EFFECTS OF PROCESSING CONDITIONS AND TESTING ATMOSPHERE ON THE ELECTRICAL PROPERTIES OF CALCIUM COPPER TITANATE CERAMICS FOR ENERGY STORAGE APPLICATIONS.

By

DISNA PRIYADARSHANI SAMARAKOON

Bachelor of Science in Materials Science and Engineering
University of Moratuwa
Moratuwa, Sri Lanka
2004

Master of Science in Mechanical Engineering
Kansas State University
Manhattan, KS
2010

Submitted to the Faculty of the
Graduate College of the
Oklahoma State University
in partial fulfillment of
the requirements for
the Degree of
DOCTOR OF PHILOSOPHY
July, 2019

EFFECTS OF PROCESSING CONDITIONS AND TESTING ATMOSPHERE ON THE ELECTRICAL PROPERTIES OF CALCIUM COPPER TITANATE CERAMICS FOR ENERGY STORAGE APPLICATIONS.

Dissertation Approved:

Dr. Raj N. Singh

Dissertation Adviser

Dr. Krishnan Ranji Vaidyanathan

Dr. Pankaj Sarin

Dr. Sandip P. Harimkar

ACKNOWLEDGEMENTS

First of all, the greatest thankfulness goes to my dissertation adviser, Dr. Raj N Singh. I am grateful to him for providing guidance, encouragement, valuable comments, and strong equipment/funding supports throughout my PhD study. Without his guidance and constant support, this work would not have been possible. Besides my advisor, sincere thanks are expressed to my dissertation committee: Dr. Ranji Vaidayanathan, Dr. Pankaj Sarin, and Dr. Sandeep Harimkar for all the constructive ideas and suggestions to address various perspectives of my research.

I extend my special appreciation to Dr. Nirmal Givindaraju for his numerous help throughout my study. I also appreciate the staff and faculty members in the Department of MSE at OSU Tulsa for their technical assistance and help. I thank Dr. Feng Lu for his continuous support whenever I needed to use the core lab facility in Helmrich Research Center (HRC) at OSU Tulsa. I would also like to thank my friends: Dr. Parvaneh Rouhani, Dr. Malay Jana, Dr. Kunal Mishra, Mr. Padmanapan Rao, Mr. Ranjan Singhal for their friendship and stimulating discussions that motivated me throughout my studies.

Last but not the least, whatever I pursue would not have been possible without my parents. I am very grateful to dedicate my doctoral dissertation to my parents. My deepest gratitude also goes to my brother and my husband for their unconditional support behind me. Most importantly, a special thank goes to my loving six-year-old son: Matheesha Manuja who brought unending inspiration to succeed my work.

Name: DISNA PRIYADARSHANI SAMARAKOON

Date of Degree: JULY, 2019

Title of Study: EFFECTS OF PROCESSING CONDITIONS AND TESTING ATMOSPHERE ON THE ELECTRICAL PROPERTIES OF CALCIUM COPPER TITANATE CERAMICS FOR ENERGY STORAGE APPLICATIONS.

Major Field: MATERIALS SCIENCE AND ENGINEERING

Abstract: Large dielectric constant (ε') in $CaCu_3Ti_4O_{12}$ (CCTO) ceramics show a potential for use in capacitive energy storage. However, large tan(δ) of CCTO is still undesirable for such applications hence finding ways to reduce the tan(δ) is very important. Dielectric properties of CCTO are very sensitive to processing conditions and are unstable at RT in air based on our new findings. The objective of the current research is to obtain a fundamental understanding of CCTO ceramics with stable large ε' and a low tan δ through processing and testing innovations.

CCTO.xAl_2O_3 (x=0,0.5,4wt.%) powders and dense ceramics were prepared by solid state reaction and sintering. High density (>90%) is achieved for sintering at 1060°C-1115°C for 5h (S1060-S1115). The temperature dependence of complex impedance (Z*) and dielectric properties of the as-prepared (pure and doped) and thinned down CCTO samples are studied in air and in dry N_2 between 23°C to 225°C. Highly irreproducible total impedance is observed in tests performed in ambient conditions at 23°C despite the sample surface conditions or doping. Stable and reproducible dielectric properties are only obtained in dry N_2 due to elimination of moisture and air. Increased space charge accumulation at GBs leading to large ε' and loss was observed in air at 23°C while stable ε' with low tan δ is measured in N_2.

The lowest tan δ of 0.010-0.013 is obtained at 23-58°C at 1.4-6 kHz for pure S1080. The resistivity of CCTO was independent of its thickness thereby confirming that the absence of surface barrier layer contribution. Total resistance of alumina-doped CCTO increased by orders of magnitude due to highly resistive $CuAl_2O_3$ at inter-grains and Al doping into intra-grains. Very low tan δ (0.021-0.020) with a large ε' (8,815-11,090) at 23°C at 500-800 Hz for 0.5wt.% alumina doping suggests the possibility of developing CCTO as capacitors. Therefore, data on as-prepared (pure and alumina doped) and thinned down CCTO measured in air and dry N_2 can be used as guidelines for developing CCTO for possible applications as capacitors.

These results indicated, for the first time, that sample processing and particularly testing atmospheres control the charge carriers, resistance, and capacitance of GBs, which in turn determine the overall magnitude and reproducibility of dielectric properties of polycrystalline CCTO ceramics.

TABLE OF CONTENTS

Chapter Page

LIST OF TABLES

Table Page

LIST OF FIGURES

Figure Page

Figure Page

Figure Page

Figure Page

CHAPTER I

INTRODUCTION

Electrical energy storage requires a large dielectric constant (ε'), better thermal stability, and a high breakdown field [1]. Maximum stored energy density of a capacitor per unit volume (U) is given by $U = \varepsilon'\varepsilon_0 E^2/2$ where, E is the applied field and ε_0 is the vacuum permittivity (8.854×10^{-12} F/m) [2]. Therefore, larger the ε', the more charge can be stored leading to miniaturization of energy storage devices. Solid $CaCu_3Ti_4O_{12}$ (CCTO) emerged as a lead-free dielectric material, which may be used in energy storage devices in the micro-electronic industries [3-5]. Cubic perovskite CCTO has a large ε' of the order of 10^5 and 10^3-10^4 in single crystals and polycrystals, respectively, at room temperature (RT) [6]. Large ε' in CCTO is stable over a wide temperature range from 100 K to 600 K [6, 7] and in a wide range of frequencies from DC up to 1 MHz [8, 9].

The value of dielectric loss (tan δ) is the most important parameter determining a dielectric material's suitability for capacitor applications. However, CCTO has a large value of tan δ (~0.1), which is still larger than the acceptable values (<0.01) [10, 11]

for capacitor applications. Value of tan δ <0.05 over a wide frequency range is still not achieved for CCTO. While the breakdown fields for CCTO ceramics is reported as small as 2 $kV \cdot cm^{-1}$ [12, 13].

Large ε' in CCTO is believed to be originated by the interfacial (or space charge) polarization due to Barrier Layer Capacitance (BLC) effect at internal boundaries [9, 14] such as grain boundaries (GBs) [8, 15, 16] and/or at domain boundaries [17] in polycrystals and twin boundaries [18] in single crystals. Surface barrier layers between sample and electrode interface are also suggested as possible sources affecting the overall dielectric properties in CCTO [19-23]. Some studies however have demonstrated that sample electrode interface is not playing a dominant role in controlling the dielectric properties in CCTO [24].

Despite the controversy on which type of internal BLC, domain or GBs play the dominant role is not clear, the GBs are reported to play a key role in controlling the dielectric properties of CCTO ceramics [25]. Although the dielectric mechanism in CCTO are not completely understood until now, intensive studies show strong evidences supporting the idea that BLC effect at GBs are the main sources of an abnormally large-ε' in polycrystalline CCTO at RT [8, 9, 25-28]. According to BLC theory, CCTO microstructure is electrically heterogeneous with semi-conductive grains surrounded by insulating GBs [6, 7, 29]. Therefore, chemical change in CCTO grains and near GBs may largely affect the dielectric behavior of CCTO.

Many strategies that are pursued so far on improving CCTO dielectric properties are therefore based on controlling the microstructure via changing the processing such as synthesis methods, sintering and/or post-annealing conditions, and doping. Most of the

research work indicated that CCTO dielectric properties can be changed by changing the grain size [26, 30, 31], non-stoichiometry [32, 33], Cu segregation [34, 37], and oxygen loss [38-40] during sintering. Doping of various cationic substitutions on either A site (Ca and Cu), or B site (Ti), and/or on both sites are also attempted by many. Some recent studies indicated the possibility of doping with Al [41, 42] or Al_2O_3 [43-45] to modify the CCTO compositions and grain size thereby enhancing the breakdown field [46-48]. Therefore, CCTO dielectric properties are sensitive to the sample processing conditions [24, 38, 49-54].

Despite the various strategies such as changes of processing and doping were carried out, preparation of either phase-pure or doped-CCTO materials with a very low tan δ while retaining its ε' above 10^4-10^5 is challenging. Even when prepared by the same method or with small changes in the processing, a wide variation of tan δ and ε' values were reported for CCTO ceramics. This indicates that this material is still not well characterized to find out the reasons for large variations in its properties. More efforts and new characterization methods are needed to fabricate CCTO materials with the optimized dielectric properties for use as capacitors in storage applications.

Reports indicate that electrical impedance of CCTO aged in air at RT can be changed by moisture, oxygen absorption, or the electrode materials being used. Humidity sensitivity of CCTO ceramics [55, 56]and thin films [57, 58]have been recognized only by limited studies by two groups. Studies on humidity sensitivity of CCTO ceramics indicate that potential barrier layer formed at the interfaces and GBs can change the low frequency dielectric properties [55, 56]. Some studies reported that impedance near RT undergo a dramatic change when the CCTO samples were aged in air due to adsorption of oxygen on the sample

surface [23]. While other studies on CCTO single and polycrystalline samples indicated a large low frequency relaxation due to surface layers, which are sensitive to air atmosphere and type of electrode material being used [19, 21].

Therefore, moisture effect from atmospheric water and air interaction should not be over-looked and could play a key role in controlling the dielectric properties of CCTO. Especially, the stability and reproducibility of dielectric properties displayed by CCTO ceramics is the most important concern, when they are used as capacitors. Despite these studies, to the best of our knowledge, no study is reported on as prepared (phase pure or doped) or thinned down CCTO (to eliminate surface layer effect) to clarify whether RT dielectric properties are still affected if measured in a moisture or oxygen free atmosphere.

In the light of these shortcomings, current research intends to address some of the above discussed issues by providing a comprehensive state-of-the-art synthesis and testing conditions for fundamental understanding of the dielectric properties of CCTO ceramics. The primary objective of this study is to investigate the effect of processing and testing atmosphere on the stability and reproducibility of the electrical properties of CCTO. To accomplish this goal, the temperature dependence of impedance spectroscopy and dielectric properties of the pure and Al_2O_3-doped CCTO samples (as-prepared) are studied in both ambient air and in dry N_2. Different sintering temperatures and Al_2O_3 doping can provide different CCTO microstructures, densities, and defects, which can respond differently to ambient conditions as well. Complex impedance of the CCTO ceramics (pure and alumina doped) prepared at various sintering temperatures are investigated in different atmospheres between 23°C and 225°C. In order to investigate effect of various testing atmospheres on the

surface or GB barrier layer effect, thickness dependent impedance measurements were also done by removing the surface layers.

Complex impedance spectroscopy and associated modeling are used to describe dielectric properties including the effect of testing conditions of CCTO ceramics. To optimize the powder processing and sample preparation conditions, pure and alumina doped CCTO calcined powders and sintered samples were further analyzed using characterization techniques such as TGA, X-ray diffraction (XRD), optical micrographs, Raman spectroscopy, Scanning Electron Microscopy (SEM), and density measurements. These results are analyzed, presented, and discussed.

The new findings from study indicated that dielectric properties of CCTO ceramics are not only sensitive to sample processing conditions but also on surrounding atmosphere. We report that sample processing and testing atmospheres may control the charge carriers at CCTO GBs. Therefore, overall dielectric properties of CCTO ceramic are affected by the resistance and capacitance of GB, which in turn can explain the important roles of surrounding atmosphere and sample preparation conditions on the stability of electrical response of polycrystalline CCTO ceramics, which have not been reported in this field of study. Comparative dielectric properties of as-prepared (pure and alumina doped) and thinned down CCTO samples measured in two different test environments (air and dry N_2) of this study can be used as a guide lines for developing CCTO for possible capacitor applications.

CHAPTER II

LITERATURE REVIEW

2.1 Theory of Dielectric Materials for Energy Storage Capacitors

Consider a parallel plate capacitor filled with vacuum under the application of direct current (DC). The capacitance (C_0) of a capacitor depends on the conductive plates of area (A) and the separation between the plates (d) as can be seen by equation 2.1.

$$C_0 = \frac{A\varepsilon_0}{d} \qquad (2.1)$$

Where, ε_0 is the vacuum permittivity. If an alternating current (ac) voltage is applied between the conducting plates of the capacitor, a charging current results (I_C), which leads the applied ac voltage by 90°. Dielectric materials can be defined as materials with high electrical resistivity that can store electrical energy in the form of electrostatic charge in the devices. When a dielectric material is placed between the conducting plates, the capacitance (C) of the capacitor is increased by a factor ε_r as given by equation 2.2, where, ε_r is the dielectric constant or the relative permittivity of the material.

Materials with a high dielectric constant have a strong ability to become polarized, which is the displacement of a charge in relation to an electric field.

$$C = \frac{A\varepsilon_0\varepsilon_r}{d} = C_0\varepsilon_r \qquad (2.2)$$

Under an external force produced by the ac electric field, atoms or molecules in the dielectric material tends to become oriented from its original equilibrium state to a new equilibrium state in a way that it opposes the external electric field. This is called charge displacement or polarization.

When an alternating current is applies (AC) as shown in Figure 2.1, the resulting current is no longer 90° and is made up of a charging current (I_C) and a loss current (I_R), respectively. Therefore, resultant current leads the applied voltage by rather 90-δ, where the value of δ is the loss angle, which indicates the phase lag between charging and loss current.

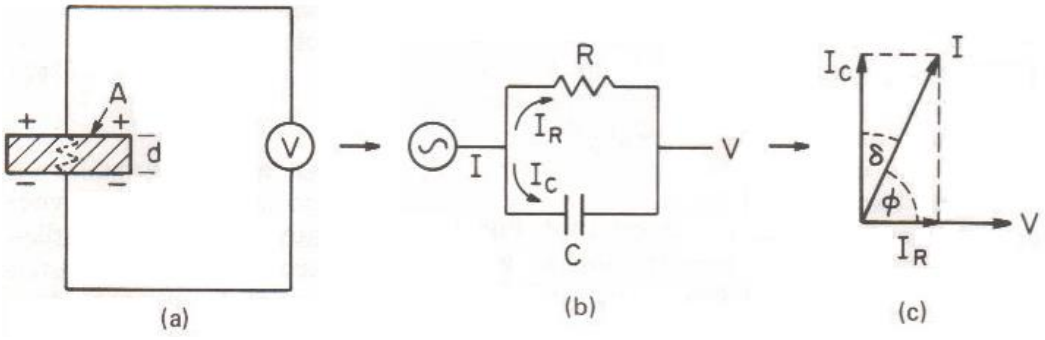

Figure 2.1. (a) A dielectric material between two parallel plates of a capacitor in an alternating electric field, (b) equivalent circuit and (c) phasor diagram for clarity. [*https://slideplayer.com/slide/3431672*].

For such a lossy (imperfect) dielectric material, the relative permittivity can be represented by a complex number (ε*) as can be seen in equation 2.3 [50, 59, 60].

$$\varepsilon_r = \varepsilon^* = \varepsilon' - j\varepsilon'' \qquad (2.3)$$

Where, the real part (ε') is the relative permittivity (or dielectric constant), which represents the energy storage capabilities while the imaginary part (ε") is the loss factor (or dissipation factor), which signifies the energy lost from the electric field and absorbed energy of the dielectric material in the form of heat.

At the microscopic level, several dielectric mechanisms can contribute to the charge displacement. They are interfacial, dipolar, ionic, and electronic polarization as shown in Figure 2.2. Electronic polarization occurs when electrons are displaced relative to the nucleus. Only the low mass bodies of the electrons can polarize at very high frequency electric fields, so they are seen in high frequencies. Ionic polarization occurs when cations and anions are displaced relative to each other while dipole orientation polarization occurs when permanent dipoles are aligned opposing to the applied ac field. Orientation of ions and permanent dipoles move slowly and can only be polarized at moderate frequencies of the applied electric fields. Space charge or interfacial polarization is the separation of charge at boundaries such as interfaces and /or grain boundaries. Space charge separation is too slow and therefore occur at very low frequencies of the applied electric field.

The time needed for a specific polarization to occur is termed as the relaxation time (τ). Therefore, orientation of dipoles of in an electric field is determined by the relaxation time, which is varied depending on the type of dielectric material and its polarizability.

Therefore, the relative permittivity of the material placed in a capacitor under an ac electric field depends strongly on the frequency of the alternating electric field. As shown in Figure 2.2, starting from low frequencies, the real part (ε') decreases in steps corresponding to a certain type of molecular movement and every time a peak in the imaginary part (ε") is encountered. This reduction of ε' is the dielectric relaxation or dispersion.

When dielectric relaxation occurs, dielectric material absorbs the energy from the applied electric field and dissipates as a heat. This can result a maximum (peaks) in the dielectric loss ε" verses frequency as can be seen in Figure 2.2. At very high frequencies, the dipole moments are not able to orient fast enough to keep in alignment with the applied field and each polarization mechanism cease to contribute resulting a reduced total ε'.

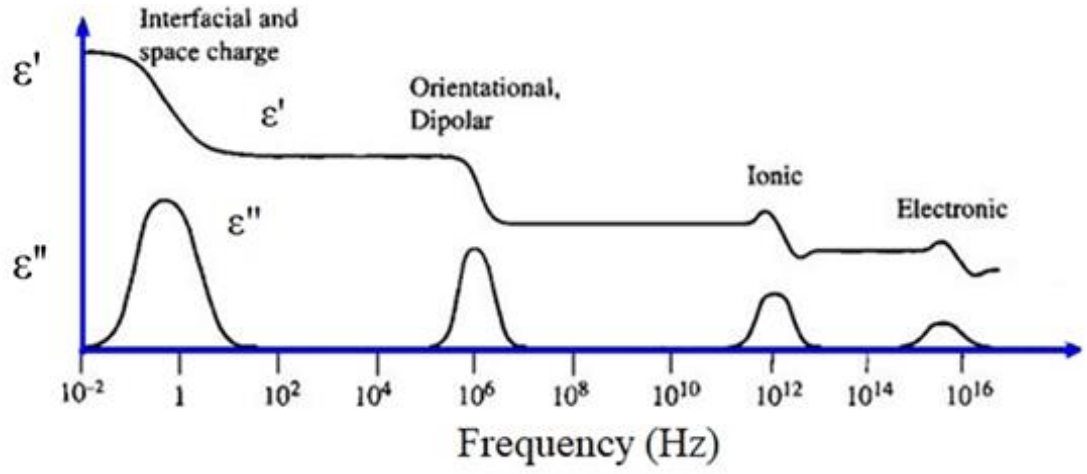

Figure 2.2. The frequency dependence of the real (ε') and (b) imaginary (ε") parts of the complex permittivity in the presence of interfacial, orientational, ionic, and electronic polarization mechanisms [61].

Relative permittivity of a materials is also dependent on the chemical structure, imperfections or defects in the material as well as other physical parameters such as temperature. Movement and rotation of molecules in a dielectric material due to the applied ac voltage on the other hand can result in a polarization and an energy loss of such materials.

Low dielectric loss is the primary factor determining the suitability of dielectric material for devise application. Term, loss tangent (tan δ) is the vector angle δ of the horizontal axis, ε' when the complex permittivity is represented in vector format [50, 59, 60] . Therefore, tan δ is the measure of the ratio of how lossy (ε") is the material to the lossless component (ε') in the application of ac electric field, which is given in equation 2.4. The value of tan δ under 0.001 (<0.1%) is considered to be quite low and 0.05 (5%) is high for practical applications [11].

$$\tan\delta = \frac{\varepsilon''}{\varepsilon'} \qquad (2.4)$$

Debye Relaxation: Dielectric relaxation of an ideal dielectric is a complex number, which is described by Debye function as given in equation 2.5 [50, 59, 60] .

$$\varepsilon^* = \varepsilon_\infty + \frac{\varepsilon_s - \varepsilon_\infty}{1+j\omega\tau} \qquad (2.5)$$

Where, τ is the relaxation time given by τ=RC and ω is the angular frequency. R and C are resistance and the capacitance of the dielectric material.

The real and imaginary parts of the equation 2.5 can be separated as follows as seen in equation 2.6 and equation 2.7.

$$\varepsilon' = \varepsilon_\infty + \frac{\varepsilon_s - \varepsilon_\infty}{1+\omega^2\tau^2} \quad (2.6)$$

$$\varepsilon'' = \varepsilon_\infty + \frac{(\varepsilon_s - \varepsilon_\infty)\omega\tau}{1+\omega^2\tau^2} \quad (2.7)$$

If real (ε') verses imaginary (ε") parts of the complex relative permittivity of Debye expression (equation 2.5) are plotted, it traces a semi-circle as shown in Figure 2.3 (a), which is the Cole-Cole diagram. Furthermore, ε' and ε" of Debye expression are also graphically represented as a function of frequency in Figure 2.3 (b).

The symbols ε_s and ε_∞, respectively in the Figure 2.3 (a) and (b) are the static (DC value or low frequency limit) and high frequency limits of real part (ε') of the complex permittivity (ε*) and τ is the relaxation time. As can be seen in the Figure 2.3, when the frequency of the applied electric field is increased, some of the polarization mechanisms will no longer be able to attain their low frequency DC values (ε_s). Therefore, ε* at intermediate frequencies can be obtained by Cole-Cole diagrams.

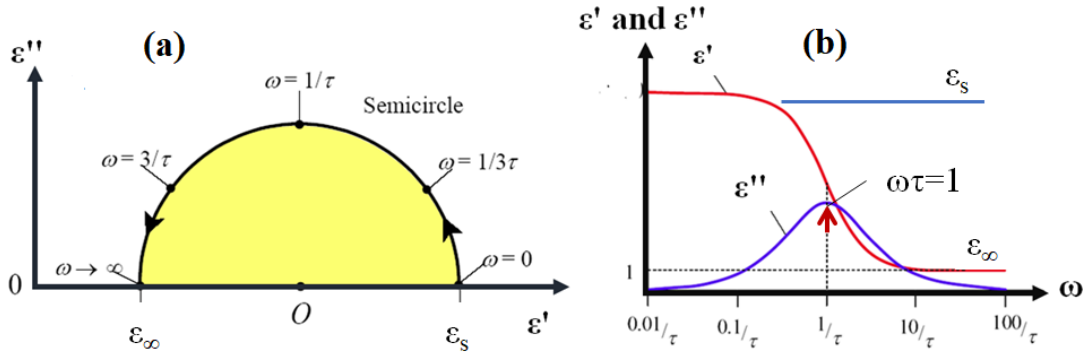

Figure 2.3. (a) Real (ε') versus imaginary (ε") parts of the complex dielectric constant as a function of angular frequency (ω), where, ω=2πf and f is the frequency [61].

Three major phenomena can be seen in Figure 2.3.

1. When the relaxation time (τ) is smaller (much faster, $\omega\tau<1$) than the frequency of the applied electric field, polarization occurs instantaneously. Therefore, for small values of $\omega\tau$, the terms $\omega^2\tau^2$ become even smaller in equation 2.6 and 2.7, resulting the real part $\varepsilon' \approx \varepsilon_s$ and small ε''. This situation can be seen in the low frequency range in Figure 2.3.
2. When τ is large, (much slower, $\omega\tau>1$) than the frequency of the applied electric field, no polarization occurs. For very large values of $\omega\tau$, $\varepsilon' \approx \varepsilon_\infty$ and ε'' is small. This situation can be seen in the high frequency range in Figure 2.3.
3. When τ and the frequency of the applied field are similar ($\omega\tau=1$) a phase lag occurs. Energy is absorbed due to phase lag resulting in a maximum dielectric loss as can be seen by a peak in ε'' at the moderate frequencies in Figure 2.3. At the maximum of ε'' value of $\omega\tau=1$.

Debye assumes that the molecules are spherical in shape and therefore the axis of rotation of the molecule in an external field has no influence in deciding the value of complex permittivity [62, 63]. However, dielectric materials deviate from ideal Debye response as the molecules in real materials may have different shapes and hence interaction between molecules can differ resulting non-ideal capacitors and resistors.

On the other hand, the relaxation times (τ=RC) of polycrystalline materials such as CCTO have more than one relaxation times (several RC components) resulting a dispersion that occurs over a wider frequency range. Therefore, a semi-circle with its center lying on the real axis (as seen Figure 2.3) cannot be seen in the Cole-Cole diagram for practical dielectric materials. Cole-Cole [63] suggested that ε' verses ε'' will still be a

semi-circle in such situations with its center displaced below the abscissa (real axis) as shown in Figure 2.4. The deviation of ideal Debye nature of the Cole-Cole diagram can then be expressed by the Cole-Cole empirical expression in equation 2.8 [62, 63].

$$\varepsilon^* = \varepsilon_\infty + \frac{\varepsilon_s - \varepsilon_\infty}{1+(j\omega\tau)^\beta} \qquad (2.8)$$

Where, $j^\beta = \cos(\beta\pi/2) + j\sin(\beta\pi/2)$. Here, β is the parameter with values between 0 and 1 related to the semicircular arc in the Figure 2.4 of which center lying between real axis of the complex plane. For an ideal Debye relaxation, β = 1. If β < 1, it implies that the relaxation has a distribution of relaxation times, leading to a broader peak shape than a Debye peak. Smaller the value of β, larger the deviation from ideal semi-circular shape.

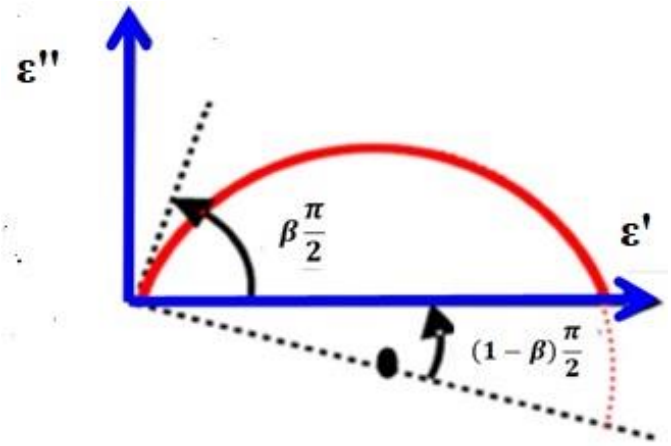

Figure 2.4. Real (ε') versus imaginary (ε'') parts of the complex dielectric constant of a depressed semi-circle where, (1-β) π/2 is the deviation angle.

The ε' and ε'' of complex permittivity in the Cole-Cole empirical expression can hence be decomposed as shown in equation 2.9 and 2.19 [60, 61].

$$\varepsilon' = \varepsilon_\infty + \frac{(\varepsilon_s - \varepsilon_\infty)\{1+(\omega\tau)^\beta \cos(\beta\pi/2)\}}{1+2(\omega\tau)^\beta \cos(\beta\pi/2)+(\omega\tau)^{2\beta}} \quad (2.9)$$

$$\varepsilon'' = \varepsilon_\infty + \frac{(\varepsilon_s - \varepsilon_\infty)(\omega\tau)^\beta \sin(\beta\pi/2)}{1+2(\omega\tau)^\beta \cos(\beta\pi/2)+(\omega\tau)^{2\beta}} \quad (2.10)$$

If dielectric materials have considerably large dc resistance (ohmic resistance) at the low frequency range, conductance losses need to be considered and added to imaginary part (ε") of the complex ε* as given in equation 2.11 [60].

$$\varepsilon^* = \varepsilon' - j\left(\varepsilon'' + \frac{\sigma_{dc}}{\varepsilon_0 \omega}\right) \quad (2.11)$$

Where, σ_{dc} is the ohmic conductivity (or dc conductivity) due to free charge carriers that can be migrated a long distance in the dielectric material. Therefore, the modified Cole–Cole expression to account for dc conduction loses is given by equation 2.12.

$$\varepsilon^* = \varepsilon_\infty + \frac{\varepsilon_s - \varepsilon_\infty}{1+(j\omega\tau)^\beta} + j\frac{\sigma_{dc}}{\varepsilon_0 \omega} \quad (2.12)$$

The imaginary part (ε") of ε* can hence be expressed by equation 2.13, which shows the losses due to dielectric relaxation (first part) and the losses due to ohmic (dc) conductivity (second part, $\sigma_{dc}/\varepsilon_0\omega$) [60].

$$\varepsilon'' = \varepsilon_\infty + \frac{(\varepsilon_s - \varepsilon_\infty)(\omega\tau)^\beta \sin(\beta\pi/2)}{1+2(\omega\tau)^\beta \cos(\beta\pi/2)+(\omega\tau)^{2\beta}} + \frac{\sigma_{dc}}{\varepsilon_0 \omega} \quad (2.13)$$

Losses due to dielectric relaxation are different from ohmic conduction losses. Both end up as heat, but conductive losses arise from free charge carriers colliding with the atoms and grain boundaries, interfaces etc., while relaxation losses are from the phase lag of the dipoles.

When dielectric materials show charge carrier induced polarization, dielectric dispersion in the frequency domain can show two or more steps due to space charge accumulation at low frequencies and dipole relaxation at high frequencies. Dielectric relaxation equation for this kind of situation can include the contribution by complex electrical conduction, which is described by equation 2.14 [50, 60].

Complex conduction (σ*) in equation 2.14 is due to two situations. One is from relaxation due to permanent dipoles (lattice response) or due to mobile charge carriers that do not involve long range mobility. Second is from conductivity caused by charge carriers involved in long range migration such as dc conduction and space charge separation [60].

$$\varepsilon^* = \varepsilon_\infty + \frac{\varepsilon_s - \varepsilon_\infty}{1+(j\omega\tau)^\beta} + \frac{\sigma^*}{\varepsilon_0 \omega^s} \qquad (2.14)$$

Here, σ* (σ*=σ_1+σ_2) is the complex conductivity, where σ_1 is the conductivity due to free charge carriers that are moving in long distance (or dc conductivity), σ_2 is the electrical conductivity due to the space charges (localized charges), and exponent s is the dimensionless parameter (0 <s< 1). For an ideal complex conductivity, s =1. If s < 1, it implies that the polarization has a distribution of the charge carrier polarization mechanism. The real (ε′) and imaginary (ε″) parts of complex dielectric function in equation 2.14 can hence be separated and are given in equation 2.15 and 2.16 [60].

$$\varepsilon' = \varepsilon_\infty + \frac{(\varepsilon_s - \varepsilon_\infty)\{1+(\omega\tau)^\beta \cos(\beta\pi/2)\}}{1+2(\omega\tau)^\beta \cos(\beta\pi/2)+(\omega\tau)^{2\beta}} + \frac{\sigma_2}{\varepsilon_0 \omega^s} \qquad (2.15)$$

$$\varepsilon'' = \varepsilon_\infty + \frac{(\varepsilon_s - \varepsilon_\infty)(\omega\tau)^\beta \sin(\beta\pi/2)}{1+2(\omega\tau)^\beta \cos(\beta\pi/2)+(\omega\tau)^{2\beta}} + \frac{\sigma_1}{\varepsilon_0 \omega^s} \qquad (2.16)$$

Above relations indicate that the conductivity may have contributions to both ε' and ε'', hence tan δ of a material is the total energy loss due to the dielectric relaxation process and dc conduction [64].

2.2 $CaCu_3Ti_4O_{12}$ (CCTO) Ceramics for Energy Storage Devices

Structure related studies identified that CCTO has an unusual perovskite structure (ABO_3 type) in which the TiO_6 octahedra are strongly tilted, giving rise to small, square planar coordinate sites for Cu and much larger space of the A-site for Ca. CCTO structure is thermally stable (remains cubic down to 35 K) with no indication of a structural phase transition, which is also an important property for it to be used in energy storage devices [7]. As depicted by Figure 2.5, Ti atoms are located at the center and O atoms are located at the corners of the octahedra, respectively.

Crystal structure of CCTO is simple cubic at RT with a lattice parameter of 7.391 Å in the space group of Im3 and Ca-O distance is reported as 2.604 Å. This Ca-O distance is much smaller than the value based on the ionic radii, which is 2.72 Å. No structural phase transition with the temperature is reported for CCTO. Single crystal CCTO are reported to be highly twinned and hence may contain nano-scale domains [7].

Since the discovery of large ε' in CCTO by Subramanian et al., the origin of its huge dielectric response has been the subject of some controversy [7] . Both intrinsic and extrinsic mechanisms are proposed to explain the unusual dielectric response observed in CCTO materials. Intrinsic origin is related to the polarization of permanent dipoles or

spontaneous polarization in the CCTO crystal lattice whereas extrinsic mechanism is related to defect induced polarization at GBs, sub-grain boundaries, domain boundaries, or sample-electrode-contact interface.

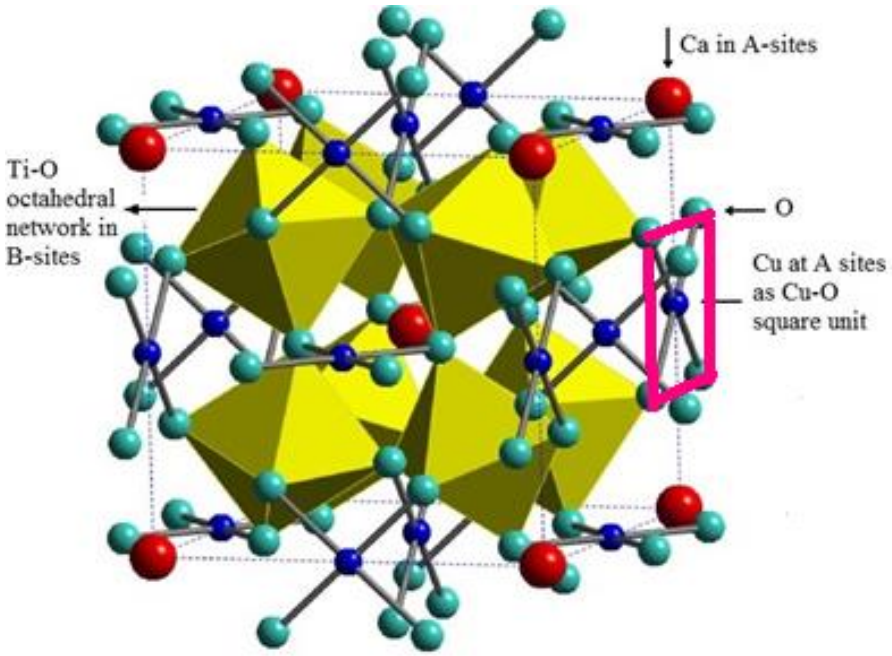

Figure 2.5. Crystal structure of CCTO: Ca (large circle) at the corner and body centered position, Cu on the face and edge centers of the unit cell (dotted lines). Octahedra are TiO_6 perovskite units. Thin and thick solid lines indicate the unit cell of typical simple perovskite ABO_3 structure and planar CuO_4 square unit, respectively [65].

The intrinsic origin of giant dielectric response in perfectly stoichiometric and defect-free crystal of CCTO as a possible mechanism had been ruled out based on the first principle calculations by authors [66]. CCTO was in their study [66] identified as a non-ferroelectric, in which dielectric response is not linked to its crystal structure and there were no direct evidences for the intrinsic lattice contribution to the ε'. The tilted nature of

TiO_6 octahedra in CCTO can frustrate the transition to a ferroelectric phase, which is the possibility of displacement of Ti^{4+} from the center of the octahedron. Later, mathematical results of the above study were further supported by the study on the structural and lattice dielectric response, which implied the extrinsic model [67].

Afterwards, there have been many other reports about the various extrinsic origins such as twin and domain boundaries in single crystals [21, 68, 69], GBs and domain boundaries in polycrystalline CCTO [17, 27, 28], and electrode interfaces in the form of interfacial contributions to the dielectric response [19, 20]. Therefore, barrier layer capacitance originated at domain and/or GBs (IBLC), surface barriers layers, and at sample electrode interface are proposed as the possible origins of large ε' in CCTO ceramics.

Single-crystal samples of CCTO are known to be highly twinned and consist of twin boundaries [70]. Therefore, the transport behavior of these domains and their boundaries in both single-crystal and ceramic samples could play a significant role in the observed dielectric response in CCTO materials. Although intrinsic origin is not possible, a large measured dielectric constant in CCTO is reported. Some studies [6, 7, 17, 71], claimed that other barrier layer mechanism(s) within CCTO grains to account for giant dielectric permittivity. Therefore, some studies claimed that there are nano-scale domains in CCTO grains can give rise to large dielectric constant in CCTO ceramics [72, 73]. While some studies reported that defects induced charge carrier transportation can form polarizable dipoles in the grains.

To obtain evidence of extrinsic effects, authors [19, 21] investigated the effects of the electrode contact on the dielectric response. Through the measurement of the frequency dependent ε′, they concluded that the high ε′ in CCTO is caused by either electrode contacts or surface oxide barrier layer effects. Furthermore, a research based on the effects of a variety of contacts and sample thickness on the dielectric response reported that there is a certain strong resistive surface oxide layer effect. This surface barrier layers are reported to have formed due to oxygen concentration gradient from CCTO inner core to the sample surface giving rise to large surface capacitance leading to large ε′ in CCTO [20].

Therefore, the origin of the huge dielectric response of CCTO has been the subject of some controversy. This is because it is not clear whether defects in the grains or GBs or surface oxide layers (surface barriers) or sample electrode interface are playing a dominant role.

However, numerous experimental investigations and intensive studies support the idea that support the idea that an external origin via Barrier Layer Capacitance effect (BLC) at GBs is the source of high-ε′ at RT [8, 9, 14, 17, 25, 29, 73] and therefore GBs are playing an important role in controlling the dielectric properties in CCTO ceramics. According to barrier layer mechanism at GBs, the structure of CCTO is proved to be electrically heterogeneous structure composed of semi-conducting grains and highly insulating GBs [9].

Figure 2.6 schematically shows the components of such a barrier layer ceramic capacitor in which electrically isolated layers are formed between inter-grain boundary and

ceramic-electrode interface in micro-scale. When an electric field is applied to such a system, migration of charge carriers occurs readily through the conducting grains, but it is hindered at the resistive boundaries leading to the formation of barriers at the GBs. Therefore, the conductivity of the entire sample is only prevented either by a failure of the conducting regions of thin insulating blocking layers at the surfaces or at internal domain or GBs.

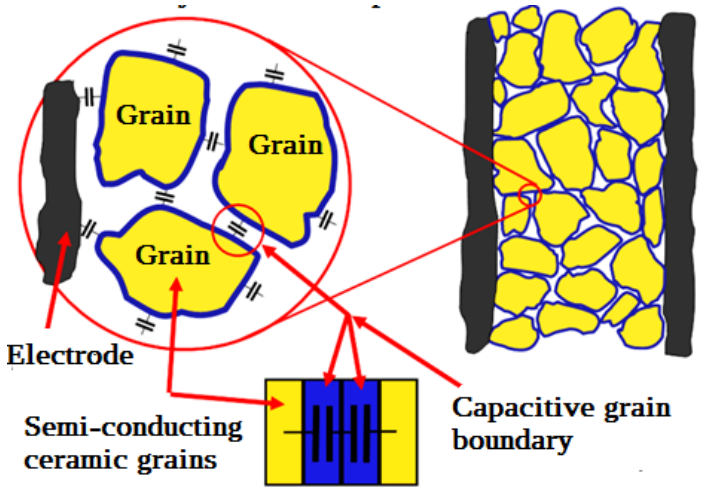

Figure 2.6. Schematic of a barrier layer ceramic capacitor

Numerous studies of CCTO ceramics showed that resistance of grain (Rg) and GBs (Rgb) are such that $R_g <<< R_{gb}$ and $C_g <<< C_{gb}$ at relatively low frequencies (10-10^5 Hz). In most reports for CCTO are sintered at 1000-1100°C for 2-10 h, and the grain resistivity measured at RT show approximately 10-100 Ωcm while GB resistivity exceeds 1 MΩcm. Much larger reported Rgb than grain or electrode implies that barrier layers capacitor in CCTO are dominated by the capacitance and resistance of GBs. Therefore, compositional and microstructural changes in GB regions are important to understanding and optimization of dielectric mechanisms of CCTO ceramics.

2.3 Mechanism of CCTO Barrier Layer Capacitance (BLC) Effect

Internal barrier layers in CCTO ceramics are formed spontaneously as a result of a single-step sintering in air, which is quite the opposite of the processing of conventional $BaTiO_3$ and $SrTiO_3$ based dielectrics requiring a multi-stage sintering at oxidizing and reducing environments [9].

Formation of semi-conducting grains and insulating barrier layers is suggested to be based on the small loss of oxygen and cation reduction (Cu-loss) during sintering at high temperatures. The driving force for reduction of oxygen in air is reported for titanite based ceramics seem to be due to partial O_2 pressure in air is lower than the equilibrium partial O_2 pressure at high temperatures [38, 40, 74, 75]. A small loss of oxygen from the lattice at high temperatures can form oxygen vacancies and free electrons in these oxide CCTO. As given in the equation 2.17, charge compensation occurs via reduction of Ti^{4+} to Ti^{3+} giving rise to the non-stochiometric formula $Ca(Cu_3)Ti_{4-x}^{4+}Ti_x^{3+}O_{12-x/2}$ [76].

$$O_O^{2-} + 2Ti^{4+} \rightarrow V_O^{\cdot\cdot} + 2Ti^{3+} + 1/2\, O_2 + 2e \uparrow \qquad (2.17)$$

On the other hand, Cu-loss within individual grains and segregation of liquid CuO and/or Cu_2O at the high sintering temperatures due to oxygen concentration gradient between sample surface and inner core can also lead to the cation reduction in CCTO [8]. Probable explanation for CuO volatility during sintering was reported in early studies by authors [18] based on the fact that Cu^{2+} becomes unstable on heating at high temperatures and reduces to Cu^{1+}. Authors [18] suggests that upon slight reduction of Cu^{2+} to Cu^{1+} at high temperatures (1000-1120°C) in air atmosphere, substitution of Ti on Cu sites occurs

giving rise to non-stoichiometric formula $Ca(Cu_{3-3x}^{2+}Cu_{2x}^{+1}Ti_x^{4+})Ti_4O_{12}$ as given in the equation 2.18 to maintain the charge neutrality .

$$3Cu^{2+} \rightarrow 2Cu^{1+} + Ti_{Cu}^{4+} + Cu \uparrow \qquad (2.18)$$

Also due to Cu volatility or Cu segregation, the loss of Cu can give rise to the formation of Cu vacancies in CCTO lattice. Charge compensation on such situations is suggested to occur via the partial oxidation of Cu^{2+} to Cu^{3+} giving rise to non-stoichiometric formula $Ca(Cu_{3-3x}^{2+}Cu_{2x}^{3+}V_x'')Ti_4O_{12}$ as given in the equation 2.19.

$$3Cu^{2+} \rightarrow 2Cu^{3+} + V_{Cu}'' + Cu \uparrow \qquad (2.19)$$

Upon cooling, re-oxidation of some of the Cu_2O back to CuO was proposed to occur while Ti^{4+} reduces to Ti^{3+}. According to this proposed model, the charge compensation occurs by partial occupation of excessive Ti^{4+} on the Cu-site as given in equation 2.20, leading to formula $Ca(Cu_{3-x}^{2+}Ti_x^{4+})Ti_{4-2x}^{4+}Ti_{2x}^{3+}O_{12}$.

$$Cu^{1+} + Ti^{4+} \rightarrow Cu^{2+} + Ti^{3+} \qquad (2.20)$$

As noted by authors [18], the required defect level to induce the anion or cation defects is very small ($x<0.0001$) to produce grain semi-conductivity of ~0.01 S/m at 300 K. However, the detection of such a small change is challenging using most of the chemical analysis techniques.

If the cooling rate is rapid, inadequate re-oxidation of Cu_2O to CuO can lead to inconsistent microstructures, non-stoichiometry, and porosity in the surface and interior

of the CCTO ceramics. Limited re-oxidation of grains and oxidized GBs/surfaces are the reasons for resistive barrier layers in CCTO. Therefore, semi-conductivity of grains and insulating GBs rely on conduction of mixed valence Ti^{3+}/Ti^{4+} and Cu^{1+}/Cu^{2+} or Cu^{3+}/Cu^{2+}.

Eventually, both Cu-loss and oxygen loss mechanisms can lead to non-stoichiometry, oxidized GBs/surfaces, limited re-oxidation of grains, and point defects in the CCTO microstructure. Possible charge carriers in CCTO ceramics are reported as oxygen vacancies (V_o and Vo"), partial charges of Ti^{3+}/Ti^{4+} and Cu^{1+}/Cu^{2+}, and H^+/OH^- (due to humidity) in which cations are reported to be more mobile than the anions [73].

Following the model suggested by authors [18], correlation of Cu-stoichiometry with many parameters such as microstructures, processing conditions, and the resulting dielectric response of CCTO have been the subject for many reports. The trend is toward accepting the Cu and Ti reduction and the formation of oxygen vacancies within individual grains leading to the chemical inhomogeneity of the CCTO lattice and non-stoichiometry of the CCTO phase [77-79].

It was known that CCTO ceramic sintered at elevated temperatures is likely to have Ti^{4+} and Ti^{3+} ions and the possibility of local electrical polarization as their centers do not coincide in the unit cell [80]. This indicates the possibility of polarization originating (without a permanent dipole) at a cation and anion pair. It is also reported that there could be an exchange of electrons between Ti^{3+} and Ti^{4+} under the applied electric field. Mixed valence cations Ti^{3+} and Ti^{4+} together with oxygen are reported to form Ti^{3+}–O–Ti^{4+} bonds and under electric field while 3d electrons in Ti^{3+} ions can hop to Ti^{4+}. Further, the

formation of Ti^{3+} is likely to distort the lattice because of its larger ionic radius (0.67 Å) than that of Ti^{4+} (0.605 Å).

Positively charged defects sites are reported as acceptor centers and can introduce p-type charge carriers [51, 81]. Therefore, local fluctuation of these p-type carriers and electrons (n-type carriers) in CCTO would increase the defect induced dipolar effect and contribute to the dielectric polarization [81, 82]. In the application of ac electric filed, a positive space charge and a negative space charge layers can also induce the charge accumulation at insulating GBs while contributing to defects induced polarization in the grains.

Therefore, CCTO dielectric properties are directly related to resulting microstructure and defects. Many studies have therefore attempted to minimize the dielectric loss as well as conductivity in CCTO by altering the chemistry and structure of the insulating barrier layers via changing the processing conditions and/or doping.

2.4. Factors Affecting the Dielectric Properties of CCTO

2.4.1 Synthesis Methods

CCTO is mostly synthesized by solid-state reaction. Many wet-chemical routes such as sol–gel, co-precipitation, sol-gel combustion, and chemical pyrolysis have been successfully put into practice for synthesis of CCTO. Solid-state route involved mixing of oxides of various cations and ground to fine powder using a ball or attritor milling. In wet-methods, individual components of the intial raw materials are mixed at atomic level and hence are proved to be advantageous over conventional solid-state method in terms

of homogeneous mixing, shorter reaction times at low temperatures [83]. In addition, these solution-derived powders have fine particles as compared to the solid-state method.

However, secondary phases commonly occur in sol-gel prepared CCTO due to the solubility limits of three different precursor solutions. Authors [83] showed that presence of CuO and TiO_2 as impurity phases in CCTO ceramics can lead to poor densification due to the calcination of sol-gel prepared precursors at relatively low temperatures (850°C for 2 h).

Authors [84] reported that secondary phases, which were observed after calcination of dried-gel at 900°C, were diminished upon sintering at 1040°C for 3 h and then 30 h making a single-phased CCTO. Further, they [84] investigated the effect of synthesis route in terms of variation of ε′ of CCTO pellets prepared by chemical pyrolysis and sol-gel combustion methods. Ceramics prepared by the combustion method showed a bimodal microstructure with a narrow distribution of grains in the range of 0.4–1.0 μm and with some grains as large as 20 μm. For the pyrolysis method grain size was 3 μm at 1040°C, which is a little larger than those made by the combustion method in this study. However, strong microstructure dependent dielectric constant rather than synthesis route was observed by this work [84]. Dielectric constant measured at -150°C and 113.38 Hz were 159,330 and 39,008 for sol-gel combustion and pyrolysis method, respectively.

Authors [10] reported the sol-gel prepared CCTO (calcined at 700°C) precursors at various pH values over a range from 1.06 to 1.77 of the solutions. For all the samples, secondary phases like $CaTiO_3$, CuO and TiO_2 were detected. However, those secondary phases were minimized when the pH was 1.6. This can be attributed to inconsistency of

mixing of precursor solutions due to the formation of minor phases before they go into the solution.

In recent years, development of sol-gel techniques involved using expensive alkoxide, titanium nitrate or chloride, titanium alkoxide $Ti(OR)_4$ as the titanium source [85]. Compared to solid-state route, costly precursors involved in wet-methods lead to a challenge in large scale production of CCTO using wet-methods [85]. The lowest dielectric loss values and respective dielectric constants reported in the recent past for preparing pure CCTO by both dry and wet methods are listed in Table 2.1.

As depicted by Table 2.1, ε' as high as 10^4 at 1 kHz and tan δ as low as 0.014-0.20 at 1 kHz at RT for pure CCTO were achieved by sol-gel method. Whereas CCTO ceramics sintered at 1100°C for 24 h attained a ε' of 250,000 and a tan δ of 0.1 at 1 kHz by the solid-state method. Table 2.1 also inferred that up to now, the greatest challenge for CCTO ceramics synthesis is to lower the tan δ while keeping the large ε'.

Although sol-gel prepared CCTO showed a relatively smaller tan δ than that of solid-state method at 1 kHz, a very large tan δ value (>0.01) is still unsuitable for its practical applications.

Table 2.1 clearly demonstrated that to date, experimental results from these studies were promising for high relative permittivity. These studies however, either rarely highlight the suitability of CCTO for capacitor applications or provide clear clues for observed large tan δ values.

Table 2.1. Dielectric properties reported for pure CCTO prepared by different methods at room temperature in recent past.

ε′ (at 1 kHz)	tan δ (at 1 kHz)	Sintering	Synthesis	Year
250,000	0.1	1100°C/24h	Solid-state	2002 [8]
~9,516	~0.020	1100°C/16h	Sol–gel	2012 [83]
59,000	0.06	1125°/4h	Sol–gel	2012 [86]
35,000	~0.014	1100°C/15h	Sol–gel	2013 [10]
61,000	0.05	1050°C /24h	Sol–gel	2014 [87]
18,225	0.028	1100°C/16h	Sol–gel	2015 [88]
48,600	0.15	1050°C/30h	Sol-gel	2015 [85]
123,000	~0.25	1125°/4h	Sol–gel	2015 [89]
60,000	0.2	1050°C/4h	Solid-state	2015 [90]
>10,000	>1	1100°C/10h	Solid-state	2016 [91]
>40,000	0.1	1200°C/12h	Solid-state	2018 [92]

In general, analyzing the dielectric properties reported by various synthesis techniques implies that variation of the dielectric constants does not necessarily mean that one synthesis technique is superior to the other. This is because the ε′ of CCTO strongly depends on the microstructures and grain size of the samples.

2.4.2 Sintering Conditions

Numerous studies showed that there is a strong correlation between CCTO dielectric properties and sintering conditions such as temperature, dwell time, and sintering atmosphere. Effect of sintering temperature on the electrical properties of pure CCTO in the range 1000-1140°C was investigated by many groups. Fang et al. [78,93] observed an

increased resistivity of GBs due to the existence of Cu-rich boundaries. Segregation of Cu during sintering [38] and oxidation near the sample surface [94] can also change the concentration of defects near the surface, GBs, and grain interior, which are contributing for the polarization and conductivity of CCTO [50].

Authors [30] reported that slower heating rates would allow sufficient time to create a higher concentration of Cu^{1+} during sintering at 1100°C for 2 h. Hence, if the cooling rate is rapid, CCTO re-oxidation occurs only by changing some amount of Cu_2O to CuO leading to inadequate time for re-oxidation of Cu_2O to CuO. Therefore, surfaces of CCTO samples and the outside of each grain can be well oxidized, while the interior of the grains remains oxygen deficient. Authors [30] observed a Cu_2O phase in pure CCTO ceramics sintered in air at 1115°C followed by air quenching. They demonstrated the segregation of a Cu-rich phase on the unpolished CCTO surface might have been due to high mobility of CuO to diffuse to the sample surface via GBs.

All in all, sintering in air at high temperatures and subsequent cooling can result in different oxidation states in CCTO materials. Many reports on sintering studies of CCTO ceramics suggested liquid CuO can act as a sintering aid, which can lead to grain growth during sintering, which can eventually affect electrical properties of CCTO ceramics. As reported by [95, 96], increasing temperature can cause an increase in liquid phase of CuO leading to increased grain size as well as porosity due to its high volatility of CuO at high sintering temperatures above 1000°C. Some studies [10] confirmed the presence of porosity reduce due to rapid migration of CuO/Cu_2O phase with increasing sintering temperature.

Authors [96] reported an enhanced ε′ of CCTO ceramics sintered at higher temperatures (1025-1125°C) with increased dwell times. They [96] observed a bimodal microstructure when the holding time and the temperature are increased above 1075°C. The intergranular phase was observed to be more Cu-rich at 1100°C as compared to sintering at 1050°C for the duration of 4 h. When sintering temperature was increased beyond 1075°C, ε′ was very high and became frequency dependent [96]. Ceramics sintered at 1125°C showed a significantly higher ε′. Similar investigation by authors [95] highlighted that ε′ is simply increased with the sintering temperatures.

An excessive dwell time can also be disadvantageous because it creates some pores inside the sample, which can decrease the ε′ due to increased evaporation of CuO [95]. Some extent of CuO segregation is important in the formation of the insulating GBs and has a significant influence on ε′. A longer sintering time can increase stoichiometric composition of grains by limiting the further migration of Cu^{1+}/Cu^{2+} ion out of the grains. If the time given for the formation of stoichiometric grains is low, Cu-deficiencies are expected in the grains. Adams group [97, 98] prepared single phase CCTO at 1100 °C for 3 and 24 h, respectively in air. On prolonged sintering grain growth occurs from ~3-5 μm (fine-grained) after 3 h to about 100-300 μm (coarse-grained) after 24 h [44]. The impedance associated with such a microstructure were such that Rg (grain resistance) was 70 Ω and 30 Ω, whereas Rgb (GB resistance) of 0.18 MΩ and 4.2 MΩ for the 3 and 24 h samples, respectively. Due to the change in microstructure and grain size, ε′ observed at RT were 10,000 and 300,000 at 1 kHz for samples sintered at 1100 C for 3 h and 24 h, respectively. Obviously, increasing dwell time is expected to increase the grain size,

which is linearly proportional to the ε′ provided that good ceramic densification is achieved.

Large ε′ at extended sintering times is attributed to thin down of the GBs too [99]. This is due to incorporating the secondary phase back into the CCTO crystals at long sintering times [99]. Authors [96] has investigated that evolution of CCTO microstructure by thinning down the GBs by increasing the consumption of small Cu-rich grains, which resulted in a stoichiometric grain interior. Authors [10] observed that increasing the holding times (up to 15 h), the Rgb reaches the highest value (0.87 MΩ), which leads to the highest ε′. Further increasing the holding time beyond 15 h, Rgb was decreased, which indicates that a certain amount of CuO was beneficial in CCTO dielectrics and evaporation of CuO at longer dwell time is not desirable. Here, the highest density sample showed excellent dielectric properties. Furthermore, they [10] found that grain surface of the CCTO ceramics sintered at 1100°C for 15 h showed a nearly stoichiometric element ratio while that for the GB showed a Cu-rich phase.

2.4.3 Dimensional Effect

Adams group [97, 98] observed that dielectric properties of coarse-grained sample is sensitive to electrode material and sample thickness only at low frequencies. When the coarse-grained ceramic of initial pellet thickness of 1.9 mm was reduced to 0.34 mm by layer by layer polishing, they observed Rgb was reduced from ~4 MΩ to as low as 25 kΩ, while Rg was slightly increased. In contrast, a fine-grained sample did not show any significant change due to electrode or sample thickness effect.

Adams group [97, 98] showed that thickness variations related electrical properties of as-sintered and coarse-grained ceramics can be attributed to inhomogeneous microstructure, which contains regions of fine-grains and regions of extremely large grains, where Rgb>>>Rg. Applied electric field through such an electrical microstructure can be restricted across the islands of small grains due to large number of resistive GBs.

In such a case, Rgb can be dependent not only on its thickness but also on the distribution of large and fine-grained regions and the conductivity of grains. Therefore, thickness dependent dielectric response is observed at low frequencies. These observations suggest that in case of CCTO coarse grains, the electrode effect and thickness variations have a certain contribution to the overall high-ε′.

On the contrary, authors [19] performed dielectric measurements as a function of electrode effect (using brass, Ag and Au electrodes) and thickness effect (0.69 and 0.24 mm). They claimed that change in the permittivity below 1 MHz for both the electrode-type and pellet-thickness experiments were attributed to an electrode effect and is not due to a grain boundary effect. Unfortunately, results by this report did not provide any details on the microstructure of the ceramics. Therefore, we can assume that these assumptions of electrode effect may not be valid when relating to the effect of the thickness.

Dielectric spectroscopic studies [19, 21, 69] on both single and polycrystalline CCTO samples indicated that a large low frequency relaxation due to surface and/or GB are sensitive to the electrode material being used [19, 21, 69] and sample preparing conditions such as post-annealing atmospheres and temperatures as reported by many

[20, 38, 50]. The low frequency behavior can be attributed to changes in two types of surface layers; the GBs and sample electrode contact, respectively.

Depending on the synthesis conditions, limited re-oxidation of grain interior and oxidized GBs or surfaces are possible in CCTO [9]. A study by authors [38] showed that a large low frequency relaxation at low frequency is attributed to surface layers, which were originated due to segregation Cu-rich phase during sintering. They observed the disappearance of large ε′, upon thinning down of the outer surface layers of the pellet samples, which were found to be Cu-rich. However, it is not clear whether they have conducted the experiment in a controlled atmosphere while measuring dielectric properties of the polished sample or as-prepared samples. Authors [36] showed the presence of small additional arc related to surface layer effect in the as-prepared sample. Their experiments showed that after subsequent polishing the samples, the impedance arc related to the surface layers were disappeared. They ascribed the changes due to the segregation of highly oxidized Cu-rich phases on the surface.

Another reported work by them [38] claimed that due to the inhomogeneous distribution of oxygen on the surface and the interior can lead to preferential segregation of oxidized Cu-rich phase (more resistive) on the as-sintered surface. Segregation of oxidized Cu-rich phase near the surface can change the surface resistivity while enhancing the ε′.

Therefore, upon layer by layer thinning down the top and the bottom surfaces of the as-sintered sample can reveal less oxidized Cu-rich surface layers (less resistive) leading to low ε′ and low surface resistance. However, it is not clear whether they conduct the experiments in the controlled atmosphere.

2.4.4 Doping

Doping has been used to enhance the dielectric properties in CCTO by various cationic substitutions on either A site (Ca and Cu), or B site (Ti), and/or on both sites in CCTO. Researchers have indicated that defects in CCTO can be changed via doping schemes. The excessive charge carriers from the replaced element in the A-site or B-site ($Ti^{4+)}$ of CCTO perovskite is accommodated by the creation of vacancies, which can change conductivity of grains and GBs in CCTO [11].

Study on different cation doped CCTO can therefore provide new insights into the role played by CCTO grains and GBs depending on the site/s where the dopants are occupied. Cation vacancies tend to be separated by oxygen ions so that there is a considerable energy barrier to be overcome before the ion and its vacancy can be interchanged. Donor–cation vacancy combinations are reported to have a stable orientation so that their initial random state is unaffected by applied fields.

Whereas acceptor–oxygen vacancy combinations are likely to be less stable and thermally activated and hence reorientation may take place in the presence of local or applied electric fields. Therefore, type of dopant (donor and acceptor) has a strong effect on dielectric properties of CCTO.

Table 2.2 shows the ε' and tan δ values reported in some of the doped CCTO with various cations and in some CCTO related composites. Doping of CCTO has been carried out on partial substitutions of Ca ions of CCTO such as substitution by La and Sr and Cu ions by Zn^{+2} and Mg^{+2} as can be seen in Table 2.2. Much work has been carried out on partial

substitutions of Ti sites by cations such as Cr [100], Fe [101], Mn [102] , V [103], Hf [104], and Ga [105].

Some examples of the reported acceptor dopant elements are Mn^{3+}, Co^{2+}, Co^{3+}, Fe^{2+}, Fe^{3+}, Ni^{2+} and Zn^{2+}. Acceptor ions such as Mn^{3+} on Ti^{4+} sites give rise to oxygen vacancies but without the liberation of electrons [11]. The oxygen ions however form a continuous lattice structure and the oxygen vacancies have oxygen ion neighbors, which they can easily exchange with electrons and increase conductivity. Therefore, oxygen vacancies and space charges (electrons) can result in higher conductivity.

Donor dopant is defined as dopant elements with a higher ionic charge than ions they replace, causing cation vacancies [11]. Elements with an ionic charge of La^{3+}, Bi^{3+} and Nd^{3+}, are usually used as A-site donors for perovskite structures, and elements with ionic charges Nb^{5+}, Ta^{5+}, Sb^{5+} or W^{6+}, can be used as B-site donors.

Despite the reported work related to implementing doping strategies, studies reported so far however hardly highlight suitability of CCTO for capacitor applications. Very recently, a group demonstrated that the formation of spinel-$CuAl_2O_4$ phase in the intergranular regions can increase the breakdown field and GB resistance of CCTO ceramics while inhibiting the grain growth [46-48]. This suggests that Al-doped CCTO ceramic materials have a high potential for use for capacitator applications.

As can be seen in the Table 2.2, Mg^{2+} and La^{2+} in Cu and Ca sites, respectively has lowered the tan δ. However, the overall ε' has decreased. Al-doped samples show relatively enhanced ε' and tan δ values.

Furthermore, it is also difficult to make a good comparison of Al content in each of their systems due to the variations in the preparation methods. A comparative study on the effects of GB has not been studied for Al-doped CCTO ceramics subjected to various sample preparation conditions.

Table 2.2. Dielectric properties reported for doped-CCTO at room temperature.

Element	Method	Sintering	ε′ (1 kHz)	tan δ
In Ti^{4+} Site				
Cr^{4+} (x=0.01)	Solid-State	1100°C/2h	19,004	0.049 [106]
Nb^{5+} (x=0.01)	Solid-State	1100°C/2h	6,200	0.263 [106]
Zr^{2+} (x=0.01)	Solid-State	1100°C/2h	5,430	0.019 [106]
Zr^{2+} (x=0.1)	Sol-gel	1000°C/10min	12,00	0.120 [107]
Ga^{3+} (x=0.01)	Solid-State	1050°C/5h	31,330	0.044 [105]
Sc^{3+} (x=0.04)	Solid-State	1090°C/6h	57,150	0.303 [108]
Al^{3+}	Solid-State	1040°C/4h	30,226	0.100 [109]
Al^{3+} (x=0.06)	Solid-State	1100°C/12h	41,000 (10 kHz)	0.034 [41]
Al^{3+} (x=1.5%wt.)	Solid-State	1050°C/5h	81,000	0.080 [110]
Al^{3+} (x=0.3)	coprecipitation	1080°C/20h	12,710	0.070 [111]
In Cu^{2+} Site				
Zn^{2+} (x=0.05)	Sol-gel	950°C/12h	5,971	0.18 [112]
Mg^{2+} (x=0.1)	Sol-gel	1080°C /8 h.	2,520	0.017 [113]
Mg^{2+}(x=0.3)	Solid-State	1100°C/12h	17,300	0.052 [113]
Ni^{3+} (x=0.31)	Solid-State	1060°C/6h	51,600	0.034 [114]
In Ca^{2+} Site				
Sm^{3+} (x=0.05)	Solid-State	1090°C/6h	10,863	0.043 [115]
Sr^{3+} (x=0.)	Sol-gel	1070°C/9h	14,369	0.023 [116]
La^{3+} (x=0.2)	Sol-gel	1070°C/9h	2704	0.012 [116]
Y^{3+}	Solid-State	1100°C/12h	9,832	0.014 [117]
Tb^{3+}	Sol-gel	1070°C/4h	2,090	0.051 [118]
CCTO Composites				
CCTO/CuO	Solid-State	1000°C/10h	16,875	0.074 [35]
CCTO/$CaTiO_3$	Sol-gel	1020°C/24h	~6,513	0.015 [119]
CCTO/$CaTiO_3$	Solid-State	1100°C/3h	23,600 (10kHz)	0.406 [120]
CCTO(0.5)HfO_2	Solid-State	1000°C/10h	4,298 (100 kHz)	0.064 [121]
CCTO(0.1)ZrO_2	Solid-State	1100°C/1h	5,030	0.016 [122]

2.4.5 Humidity and Air Interaction with CCTO

The behavior of CCTO exposed to reducing atmosphere and oxidizing atmosphere is reported in earlier studies. The reported behavior indicates that when the CCTO thick films exposed to reducing atmosphere (such as N_2) at RT, oxygen vacancies can be generated [123]. These oxygen vacancies may act as mobile space charges and can decrease of the surface resistivity [124]. Conversely, in the oxygen rich atmosphere, oxygen vacancies in the CCTO are filled and decrease the mobile space charges leading to an increased surface resistivity. Reports also indicated that if the resistivity of the ceramic is as high as $1.2x10^8$ Ωcm, mobile space charges are absent on the surface at RT [124].

Despite the differences in the material, humidity interaction with oxide ceramics surface is explained through three mechanisms. They are; the chemical adsorption, physical adsorption of water molecules on the surface, and capillary condensation in the open pores of the microstructure as can be seen in Figure 2.7.

Hydroxyl species (OH) can be formed by the reaction of a water molecule with an adsorbed O^{-2} ion. These chemisorbed two OH can evolve to water vapor at 300-500°C [125-127]. Succeeding layers are physically adsorbed on the chemisorbed layer as shown in Figure 2.7. The first physiosorbed layer is stable and removable at 100-160°C. Second physically adsorbed layer is relatively mobile and removable at 80-100°C.

However, complete removal of physically absorbed moisture was achieved by heating the sample inside the tube furnace at the ambient temperature of ~400°C [126]. Mechanism

of humidity interaction with metal oxides depends mainly on the bulk properties such as microstructure, pore size and volume, grain size, and defects. Various surface reactive sites such as porosity, point defects, large surface areas, and vacancies enhance moisture adsorption on the oxide ceramics [125, 128, 129].

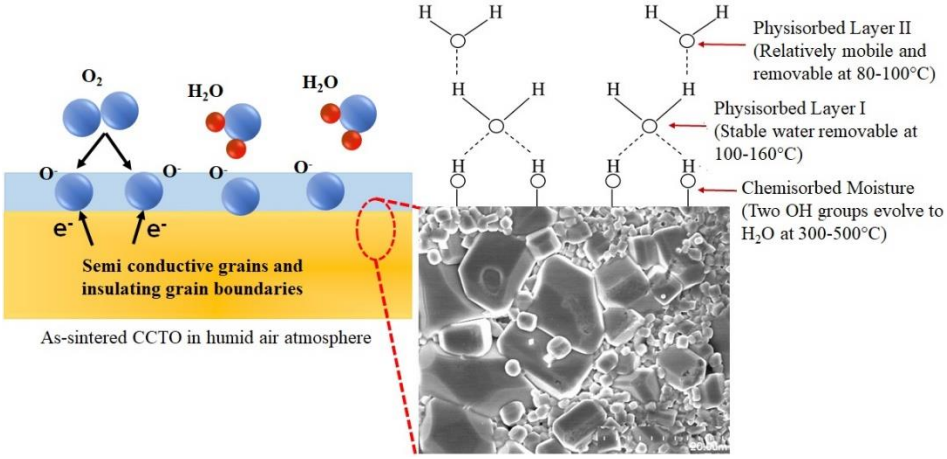

Figure 2.7. Schematic of moisture absorption on CCTO ceramics surface

Due to the presence of humidity in the air, conduction mechanism of oxide ceramic sensors can be either ionic or electronic [125, 130]. In ionic-type humidity sensors, the conduction mechanism is mainly due to the displacement of protons between the physically adsorbed water molecules. Impedance of the material decreases with increase of humidity due to the ionic type physisorption and capillary condensation of water molecules on the surface of the material. At higher humidity, water molecules are adsorbed only through one hydrogen bond and the proton-transfer process dominates and capillary condensation takes place in the pores. Hence, the water molecules can move freely and the impedance value decreases.

In contrast, at lower humidity, water molecules are attached on the surface of ceramic through two hydrogen bonds. As a result, the water molecules are not able to move freely and thus, the impedance value increases. In the electronic type sensor, water molecules are chemosorbed by donating electrons on to the surface and a thin layer of hydroxyl groups (OH^-) are formed on the surface. Depending on whether the material is an n or p-type semiconductor, electronic conductivity of the material increases or decreases.

Although moisture effect was not identified, some research work indicated a dramatic change of impedance measured near RT when CCTOs were aged in air [23]. Work by authors [23] indicated that complex impedance measured in CCTO ceramics at RT were changed after aging the samples in air. They [23] suggested this instability to high sensitivity of the sample-electrode interface to oxygen adsorption. They [23] argued that grains and GBs will not be sensitive to atmosphere when kept in air at RT. They showed that only the impedance related to sample/Au-electrode-contact was sensitive to the surrounding atmosphere. They observed a gradual increase of electrode contact resistance from the initial value of 7.7 kΩcm to 23 kΩcm and then to 75 kΩcm, respectively after aging the samples in air for 4 h and then for 18 days at RT while no change was observed for bulk. After annealing in air at 300°C, a large reduction in electrode resistance and capacitance were reported with no changes to GB or grain resistances [23].

Authors also [23] claimed that the electrode contact impedance can be sensitive to sample/electrode treatments and surrounding atmosphere if the Rgb of CCTO samples are considerably low. However, they did not show the range of GB resistances measured at various atmospheres other than air to find its sensitivity to the testing atmosphere.

They also suggested that adsorption of oxygen at the sample electrode interface might play a role to alter the dominant electrode effect.

In polycrystalline CCTO ceramics, formation of oxygen vacancies during sintering at high temperatures in air or sintering in reducing environment is reported [18-20]. When oxide ceramics are exposed to air, atmospheric oxygen can be chemisorbed on to the surface by capturing free electrons from the conduction band thereby decrease the electron concentration. In absence of oxygen ion vacancies, improved wetting properties of ZnO surface due to adsorption and desorption of water is reported [129].

It is also reported for other oxide ceramics that water competes with oxygen for the surface vacancies. The adsorption of water molecules on the surface of CCTO can also decrease the surface area that is responsible for the oxygen chemisorption and sensitivity. The effects of water vapor have been discussed in terms of the displacement of chemisorbed oxygen by H_2O and OH^- formation on SnO_2 [126, 127]. Desorption of the adsorbed OH in the surface can produce water and oxygen [127]. Adsorbed oxygen is an oxygen molecule trapped in or on a surface oxygen vacancy. Water competes with oxygen for the surface vacancies. In the presence of surface rich in oxygen vacancies can therefore increase the moisture absorption.

If the ceramics surface or GBs are rich in oxygen vacancies during processing, then it might increase the moisture absorption by CCTO. This is because an OH group can occupy a vacant oxygen ion sites at the surfaces and interfaces without distorting the lattice as reported for the other oxide ceramics [126, 127].

2.5 Summary

Dielectric properties of CCTO are strongly dependent on processing conditions, microstructure, sintering conditions, heat treatments, and doping. Even when prepared by the same method, there is a wide range of effective permittivity values indicating that some other conditions other than just the synthesis technique alone are playing a role in controlling dielectric properties of CCTO. CCTO dielectric properties are highly sensitive to changes in the microstructure and electrical properties have been based on the extrinsic mechanisms as suggested by barrier layer capacitance effects at GBs. Although the mechanism responsible for these exceptional properties in CCTO ceramics are still not fully understood, any changes to electrical properties of grain and/or GBs will affect the overall dielectric behavior of CCTO. On the other hand, it is very important to eliminate or decrease the dependence of the dielectric properties of CCTO on ambient conditions such as humidity and air on measured dielectric properties for use as capacitors in energy storage applications. Key questions to address regarding electrical properties of CCTO are how microstructure is changed to form highly resistive insulating layers and how large-ε' and tan δ are obtained from such a microstructure.

CHAPTER III

RESEARCH OBJECTIVES AND APPROACH

Although CCTO has a large dielectric constant (ε'), high dielectric loss hinders its practical applications. A varied dielectric property is reported even for CCTO ceramic samples prepared in a similar way. Therefore, dielectric response of CCTO is hard to explain clearly. CCTO microstructure is electrically heterogeneous with semiconducting grains and insulating GBs.

The dc conductivity of CCTO is related to grain and grain boundary (GB) resistances as $\sigma_{dc}=A/t(R_g+R_{gb})$, where, A and t are the sample cross-sectional area and thickness, respectively. Since Rgb>>Rg, the overall dc conductivity of CCTO is usually governed by the resistance of GBs for a given sample geometry. Whereas ac conductivity is related to $\sigma_{ac}=\omega\varepsilon_0\varepsilon'\tan\delta$, implying that smaller the ε' or smaller the ac conductivity, it can lead to a low dielectric loss. Therefore, tan δ can be reduced by decreasing the conductivity (or increasing Rgb and Rg).

On the other hand, ε' and tan δ can also be affected by extrinsic factors such as surrounding atmosphere or moisture. There are contradictory reports and mutually exclusive explanation for the CCTO dielectric properties measured in air at RT. Some reports say that there is a highly resistive oxide layer in CCTO sample surface, which is contributing partly to large ε' in CCTO in air at RT. While some other studies showed that CCTO sample surface and electrode contact impedance can be changed depending on the electrode material being used.

Reviewing all those reports indicates that CCTO are not only sensitive to sample processing conditions but also to the atmosphere where the samples are tested. Obviously, there are many open questions concerning the origin of large ε′ in CCTO and hence need to clarify the effect of synthesis conditions, surface layers, GB effect, and surrounding atmosphere on the electrical properties displayed by CCTO ceramics. Therefore, this material still requires careful investigation to identify the reasons for large variations in its properties and ways to achieve a reduced tan δ**.**

The goal of this research is to obtain a fundamental understanding of the dielectric properties of CCTO, which can translate into engineering strategies to enable the development of CCTO as a suitable dielectric material capable of achieving a small tan δ (<0.01) while still maintaining large ε' (10^3-10^4).

The research suggests that significant change in CCTO dielectric properties occur with the modification in electrical resistance and capacitance of the grain and GBs leading to enhanced dielectric properties for capacitor applications. The hypothesis of this research is that *processing conditions (such as sintering and doping), microstructural defects*

(such as GBs, interfaces, and surface layers), and measuring atmosphere can govern the stability and reproducibility of dielectric and electrical properties of polycrystalline CCTO ceramics and consequently control the overall charge transportation across CCTO and related energy storage capabilities as capacitor

3.1 Objectives

Primary objective of this research is to obtain fundamental understanding on dielectric properties of CCTO with low tan δ and large ε' value. The challenge of synthesizing low loss CCTO materials with large-ε' is addressed by preparing phase pure CCTO using simple solid-state method. For enhancing GB capacitance and Rgb, the effects of sample preparation conditions, microstructure, and testing atmospheres on the electrical properties of CCTO are proposed. Optimum CCTO microstructure with enhanced dielectric properties measured in a controlled atmosphere will also be investigated by measuring the impedance spectra of sintered samples. To accomplish this goal, temperature dependence of impedance spectroscopy of the as-prepared CCTO samples with different microstructures are studied in both ambient air and in moisture free environments.

There is a controversy on the origin of large ε' whether it is associated with the sample surface or GBs. Towards this goal we have proposed research in which surface layers are removed by polishing so that thickness dependent CCTO dielectric properties in various testing environments or in a controlled atmosphere can be studied to identify the roles of GBs on dielectric properties. These approaches are expected to provide information on the mechanisms of dielectric loss whether related to surface layers and/or atmosphere.

Feasibility of reducing the loss tangent in CCTO via doping with alumina (Al_2O_3) is also proposed for research. Therefore, electrical properties of Al_2O_3 doped CCTO ceramics are also studied by exposing them to moisture/air free testing environments similar to for the undoped CCTO. It is believed that since Al^{3+} ions are acceptor dopants (ionic charges lower than ions replaced) in CCTO ceramics, which can partially substitute for Ti sites leading to change in oxygen vacancies to balance the charge neutrality. It is also expected that Al_2O_3 dispersed in the CCTO ceramics can create a more insulating second phases such as $CuAl_2O_4$ at GBs while sintering. A reduced conductivity can lead to reduced dielectric losses either by adjusting the defects or changing the concentration of commonly observed native defects such as Ti^{3+}/Ti^{4+}, Cu^{1+}/Cu^{2+}, and other point defects (such as oxygen vacancies and free electrons) in CCTO.

The results of this study are expected to provide a better understanding of the important roles of surrounding atmosphere, sample preparation conditions, and microstructure on the dielectric properties of polycrystalline CCTO ceramics.

2.6 Specific Aims of the Research

The objective of the present work is to synthesize phase pure and Al_2O_3 doped CCTO and to study their dielectric properties.

1. Prepare phase pure and alumina doped CCTO using solid-state route.
2. Study powder processing and sintering behaviors to obtain CCTO ceramic powders that can lead to relatively dense ceramics with a homogenous grain size.

3. Characterize the samples by X-ray diffraction (XRD), scanning electron microscopy (SEM), Energy-Dispersive X-ray (EDX), optical microscopy, Raman Spectroscopy, TGA, particle size, and density measurements.
4. Characterize electrical properties of sintered samples using complex impedance spectra for dielectric properties to find the conditions at which impedance, ε', and dielectric loss is varied due to the applied external effects such as temperature, frequency of the applied electric field, and testing atmosphere.
5. Investigate effect of the sample thickness and microstructure produced by sintering at different temperatures on the measured dielectric properties in different atmospheres, temperatures, and frequencies.
6. Study the effect of Al_2O_3 doping on the electrical properties of CCTO, including the effect of dopant concentration, microstructure, temperature, and testing environment.
7. Analyze and model impedance data to separate contributions from grain and GBs.
8. Model the dielectric properties to study the roles of the microstructure, sample thickness, temperature and testing environments on the grain and GBs resistances to identify the mechanisms controlling the dielectric properties and loss tangent of CCTO.

CHAPTER IV

EXPERIMENTAL PROCEDURE AND DATA ANALYSIS

4.1 Powder Processing and Sintering of Polycrystalline CCTO Materials

Figure 4.1 shows the flow chart of powder preparation and processing conditions. As shown in Figure 4.1, pure CCTO powder was synthesized by solid-state reaction using stoichiometric ratio of the $CaCO_3$ (VWR, 99.95%), CuO (VWR, 99.7%), and TiO_2 (Sigma-Aldrich, Anatase 99.8%). The raw materials were mixed in ethanol and ball-milled for 24 h in a polyethylene bottle containing zirconia media. The mixed slurry was dried and then calcined at the temperature of 850°C for 6 h in air. Calcined powders were mixed in ethanol and then reground in the ball mill for 72 h using zirconia grinding media. Finely ground wet-slurry of calcined powders were dried sieved using 120 μm sieve.

Average particle size for all the calcined powders was analyzed using Malvern Zetasizer Ver. 7.11 instruments. As can be seen in the flow chart in Figure 4.1, the calcined and sieved CCTO powders were mixed with 0.5 weight % PVB in ethanol.

Binder-added and dried CCTO powders (~1.6g) were uniaxially pressed at 165 MPa into 13 mm diameter and 2.5 mm thick green pellets. De-binding of the pressed pellets was performed at 500°C for 2 h followed by pre-sintering at 950°C for 5 h and then sintering at different temperatures from 1050°C to 1115°C for 5 h. All the heat treatments of green pellets were carried out at a constant heating and cooling rate of 2°C/min. Densities of the sintered pellets were determined using Archimedes method.

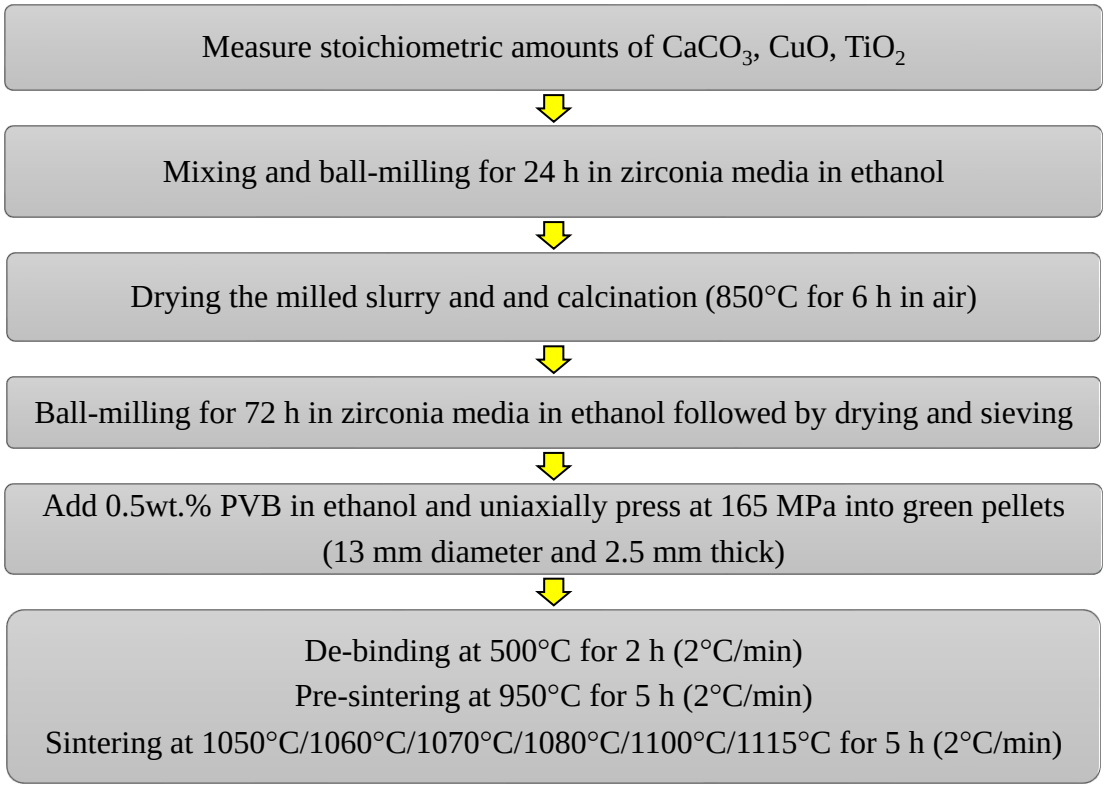

Figure 4.1. Flow chart for CCTO powder preparation and sintering.

The samples, which were sintered for 5 h at 1050°C, 1060°C, 1070°C, 1070°C, 1100°C and 1115°C, respectively, are designated as S1050, S1060, S1070, S1080, S1100, and S1115.

4.2. Characterization of Phase Purity and Microstructure

In order to identify the decomposing temperatures, thermogravimetric analysis (TGA, Netzsch STA 449 F1 Jupiter) was carried out for pre-calcined CCTO precursors at RT-900°C at a heating rate of 5°C/min in static air.

X-ray diffraction (XRD) is an analytical technique used for structural characterization and phase identification of polycrystalline materials. In order to identify the calcination temperature, XRD was also carried out to confirm the phases present at various temperatures. XRD (Bruker AXS D8 Discover) with Cu-Kα radiation was used in this research to characterize the phases and structural variations in the precursor powders and sintered ceramics with the wave length of 1.541 Å and the scan rate of 0.01º/s, with 2θ varying from 20º to 80º, and a count time of 60 s.

Raman Spectroscopy (Almega XR, Dispersive Raman) was used for calcined powders and sintered CCTO samples in searching for variations in of the Raman lines corresponding to different types of atomic motions. Morphology of precursor powders and the microstructure of sintered samples were examined at RT by Scanning Electron Microscope (SEM, Hitachi S-4800) and optical microscopy. Furthermore, Energy-Dispersive X-ray (EDX) was used for identifying the type of elements as well as the percentage of the concentration of each element in the sintered CCTO samples.

4.3 Characterization of Electrical Properties by Complex Impedance Spectra

For electrical impedance measurements of as-prepared (pure and alumina doped) and thinned down samples, platinum paint electrode was used. Before applying the platinum

paints, CCTO samples were carefully cleaned by ultra-sonicating with acetone. For this, platinum paint (Heraeus conductive paints Pt A2757) was applied on the pellets to serve as metallic contacts to the sample. The electrodes were cured by heating the platinum painted samples at a rate of 2°C/min to 600°C and holding for 2 h to burn off the solvent/binder. Similarly, to study the thickness effect, platinum paint electrodes were re-applied on the opposing surfaces of the pellets (S2) upon thinning down and cured the electrode at each stage at 600°C for 2 h.

To investigate the dielectric and charge transport properties of the studied materials, the main experimental technique used in this research is broadband dielectric spectroscopy, also known as complex impedance spectroscopy. Impedance spectroscopy (IS) has been used as a powerful method to explain the barrier layer capacitance effect of the CCTO ceramics. Complex IS enables studying the dynamics of permanent dipoles and induced mesoscopic dipoles, and the conduction properties of materials in a single experiment. Therefore, IS data in the current research help in identifying and separating the contributions of grains and GBs to bulk dielectric properties of CCTO ceramics. Real (Z') and imaginary parts (Z'') of the complex impedance (Z*) as given in equation 4.1 is separately measured by IS.

$$Z^* = Z' - jZ'' \qquad (4.1)$$

Where, j is the imaginary constant and Z', Z'' are real (resistive) and imaginary (capacitive) parts of Z*. Real part (Z') represents the ohmic resistance whereas and the imaginary part (Z'') represent the reactance due to capacitive or inductive resistance. Therefore, Z* can be used to understand the electrical properties of CCTO ceramics.

In the first set of experiments, the real and imaginary parts of the complex impedance of CCTO (S1060, S1070, S1080, S1100, and S115, respectively) were separately measured in air atmosphere at various temperatures from 23°C to 225°C using Solartron 1260A with the dielectric interface (Solartron 1296). The temperature was measured by a thermocouple mounted closer to the sample inside the tube furnace. Data acquisition was handled by a personal computer. For complex impedance characterization, a signal strength of 100 mV using two-probe method in the frequency range from 1 Hz to 4 MHz were used. Three measurements were made at various heat/cool cycles between 23°C and 225°C while keeping the identical samples in both air atmosphere.

In the second set of experiments, the impedance measurements were carried out in a dry N_2 atmosphere without removing the samples from the horizontally arranged quartz tube inside the tube furnace, which has the provision for evacuation under pressure of about 0.09 MPa and back-filling with dry N_2 as shown in as shown in Figure 4.2. Before impedance measurements in N_2 atmosphere were carried out, the samples were thermally treated by heating them up to 400°C in dry N_2 and then evacuating the chamber for 30 minutes to remove any water vapor/air and back-filled with N_2 at the same temperature and cooled to RT. This system could maintain air and dry N_2 atmospheres inside the tube furnace.

Later, during three temperature programmed heating/cooling cycles, the samples (S1060, S1070, S1080, S1100, and S1115, respectively) were kept in N_2 at three heat/cool cycles between 23°C and 225°C. At each heating cycle, the chamber was evacuated for 30 minutes at 225°C and back-filled with N_2 before cooling cycles were started. Complex

impedance of the leads/instrument impedance was separately measured and was subtracted from the data before interpretation.

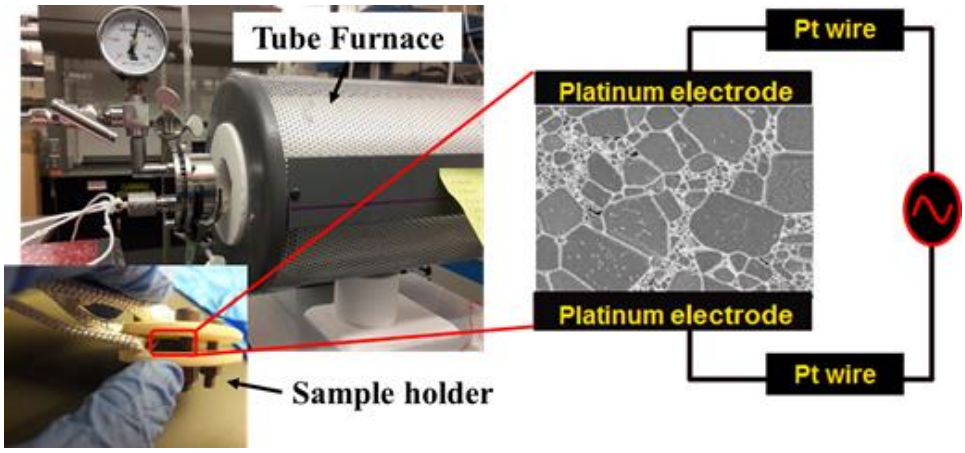

Figure 4.2. Complex impedance measurement test setup at various atmospheres and temperatures.

The stability of the impedance data had been determined by testing through three consecutive heat cool cycles. The stability of the and the performance of the experimental set-up was determined by testing the known resistors and capacitors that were connected in series and parallel.

4.4 Impedance Analysis and Interpretation of Dielectric Properties

Impedance Spectroscopy: After real and imaginary parts of the complex impedance were experimentally measured over a range of frequencies, a comparison or fitting was carried out using an equivalent circuit approach. This equivalent circuit was chosen by considering the physical processes taking place within the CCTO. Fitted data can be used to interpret and calculate values of the respective elements in the electrically

heterogeneous microstructure of CCTO. Graphical representation of the real and imaginary parts of the complex impedance in the complex plane are the Cole-Cole diagrams. The Cole-Cole plots appear as one, two or three semi-circular arcs as shown in Figure 4.3, if the resistances (R) and capacitances (C) of different regions such as grain, GB, or electrode in the materials are connected in parallel connection. Therefore, the shape and the width of the arcs (Z' vs. Z'') indicate the type of relaxation mechanism for the grain, GB, or electrode effect, respectively. The arc closest to the origin i.e. at high frequency represents the bulk resistance (grains), whereas the non-zero intercept at low frequency represents the total resistance.

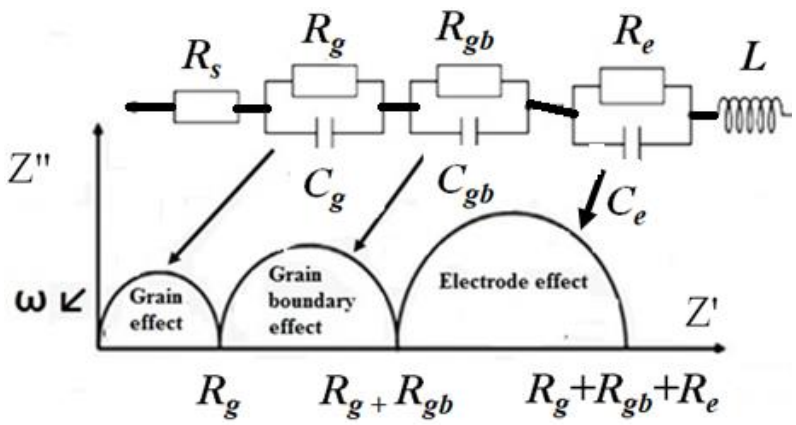

Figure 4.3. complex impedance spectra for CCTO ceramics with equivalent RC circuits, where Cg, Cgb, and Ce, Rg, Rgb, and Re are grain, grain boundary, and electrode capacitances and resistances, respectively. Rs and L, respectively are contact resistance and inductance.

Equivalent circuit for different relaxations caused by semi-conducting grains, electrically insulating grain boundaries, and electrode will all be represented by three parallel RC pairs connected in series as shown in Figure 4.3. At the maximum of each arc $\omega_{max}\tau=1$,

where, τ (τ=RC) is the relaxation time of the respective physical elements and $\omega=2\pi f_{max}$ is the angular frequency and f_{max} is the peak frequency [131]. Single RC represents the relaxation time of one mechanism. Several curves mean more than one RC elements in the investigated sample.

By extrapolating the semicircle at the low frequency end to intersect the x-axis the value of total resistance of the equivalent circuit was determined. The horizontal axis Z' is the real part of the complex impedance and the vertical axis Z'' is the imaginary part of the complex impedance. The capacitance, C can be determined by the maximum of each arc. Debye relaxation (single relaxation time) appears only in perfect crystals. The arcs for Debye response can be fitted using an ideal capacitor, C and resistor, R. The corresponding complex impedance is then of the form as given in equation 4.2.

$$Z^* = \frac{R}{1+j\omega RC} \tag{4.2}$$

For polycrystalline materials, the electrical conduction cannot be attributed to a single relaxation time due to heterogeneity in the material. If there is no electrode effect, Rg and Rgb contributions to real and imaginary parts of the complex impedance can be derived as shown in equations 4.3 and 4.4 considering ideal capacitances (Cg and Cgb) for grains and GBs.

$$Z' = \frac{R_g}{R_g + \left(\omega R_g C_g\right)^2} + \frac{R_{gb}}{R_{gb} + \left(\omega R_{gb} C_{gb}\right)^2} \tag{4.3}$$

$$Z'' = \frac{\omega R_g^2 C_g}{R_g + \left(\omega R_g C_g\right)^2} + \frac{\omega R_{gb}^2 C_{gb}}{R_{gb} + \left(\omega R_{gb} C_{gb}\right)^2} \tag{4.4}$$

Where, C_g and C_{gb} are capacitance of grain and GB, respectively. On the other hand, as the grain and grain boundaries are not ideal RC elements (non-Debye), the corresponding complex impedance is of the form given Cole-Cole expression in equation 4.5. Illustration in Figure 4.4 (a) and (b), respectively show the ideal Debye relaxation and Cole-Cole relaxation, which explains the non-ideal Debye nature when center of the semicircle is lying below the real impedance axis, where $0 < \beta \leq 1$.

$$Z^* = \frac{R}{1+(j\omega RC)^{\beta}} \qquad (4.5)$$

The smaller the value of β, the more asymmetric the resulting semicircle becomes. As β approaches 1, Debye type relaxation is regained. The value of β are obtained by measuring the angle (βπ/2) between Z' axis and the tangent to Z' verses Z'' curve at the origin (0,0). Smaller the value of β large the deviation from ideal Debye nature. When β reaches to 1 it represents semicircle with center lying on x axis, which represent the departure from ideal Debye nature of the polycrystalline CCTO [60].

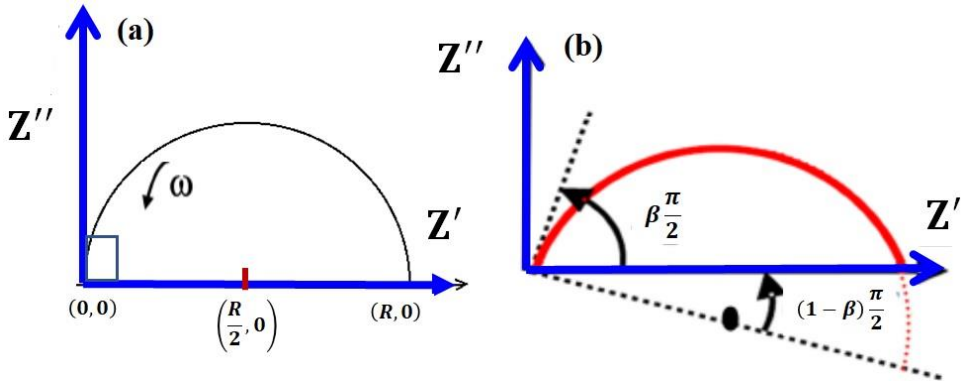

Figure 4.4. Complex impedance plane plots showing (a) ideal Debye and (b) Cole-Cole type relaxations, respectively.

As can be seen in Figure 4.4 (a) and (b), respectively, β becomes smaller as the width of the distribution of relaxation time is larger indicating a greater deviation with respect to the Debye-type relaxation. To correctly fit the experimental data, impedance data can be modeled using a modified Cole–Cole expression representing the grain and GB in CCTO ceramics. Cole–Cole expression derived for two parallel RC circuits connected in series is represented in equations 4.6 and 4.7.

$$Z' = \frac{R_g}{\left[R_{g+}(\omega R_g C_g)^{\beta g}\right]} + \frac{R_{gb}}{\left[R_{gb+}(\omega R_{gb} C_{gb})^{\beta gb}\right]} \quad (4.6)$$

$$Z'' = \frac{\omega {R_g}^2 C_g}{\left[R_{g+}(\omega R_g C_g)^{\beta g}\right]} + \frac{\omega {R_{gb}}^2 C_{gb}}{\left[R_{gb+}(\omega R_{gb} C_{gb})^{\beta gb}\right]} \quad (4.7)$$

Where, βg and βgb are two exponent parameters with 0 < βg, βgb ≤1. (what is meant here), which represent the departure from ideal Debye nature of the polycrystalline CCTO [132]. The model-fitted data and their dependences on the microstructure, temperature, and testing environments are then used for gaining a mechanistic understanding of the dielectric properties of CCTO.

In the present study, the impedance analysis was carried out with numerical least-squares minimization using Microsoft Excel Solver. Complex impedance of the leads/instrument impedance were subtracted from the data before interpretation and the root sum of squares of relative deviations between measured data and expected values were minimized. Estimated initial Cole parameters were used for solving the least squares problem to achieve a better fit to the data with 0.1% precision followed by successive refinements.

Complex Relative Permittivity and Dielectric Loss: Dielectric materials can be defined as materials with high electrical resistivity, which are able to store electrical energy in the form of electrostatic charge in the devices. Dielectric function (i.e. complex relative permittivity) is related to real and imaginary parts of the dielectric constant by $\varepsilon^{*}=\varepsilon'-i\varepsilon''$. Where, ε' and ε'' are the real and imaginary parts of the complex relative permittivity and are dependent on the frequency and temperature. The real part describes the dispersion, whereas the imaginary part describes the absorption. The dielectric function can be obtained by measuring the amplitude of the current through the capacitor and its relative phase with respect to the voltage, thereby measuring the complex impedance $Z^{*}(\omega) = V^{*}(\omega)/I^{*}(\omega)$ of the sample. Since for a capacitor of capacitance C the complex impedance is $Z^{*} = 1/i\omega C$, the frequency-dependent complex dielectric function is then given, as shown in equation 4.8.

$$Z^{*} = Z' - jZ'' = \frac{1}{j\omega C_0 \varepsilon^{*}} \qquad (4.8)$$

Therefore, real and imaginary parts of the complex dielectric function can be estimated using real and imaginary parts of Z^{*} as give equations 4.9 and 4.10.

$$\varepsilon' = \omega C_0 Z'' \qquad (4.9)$$

$$\varepsilon'' = \omega C_0 Z' \qquad (4.10)$$

Where, ω is the angular frequency given by $\omega=2\pi f$ and f is the frequency. Here, C_0 is the capacitance of a parallel plate capacitor filled with vacuum, which is given by the relation, $C_0 = \varepsilon_0 A/d$, where, C_0 is the capacitance of the empty capacitor with electrodes

of surface area A separated by a distance d. Therefore, the value for C_0 in this work can be obtained from a measurement of the empty cell or directly from the knowledge of the geometry of the cell. The geometry of the cell was determined by measuring the diameter, which is the separation area of the platinum electrodes and pellet thickness, which is the separation between two platinum electrodes. For pure ohmic conduction the real part of ε* is independent of frequency while for non-ohmic conduction or polarization effects (at inner boundaries or external electrodes) the real part of ε*(ω) increases with decreasing frequency. This way, the real and imaginary parts of the frequency dependent complex dielectric function was determined, and dielectric function was analyzed for various samples in air and dry N_2 in the current theses. The measured values of real and imaginary parts of the complex impedance can also be used to compute dielectric loss tangent (tan δ) and AC conductivity (σ_{ac}) as shown in eqns. 4.11 and 4.12 using the standard conversion.

$$\tan\delta = \frac{\varepsilon''}{\varepsilon'} = \frac{Z'}{Z''} \tag{4.11}$$

$$\sigma_{ac} = \varepsilon_0 \varepsilon'' \omega \tag{4.12}$$

Here, ε_0 is the permittivity of vacuum.

Temperature Dependence of the DC Conductivity: Once the dc resistance has been determined with the equivalent circuit method as described in the previous sections, the temperature dependence of the dc conductivity can be analyzed. In practice, Arrhenius equation is commonly used to display the temperature dependence of the dc resistance (R). DC resistance is related to the DC conductivity, by σ_{dc} = t/(AR) of a ceramic sample.

Where, t is the sample thickness and A is the cross-sectional area of the electrode. The mathematical expression characterizing the temperature dependence of the rate dc conductivity, which can be expressed in terms of the reciprocal of the measuring temperature (1/T) by an Arrhenius relation as given in equation 4.13 [133],

$$\sigma_{dc} = \sigma_0 \exp(-E_a/k_B T) \qquad (4.13)$$

Where, σ_{dc}, σ_0, E_a, and k_B are the DC conductivity, the independent pre-exponential factor, the activation energy, and the Boltzmann constant, respectively. Linearization of equation 4.13 shows up as a straight line when the ln (R) versus the inverse temperature is plotted (the so-called Arrhenius plot) and the slope of this line is proportional to the activation energy. In the current research, the following mathematical treatment was carried out to obtain linearized expression for the equation 4.13.

$$\ln \sigma_{dc} = ln\, \sigma_0 - E_a/(k_B T)$$

$$\ln \sigma_{dc} = \ln (t/A) - \ln(R)$$

$$\ln (t/A) - \ln(R) = ln\, \sigma_0 - E_a/(k_B T)$$

$$-\ln(R) = ln\, \sigma_0 - \ln (t/A) - E_a/(k_B T)$$

$$\ln(R) = (E_a/k_B)\frac{1}{T} + [\ln (t/A) - \ln \sigma_0]$$

CHAPTER V

CCTO POWDER PROCESSING AND SINTERING

In this chapter, results of $CaCu_3Ti_4O_{12}$ calcined powder and sintered ceramics fabrication are presented. Results of the characterization of phase purity, microstructure using XRD, SEM, Raman spectroscopy, and EDS as well as the results of density of sintered samples will also be addressed.

5.1 CCTO Powder Synthesis and Sintering

Pure CCTO powder was synthesized using stoichiometric ratio of solid-state precursors $CaCO_3$, CuO, and TiO_2. The color of dried pre-calcined precursor powders after mixing and ball milling (using zirconia media in ethanol) was grayish black as can be seen in Figure 5.1 (a). After calcination at 850°C for 6 h, the color of pre-calcined powders was changed from grayish to yellowish as can be seen see Figure 5.1 (a) and (b). Furthermore, the appearance of green pellets prepared using finely ground calcined powders turned black color when they were sintered between 1060°C and 1115°C for 5 h as can be seen in Figure 5.1 (c).

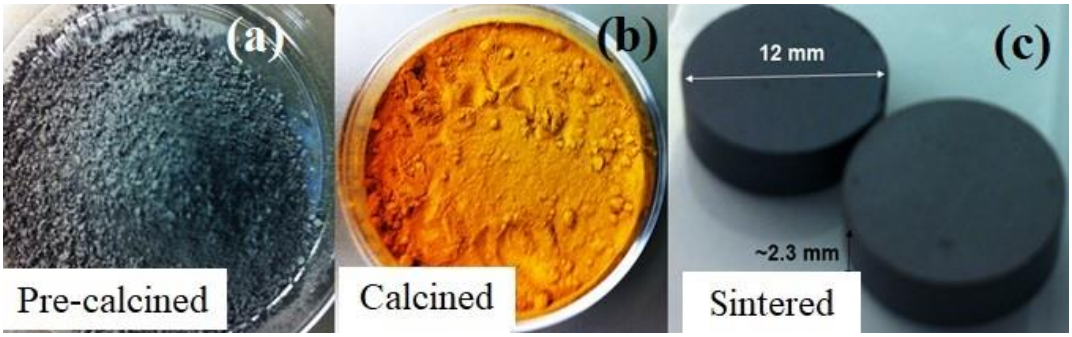

Figure 5.1. (a) Ball-milled and mixed pre-calcined powders, (b) calcined powders at 850°C for 6 h, and (c) sintered pellets at 1060-1115°C for 5 h.

The average particle size of the calcined and sieved powders was measured as 500 nm. Similar particle size range (200-500 nm) was observed in SEM micrographs as well. Figure 5.2 (a) and (b) are two different magnifications of homogeneously distributed CCTO calcined powder morphologies.

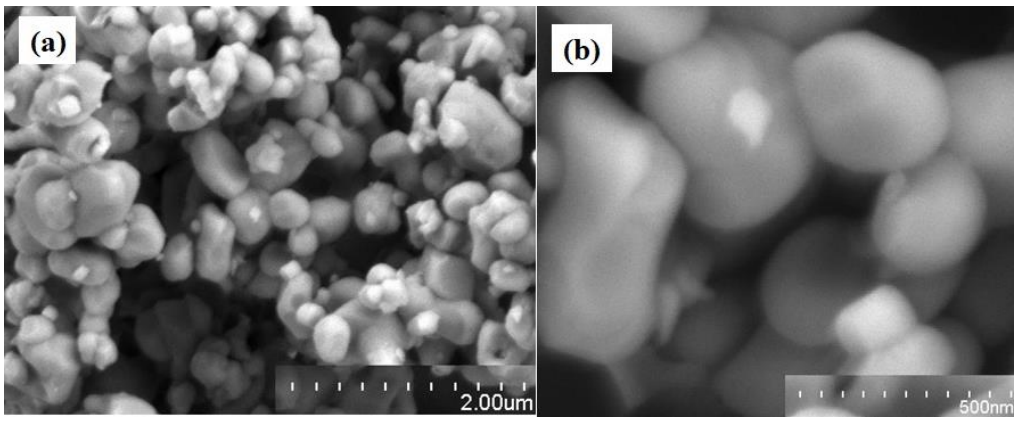

Figure 5.2. (a) and (b) are two different magnifications of SEM micrographs of pure-CCTO powders calcined at 850°C for 6 h showing the particle size as small as 200-500 nm.

5.2 Analysis of Phase Evolution, Chemical Composition, and Microstructure

To determine the decomposition temperatures of CCTO pre-calcined powders, TGA was used. Figure 5.3 shows the TGA curve of pre-calcined CCTO precursors. The main mass loss observed approximately up to 600°C was nearly 9%, which is due to decomposition of the organic groups such as PVB binder, carbonate, ethanol, and moisture. Relatively negligible weight loss beyond 700°C indicates that crystalline oxides are slowly reacted to form polycrystalline CCTO powders when heating them above 700°C.

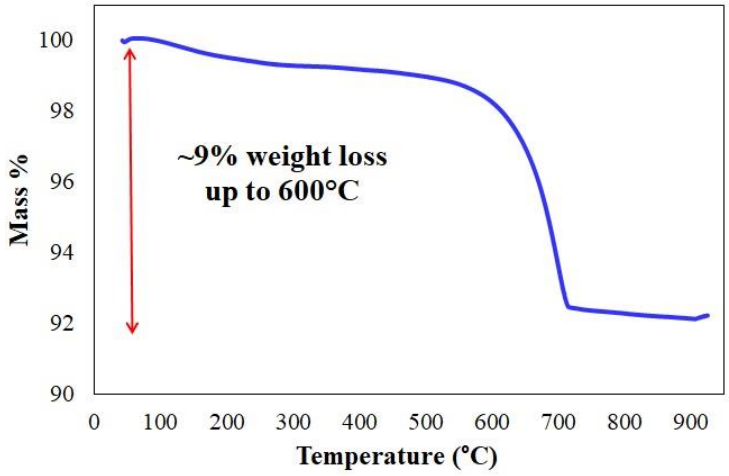

Figure 5.3. TGA for pure-CCTO pre-calcined precursors at a heating rate of 5°C/min in static air from room temperature to 900°C.

After determining the range of temperature at which no further weight loss in the TGA curve, XRD was also carried out to identify the phases present in the pre-calcined, calcined, and sintered CCTO samples. XRD patterns for the evolution of CCTO phases upon calcination of the powders in the temperature range of 650-850°C for 6 h are shown in Figure 5.4. As can be seen in Figure 5.4 (a), secondary phases are diminished upon

heating above 750°C indicating a higher crystallinity and complete conversion to CCTO phase.

As can be seen in Figure 5.4 (a), secondary phases are diminished upon heating above 750°C indicating a higher crystallinity and complete conversion to CCTO phase. The lowest temperature at which single-phase CCTO powders with a cubic structure are formed is at a calcination temperature of 850°C for 6 h. Therefore, for the current experiments, the calcination temperature was fixed at 850°C for 6 h. As can be seen in Figure 5.4 (b), sintered ceramics (at 1060-1100°C for 5 h) show strong CCTO related peaks with no observable secondary phases.

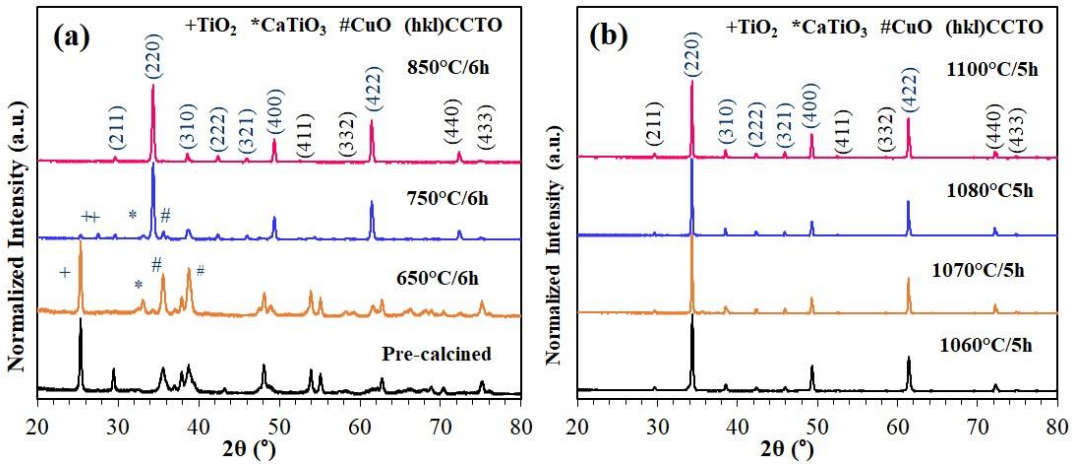

Figure 5.4. XRD patterns of CCTO (a) pre-calcined powders upon calcination at 650-850°C for 6 h and (b) sintered at 1060°C, 1070°C, 1080°C, and 1100°C for 5 h.

Raman spectroscopy measurements for calcined powders at 850°C for 6 h and surface of sintered pellets are shown in Figure 5.5. Three theoretically predicted symmetry modes were observed and the description of them is provided in Table 5.1. The theoretical values of two of them are at 428 cm^{-1} (Ag1) and 512 cm^{-1} (Ag2), respectively, which are

assigned to TiO_6 rotation like modes. The peak at 576 cm^{-1} (Fg3) is assigned to the Ti-O-Ti anti-stretching mode of the TiO_6 octahedra.

Upon sintering the green (calcined) CCTO pellets, the peak position of the of Ag (2) (510 cm^{-1}) band, which is associated to rotation (or tilting) modes of the TiO_6 octahedron is increased from 504 cm^{-1} to 511 cm^{-1} while the peak position of the Fg (3) (510 cm^{-1}) band, which is associated with anti-stretching modes of the O-Ti-O is increased from 565 cm^{-1} to 575 cm^{-1}. It has been previously shown that the Raman peaks shift to longer wave numbers in Ti-deficient samples compared to those of (nominally) stoichiometric CCTO [134]. In the current study, increasing the sintering temperature has not significantly shifted the peak position or broadened the shape of these two rotational peaks. This indicates the presence of symmetry despite the changes in the sintering temperatures.

Table 5.1. Theoretical and experimental values of the main atomic motions of the Raman peak positions of CCTO calcined powder at 850°C for 6 h and sintered samples at different temperatures from 1060°C to 1100°C for 5 h.

Sample	$A_g(1)$ cm-1	$A_g(2)$ cm-1	Fg(3) cm-1
	TiO_6	TiO_6	O-Ti-O
	Rotation like vibration	Rotation like vibration	Anti stretching mode
Theoretical	**428**	**512**	**574**
Calcined	443	504	565
S1060	445	511	575
S1070	445	511	574
S1080	444	510	574
S1100	444	511	575

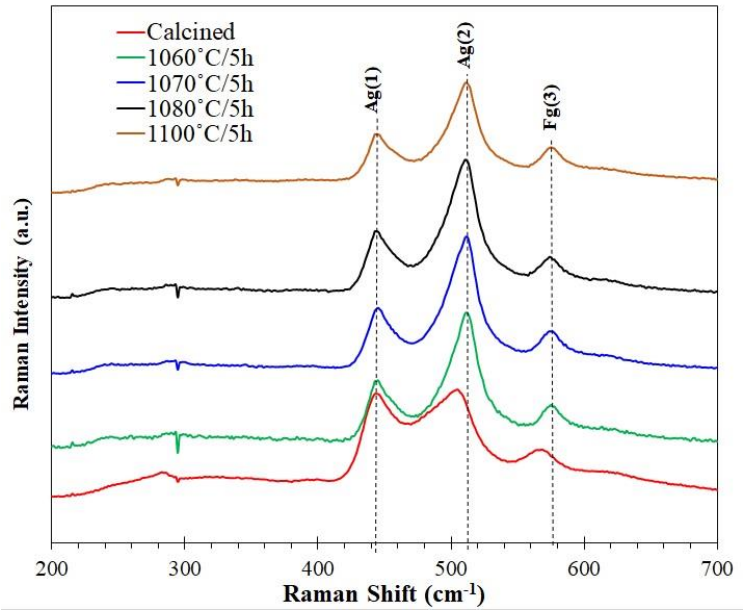

Figure 5.5. Raman spectra of pure CCTO calcined powders at 850°C for 6 h and as-sintered samples for 5 h, respectively at various temperatures from 1060°C to 1100°C.

SEM micrographs in Figure 5.6 (a)-(d) show the evolution of microstructure of polished and sintered CCTO samples prepared at different temperatures (1050-1080°C) with an equal sintering cycles in terms of heating/cooling rates (2°C/min) and holding time (5 h). Figure 5.6 (a) clearly shows the initiation of discontinuous grain growth when CCTO samples are sintered at 1050°C for 5 h.

When increasing the sintering temperature, most of the grains have grown in to a wide range of distribution. As seen in Figure 5.6 (a)-(d) duplex nature grain growth with no clear GBs indicates an incomplete grain growth until 1080°C. All the samples in Figure 5.6 show that much larger grains are about 20-25 μm apart and the space between them is filled with large numbers of small grains about 1-2 μm.

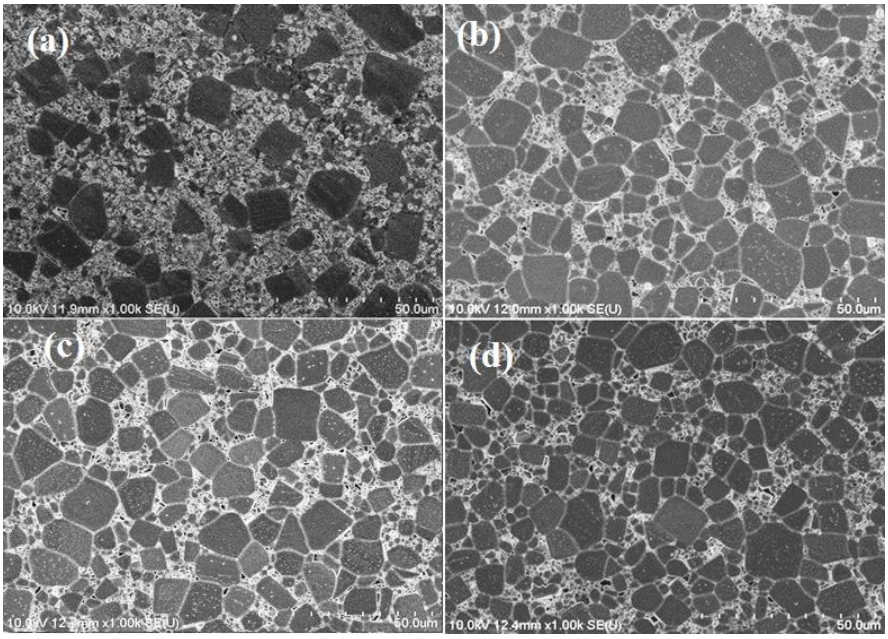

Figure 5.6. SEM micrographs show evolution of microstructure of pure-CCTO ceramics (a) S1050, (b) S1060, (c) S1070, and (d) S1080.

Figure 5.7 shows the optical micrographs of the polished sample surfaces when increasing the temperature from 1060°C to 1080°C. The dark regions in all the micrographs are grain pullout during polishing. As shown by optical micrographs, all the samples have large sized grains (<20 μm) with large number of smaller grains. However, the amount of smaller sized grains has decreased when increasing the sintering temperature.

To further clarify the effect of CCTO sintering temperature on CCTO microstructure, sintering was carried out at high temperature at 1100-1115°C, respectively for 5 h to obtain homogeneously distributed grains with clear GBs. Optical micrographs in Figure 5.8 show the sample sintered (S1115) has the continuous grain growth with clear GBs

with relatively narrow grain size distribution. S1100 has islands of large grains (>20 μm) surrounded by relatively large number of smaller sized grains compared to S1115.

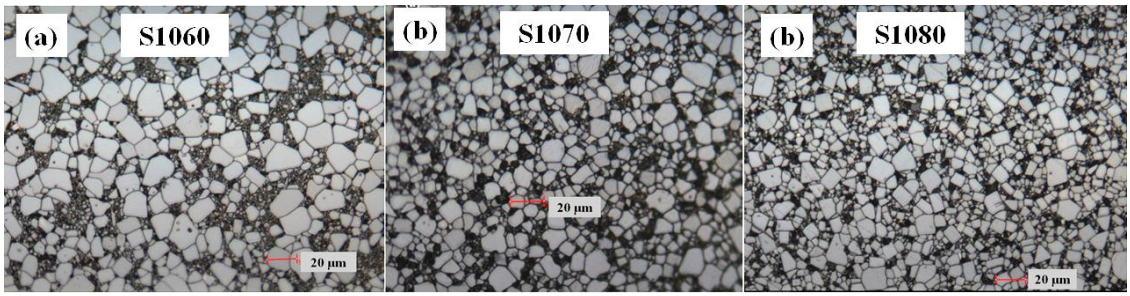

Figure 5.7. Optical micrographs show the evolution of microstructure of pure-CCTO ceramics (a) S1060, (b) S1070, and (c) S1080. The dark regions are pullout during polishing.

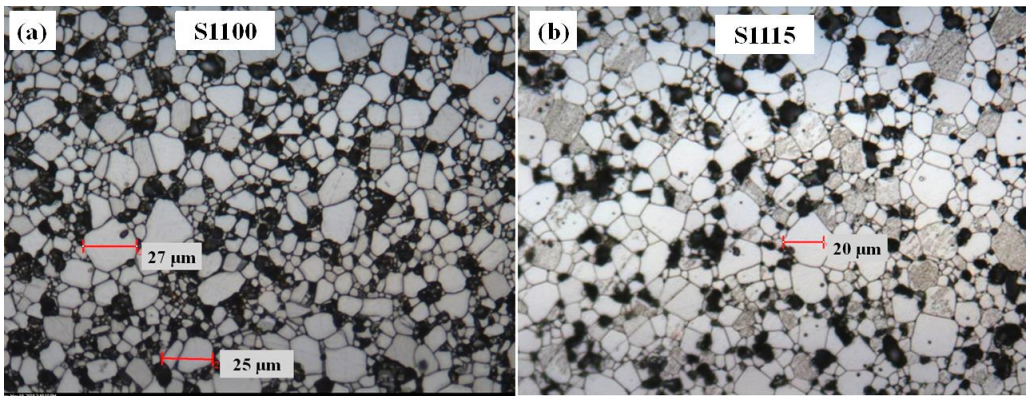

Figure 5.8. Optical micrograph of pure-CCTO sample (a) S1100 and (b) S1115 (sintered at 1100-1115°C, respectively for 5 h) shows more grain growth with clear grain boundaries. The dark regions are pullout during polishing.

SEM images of fractured surface in Figure 5.9 (a) confirm the duplex nature of microstructure even when increasing the sintering temperature up to 1100°C (S1100). S1100 has relatively larger grains > 20 μm within some smaller sized grains about 2 μm.

As-sintered surface image of S1100 as can be seen in Figure 9 (b) further indicates a wide grain size distribution.

The average grain size distribution calculated using line intercept method using ImageJ software for S1060, S1070, S1080, S1100, and S1115 are 4.95 ± 0.38, 5.02 ± 0.17, 4.57 ± 0.23, 6.86 ± 0.15, and 7.94 ± 0.48 indicating largest average grain size for S1100 and S1115.

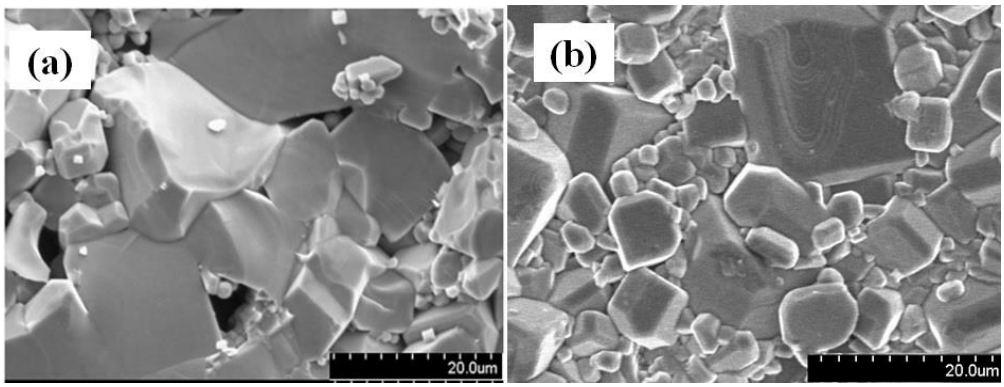

Figure 5.9. SEM micrographs of CCTO sintered sample (a) show the fractured and (b) as-sintered surfaces of S1100, respectively.

Sintering behavior of CCTO ceramics was further evaluated using density measurements based on Archimedes principle. Figure 5.10 (a) is the graphical representation of the measured bulk density of sintered ceramics at 1050-1115°C, respectively for 5 h.

When the sintering temperature is increased from 1050°C to 1115°C, relative density increases to a maximum value of 4.735 ± 0.065 g/cm^3 (94% of the theoretical density - 5.049 g/cm^3) at 1060°C and decreases to a value of 4.439 ± 0.050 g/cm^3 at 1100°C then increases slightly to a value of 4.585 ± 0.019 g/cm^3 at 1115°C. Density of the sample

sintered at 1070°C for 5 h is 4.669 ± 0.042 g/cm^3 (92%) is relatively within the density variation observed for sample sintered at 1060°C. The lowest density is observed for sample sintered at 1050°C for 5h, which is 4.326 ± 0.028 g/cm^3 (86%) and hence was excluded for measurements of electrical properties due to its low density. As can be seen in Figure 5.10 (b), largest density of S1060 was confirmed at 1060°C for 5 h by varying the sample dwell time 3, 5, 10, and 15 h, respectively (at 1060°C).

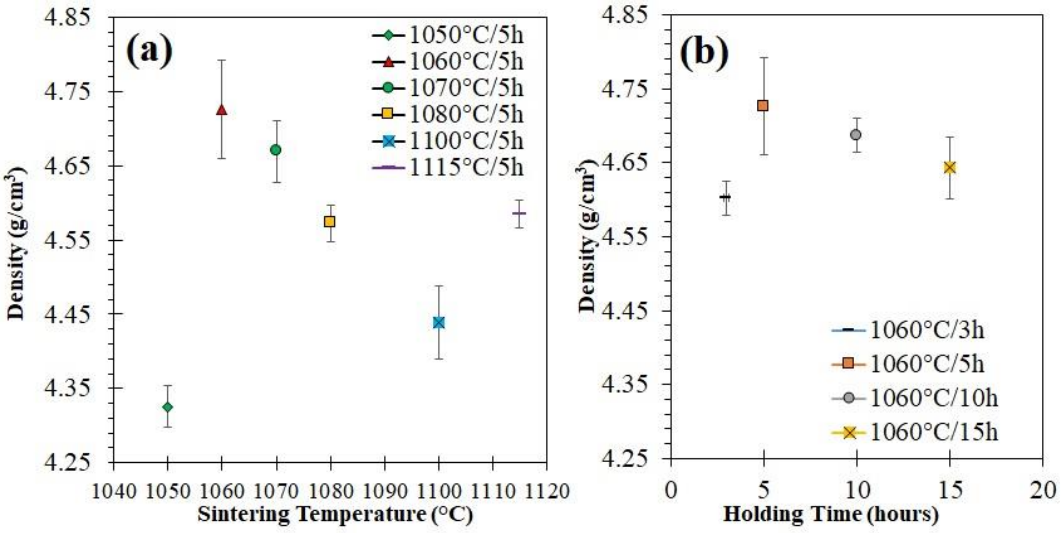

Figure 5.10. Density of CCTO ceramics prepared at (a) various sintering temperatures from 1060°C to 1115° and (b) at 1060°C for various holding times 3, 5, 10, and 15 h.

Reports related to CCTO sintering studies indicated copper melting aid the sintering leaving the bigger sized grains remained to be stoichiometric while smaller sized grains be copper rich [38]. Therefore, compositional variations of the densest sample sintered for 5 h at 1060°C was carried out. According to EDS analysis in CCTO sample displayed in Figure 5.11, no significant compositional variations was observed in larger verses smaller grains. The nearly stoichiometric ratio of the weight percentage (wt.%) of all the

elements as per the EDS analysis indicates homogeneous composition of CCTO grains throughout the smaller and larger grains.

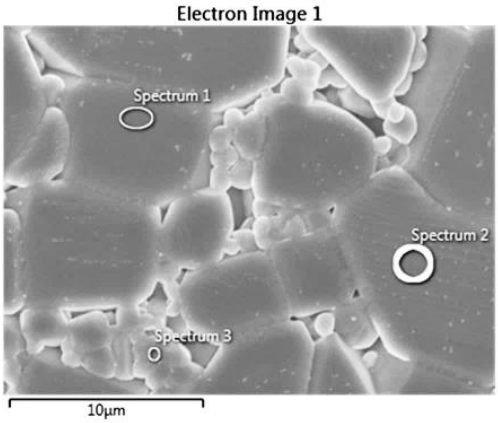

Element (Wt%)	Spectrum 1	Spectrum 2	Spectrum 3
O	31.23 ± 1.19	30.66 ± 1.2	31.69 ± 1.14
Ca	6.68 ± 0.4	7.25 ± 0.41	6.27 ± 0.38
Ti	32.95 ± 0.94	32.61 ± 0.95	31.2 ± 0.89
Cu	29.15 ± 1.12	29.48 ± 1.16	30.84 ± 1.11
Total:	~100	~100	~100

Figure 5.11. EDS analysis in different sizes of grains: spectrum 1, spectrum 2, and spectrum 3 are three different grains on the polished sample sintered for 5 h at 1060°C.

CHAPTER VI

INFLUENCE OF ATMOSPHERE ON THE DIELCTRIC PROPERTIES OF CCTO CERAMICS

Contents published in *J Am Ceram Soc.* and in *Trans. Indian Inst. Met.* (Samarakoon et al., 2019)

Chapter Abstract: This study investigated the effect of testing atmospheres such as air and dry N_2 on the stability and reproducibility of the electrical properties displayed by CCTO ceramics. Solid state reaction method is used to synthesize phase pure CCTO powders, which are used to fabricate dense samples by sintering. Samples with different microstructures are obtained by sintering at different temperatures of 1070°C and 1100°C. AC impedance spectroscopy is used to study the effects of testing atmospheres, temperatures, microstructures and frequency on the dielectric properties of the sintered samples. Highly irreproducible dielectric properties are observed upon testing in ambient conditions. Stable and reproducible dielectric properties are only obtained in dry N_2. Re-exposing the same CCTO samples back into ambient air after treating in dry N_2 restored irreproducibility

The results from this study suggested that the role of moisture/air in the ambient on the dielectric properties should not be over-looked and is expected to play a key role in controlling the stability of dielectric properties of CCTO. This new approach of characterizing the CCTO ceramics can be used as guide lines to eliminate hysteresis due to ambient atmosphere and to produce stable and reproducible dielectric properties useful as capacitors.

6.1 Introduction

The stability and irreproducibility of dielectric properties displayed by CCTO ceramics is of most concern, when they are used as capacitor dielectrics. However, reports indicate that electrical impedance of CCTO measured in air at RT can change either by moisture, oxygen absorption, or due to changes in the electrode material.

CCTO ceramics and thin films are multifunctional due to its gas [13, 135, 136] and moisture sensitivity [55, 56]. Humidity sensitivity of CCTO ceramics [55, 56] and thin films [57] have been recognized only by limited studies by two groups. Two publications [55, 56] on CCTO ceramics demonstrated that the adsorption of water molecules can affect the potential barrier layer formed at the interfaces and hence can affect the inherent dielectric properties.

Other moisture sensitive ceramics have shown that adsorbed moisture sits preferably on active surface sites such as pores and defects, which can then modify the conduction paths [125, 126, 130]. Mechanism of humidity interaction with metal oxides depends mainly on the bulk properties such as microstructure, pore size and volume, grain size,

and defects [130]. Various surface reactive sites enhance moisture adsorption on the oxide ceramics [125]. Moreover, the moisture absorption during storage of the CCTO ceramics in high humidity environments or even at normal laboratory conditions might cause breakdown and failures due to change in conductivity of the material. In ambient air atmosphere, surface reactive sites can adsorb molecular O^{2-} and OH^{-} ions at low temperature [125], which can travel due to the applied AC electric field and affect the overall complex impedance [125, 137].

However, some research work indicated that impedance near RT undergo a dramatic change when the CCTO samples were aged in air due to adsorption of oxygen on the sample surface [23]. Some studies stressed that there is a large variations or instability of the dielectric constant/loss factor at low frequency due to the changes in the migration of oxygen vacancies across sample electrode contact at RT [138, 139]. While other dielectric studies on both single and polycrystalline CCTO samples indicated a large low frequency relaxation due to surface layers which are sensitive to air atmosphere and type of electrode material used [19, 21].

To the best of our knowledge, no study could be seen in the reported literature regarding the exact reasons for observing such variations at low frequency at RT or finding a way to eliminate such variations. Moreover, no literature reported the electrical properties of CCTO measured in a moisture or air free test environment. In addition, the roles of measuring atmospheres and aging in it on the intra-grain and grain boundary (GB) dielectric properties are neither studied nor identified. A lack of such study may have led to reported data in the published literature that cannot be fully rationalized.

This literature survey and our own results have indicated as described in this chapter, that it is very important to eliminate or decrease the dependence of the dielectric properties of CCTO on ambient conditions such as humid air to eliminate environmental effects on measured dielectric properties for use as capacitors or other applications.

The value of tan δ (loss tangent) is also one of the important parameters determining a dielectric material's suitability for capacitor applications. However, to the best of our knowledge, any published data on dielectric properties and loss tangent of the CCTO ceramics measured systematically in a controlled environment could not find.

Therefore, the primary objective of the current study in this chapter is to investigate the effect of testing atmosphere on the stability and reproducibility of the electrical properties of CCTO. To accomplish this goal, the temperature dependence of impedance spectroscopy and dielectric properties of the CCTO samples are studied in both ambient air and in dry N_2. In addition, different sintering temperatures can provide different CCTO microstructures, densities, and defects, which can respond differently to ambient conditions as well.

Therefore, complex impedance of the CCTO ceramics with different microstructures produced by sintering at different temperatures are also investigated by measuring dielectric properties of identical samples in different atmospheres between 23°C to 225°C. Comparative dielectric properties measured in two different test environments of this study can be used as a guide for developing CCTO for possible capacitor applications. These results are analyzed, presented and discussed in this chapter.

The results of this work indicate that a large effective dielectric constant with a lowest loss tangent can be achieved as opposed to the value that can be observed for capacitors, which are used in normal ambient conditions if one can eliminate the changes of dielectric properties in CCTO capacitors caused by environmental conditions such as moisture and air.

6.2 Experimental Procedures

Pure CCTO powder was synthesized by solid-state reaction using stoichiometric ratio (1:3:4:12) of the high-purity $CaCO_3$ (VWR, 99.95%), CuO (VWR, 99.7%), and TiO_2 (Sigma-Aldrich, Anatase 99.8%) raw materials. CCTO powders calcined at 850°C for 6 h were uniaxially pressed at 165 MPa into 13 mm diameter and 2.3 mm thick pellets. Additional information on processing is stated in experimental procedure in Chapter 4 in this dissertation.

Four types of samples were prepared by sintering the pressed pellets at 1060°C (S1060), 1070°C (S1070), 1080°C (S1070), 1100°C (S1100), and 1115°C (S1115) with the holding time of 5 h in air at a constant heating and cooling rate of 2°C/min. Average particle size for all the calcined powders was measured as 250-500 nm using Malvern Zeta-sizer (see Chapter 5 of this dissertation for further details).

X-ray diffraction analysis (XRD, Bruker AXS D8 Discover) of the calcined powders and sintered samples was performed using a diffractometer with Cu Kα radiation. Optical micrographs were used to characterize the microstructure and grain size of the polished surface of the sintered samples.

Platinum electrodes were applied on as-sintered pellets and thermally cured at 600°C for 2 h to burn off the solvent/binder.

As explained in the experimental procedure in Chapter 4 in this dissertation, complex impedance ($Z^*=Z'-jZ''$) of as-prepared CCTO as a function of frequency from 1 Hz to 4 MHz of the applied ac voltage of 100 mV were measured at various temperature from 23°C to 225°C in air and dry N_2, respectively. Three measurements were made at various heating/cooling cycles between 23°C and 225°C while keeping the identical samples in both air and dry N_2 atmospheres, respectively. Before impedance measurements in N_2 atmosphere were carried out, all the samples were thermally treated by heating them up to 400°C in dry N_2 and then evacuating the chamber for 30 minutes to remove any water vapor/air and back-filled with N_2 at the same temperature.

During three temperature programmed heat/cool cycles, the samples were kept in N_2. At each heating cycle, the chamber was evacuated for 30 minutes at 225°C and back-filled with N_2 before cooling cycles were started. Complex impedance of the leads/instrument impedance was separately measured and was subtracted from the data before interpretation.

Table 6.1 show the description such as thickness, diameter, density, sample surface conditions, and testing atmosphere/temperature of the as-prepared CCTO (phase pure) prepared for measuring the complex electrical impedance.

Table 6.1. Description of the pure CCTO samples used for the analysis of electrical/dielectric properties.

Description	S1060	S1070	S1080	S1100	S1115
Diameter (mm)	11.20	11.22	11.34	11.40	11.32
Thickness (mm)	2.32	2.28	2.31	2.35	2.40
Density (g/cc)	4.667	4.728	4.579	4.522	4.566
% Relative Density	93	94	91	90	90
Sample surface Conditions	As prepared	As prepared	As prepared	As prepared	As prepared
Average grain size (µm)	4.95 ± 0.38	5.02 ± 0.17	4.57 ± 0.23	6.86 ± 0.15	7.94 ± 0.48
Largest grain size (µm)	20	20	20	27	25
Testing atmosphere	N_2 and Air	N_2 and Air	N_2 and Air	N_2 and Air	N_2 and Air
Testing temperatures	From 23°C to 225°C	From 23°C to 225°C	From 23°C to 225°C	From 23°C to 225°C	From 23°C to 225°C

6.3 Results

6.3.1 Complex Impedance Spectroscopy

Impedance spectra in Figure 6.1 and Figure 6.2 are for samples S1070 and S1100, respectively. It is noteworthy to mention that with the same electrode material, the total impedance measured at 23°C in air were considerably different and unstable. Figure 6.1 (a) and Figure 6.2 (a) clearly demonstrate that the impedance data are inconsistent at low frequency during prolonged exposure to air atmosphere at 23°C. As can be seen in Figure 6.1 (a) and Figure 6.3 (a), the impedance of two samples measured at various holding times in air at 23°C at low frequency are changing unpredictably when the same samples were repeatedly measured during various heat/cool cycles.

Impedance measured in dry N_2 for both samples are shown in Figure 6.1 (b) and Figure 6.2 (a). The total impedance observed at low frequency at 23°C in N_2 is larger and highly reproducible when compared with the impedance of the same sample measured in air

atmosphere. It is evident that low frequency impedance measured in air at 23°C is very sensitive to testing atmosphere. Furthermore, the high frequency data for both the samples measured at 23°C are shown in Figure 6.1 (c) and Figure 6.2 (b). The high frequency arcs are coincident with each other despite their testing atmosphere suggesting the negligible impedance change in the bulk of the CCTO in both atmospheres.

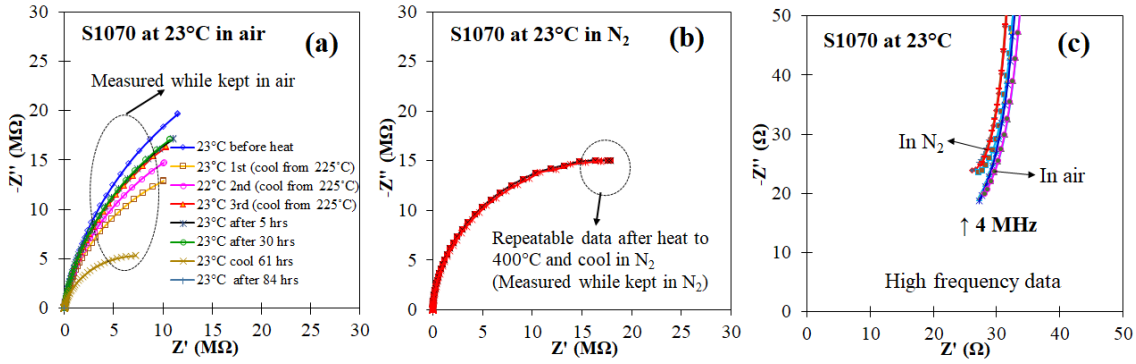

Figure 6.1. Impedance spectra of the same CCTO sample S1070 measured at 23°C in (a) air and (b) N_2 and (c) is the corresponding high frequency data.

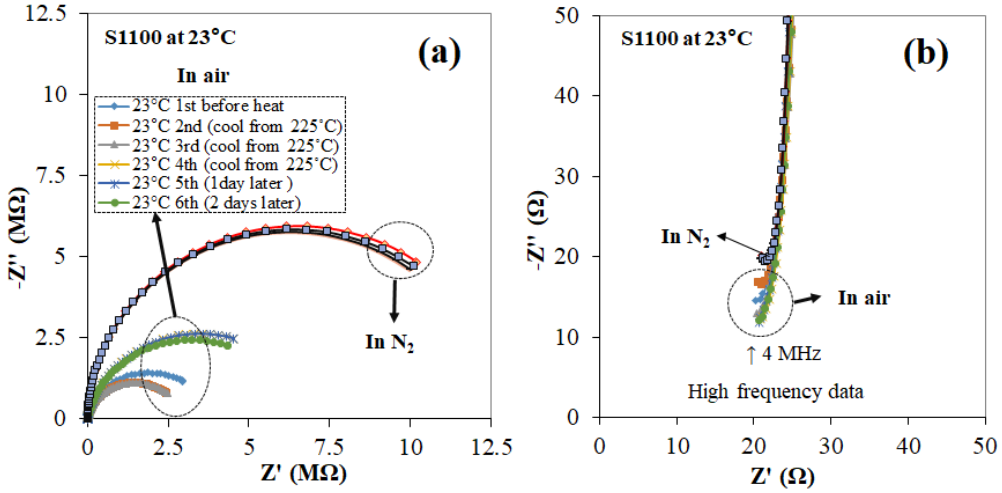

Figure 6.2. (a) Impedance spectra of the same CCTO sample S1100 measured at 23°C in air and N_2 and (b) is the corresponding high frequency data.

Figure 6.3 and Figure 6.4 show the impedance spectra measured at high temperatures (58°C, 89 °C, 114°C and, 171°C) for samples S1070 and S1100, respectively. Fully resolved semicircular arcs can be seen for both the samples at high temperatures. The different curves in Figure 6.3 and Figure 6.4 are from measurements done on identically the same samples repeatedly while heating and cooling cycles in air and N_2 atmospheres indicating high irreproducibility of data tested in air, especially for sample S1070.

As depicted in Figure 6.3 (a)-(d), the sample S1070 shows a large deviation of the total impedance when exposed to air at higher measuring temperatures compared with the same sample measured in dry N_2. However, as one can see in Figure 6.4 (a)-(d), the sample S1100 shows a smaller drift in the total impedance measured at high temperatures in both air and N_2 atmospheres because of its larger grain size.

Interestingly, the total impedance is relatively similar, when they are tested beyond 89°C despite the testing atmosphere. This indicates a less sensitivity to the measuring atmosphere when sample S1100 was tested at high temperatures (>89°C). The high frequency data for both the samples were close to each other at all the measuring temperatures irrespective of their testing atmosphere.

All the samples were stored at RT in vacuum oven after the treatments/measurements in dry N_2. To observe the stability of impedance of the N_2 treated samples, the complex impedance of the stored samples was re-measured in ambient conditions by leaving the same samples in air. Re-measured complex impedance of the same sample S1070 at 23°C (after treatment in N_2 and stored in vacuum oven at RT) is shown in Figure 6.5.

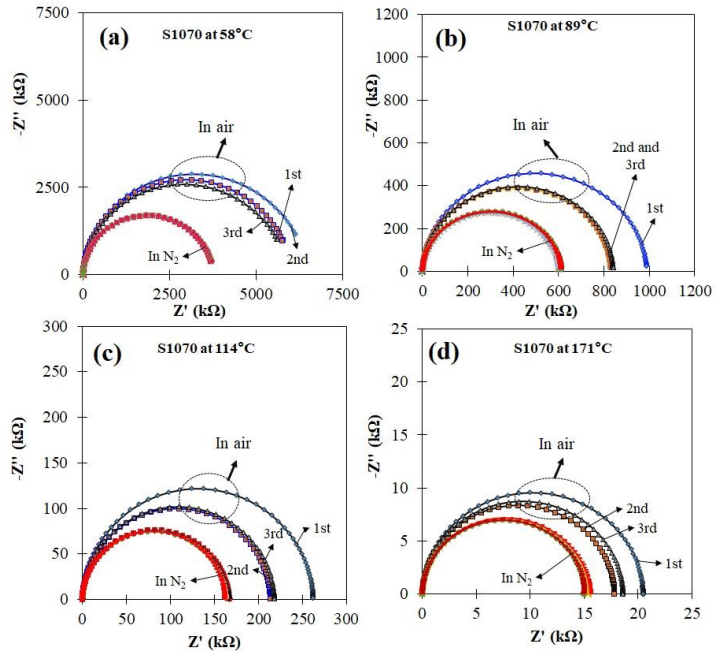

Figure 6.3. Complex impedance plots of the same CCTO sample S1100 measured at (a) 58°C, (b) 89°C, (c) 114°C, and (d) 171°C in both air and N_2.

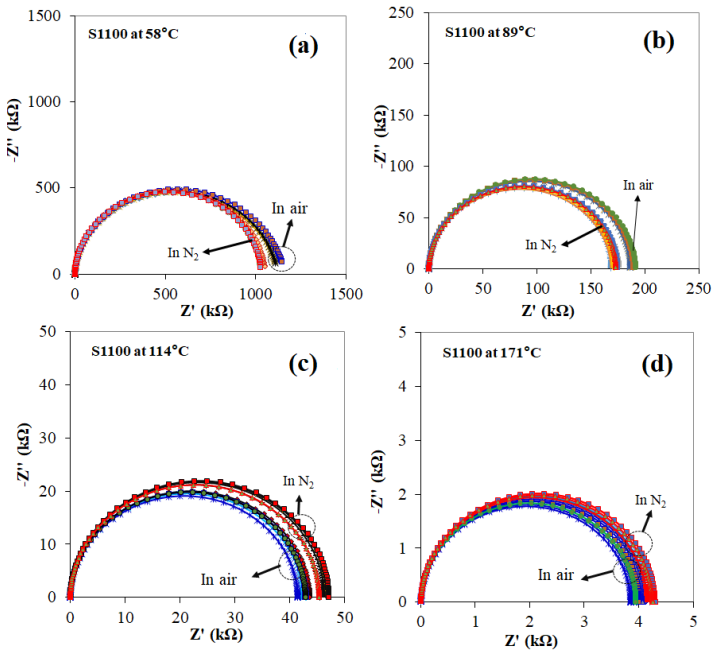

Figure 6.4. Frequency dispersion of the dielectric constant (ε′) of the same sample S1070 measured at temperatures (a) 23°C, (b) 58°C, and (c) 89°C in both air and N_2.

Various arcs in Figure 6.5 (a) are for repeatable measurements for the same S1070 sample in air atmosphere. A large variation in the impedance spectra at low frequencies confirm the unpredictable nature in air. However, re-measured high frequency data of the same S1070 are negligibly changed due to air atmosphere as shown in Figure 6.5 (b).

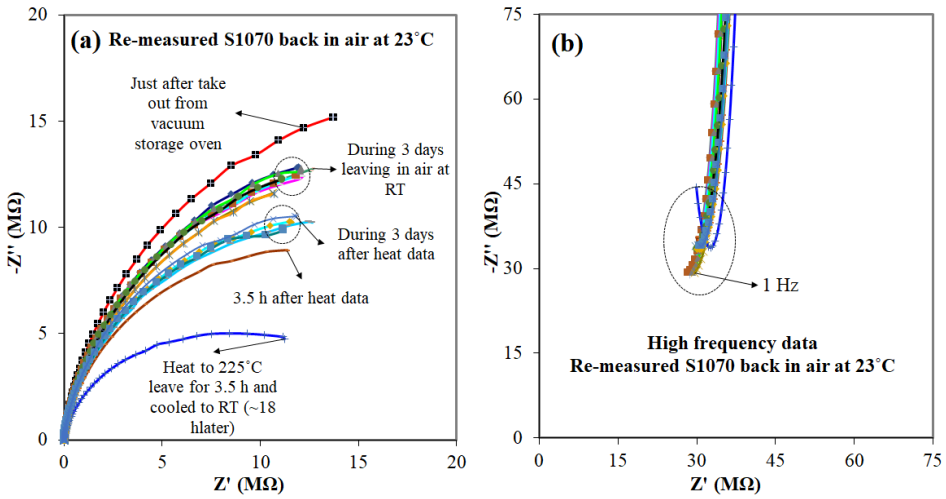

Figure 6.5. (a) Impedance spectra of the same CCTO sample S1070 re-measured in air at 23°C and (b) corresponding high frequency data.

Above observations further indicates that a stable low frequency impedance measured in dry N_2 seems to be associated with the elimination of mobile ion species due to moisture or air exposure on CCTO GBs, sample surface, on defects, etc. of all the samples.

To clearly see the values of real (Z') and imaginary (Z'') parts of the complex impedance as function of frequency and temperature measured in dry N_2, Z' and Z'', respectively of a chosen sample S1100 are shown in Figure 6.6 (a) and (b). Here, Z' and Z'', respectively represent the energy dissipation due to dc resistance and the energy storage of the sample. As shown in Figure 6.6 (a), Z' is decreasing as the temperature increasing. At low

frequency, the value of dc resistance (Z') is large and it is decreased upon increasing the frequency.

As can be seen Figure 6.6 (b), Z" is also decreasing abruptly when increasing the temperature at low frequency with no change of its value at high frequency. A dominant single peak value of the Z" (at which ωRC=1) represents the maximum of the Cole-Cole diagram. Peak values of Z" is shifted to high frequencies when increasing the measuring temperatures.

In the present work, similar frequency and temperature dependent Z' and Z" curves for all the samples could be observed (not shown here) despite the measuring atmosphere.

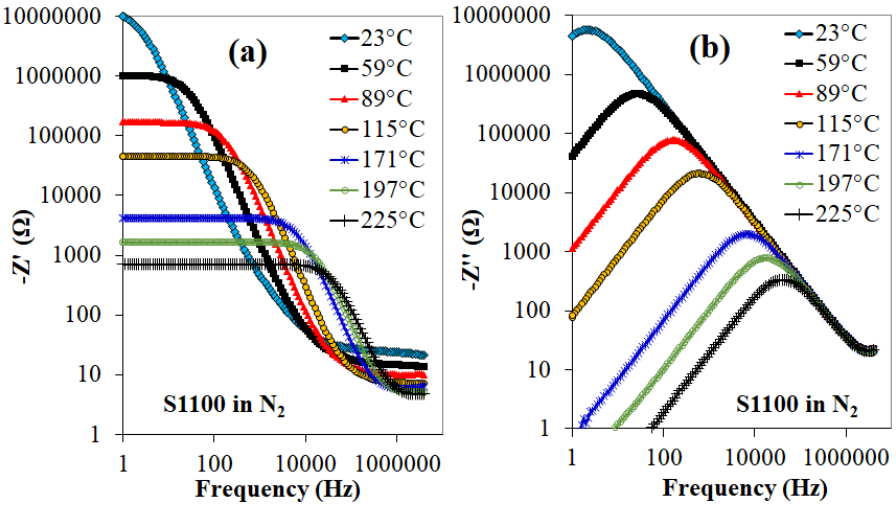

Figure 6.6. Frequency and temperature dependent of (a) real (Z') and (b) imaginary (Z") parts of the complex impedance of S1100.

In the current study, a single impedance semicircular arc was observed with no obvious electrode effect in both air and N_2 atmospheres throughout the measuring temperatures for all the samples when they were tested with the same platinum electrode.

Therefore, impedance data were analyzed using modified Cole–Cole function derived for two parallel RC circuits connected in series to account for the depressed semicircles for the grain and GB contributions of each sample [60].

In the present study, the impedance analysis was carried out using a Microsoft Excel Solver with the numerical least-squares minimization as explained in Chapter 4 of this dissertation. We minimized the root sum of squares of relative deviations between measured data and expected values.

The capacitances were determined by the maximum of each arc at which $\omega RC=1$, where, $\omega=2\pi f_{max}$ is the angular frequency and f_{max} is the peak frequency [60]. In the present work, the fitted values are obtained for samples S1070 and S1100 are shown in Table 6.2. Grain resistance, GB resistance, and GB capacitance are shown as Rg, Rgb and Cgb, respectively.

As can be seen in Table 6.2, the impedance measured at 23°C depicts a range of Rgb values in air atmosphere. However, this variation of Rgb is relatively negligible when both the samples are measured in N_2 atmosphere. Highly resistive barrier layers are indicated by much larger Rgb values in the sample S1070 compared with sample S1100. Additionally, the average Rgb values are comparable in both the atmospheres for the S1070. The sample S1100 shows higher Rgb at 23°C when measured in dry N_2 compared with the same sample measured in air atmosphere.

Still, both the samples show a large variability of Rgb values when measured in air. Conversely, at high measuring temperatures (>89°C), Rgb values are relatively

unaffected by the surrounding atmosphere for both the samples. Comparable Rg values indicates the stability of bulk (intra-grain) properties regardless of the testing atmospheres for both the samples. Therefore, GBs seem to play an important role in measured dielectric properties of sample tested in air.

Table 6.2. Fitted values of grain resistance (Rg), grain boundary resistance (Rgb), grain boundary capacitance (Cgb), and peak frequencies (f_{max}) measured in air and dry N_2 atmospheres at various ambient temperatures for samples S1070 and S1100.

Temp.	S1070 measured in air				S1070 in measuredN_2			
(°C)	Fmax (Hz)	Cgb (nF)	Rgb (Ω)	Rg (Ω)	Fmax (Hz)	Cgb (nF)	Rgb (Ω)	Rg (Ω)
23	1	6.9	(1.4-5.0)E+07	32	1	3.6	(3.1-3.2)E+07	31
58	6	4.5	(5.9-7.0)E+06	17	6	3.6	3.8.E+06	20
89	43	3.4	(1.0-1.3)E+06	14	43	3.5	(6.0-6.1)E+06	14
114	207	3.4	(2.1-2.6)E+05	10	207	3.5	(1.6-1.7)E+05	11
171	2374	3.5	(1.8-2.1)E+04	5	2374	3.9	1.5.E+04	6
197	7042	3.5	(6.3-6.5)E+03	5	7042	3.7	(6.4-6.5)E+03	5
225	18354	3.5	(2.4-2.6)E+03	4	18354	3.7	2.0.E+02	4
Temp.	S1100 measured in air				S1100 measured in N_2			
(°C)	Fmax (Hz)	Cgb (nF)	Rgb (Ω)	Rg (Ω)	Fmax (Hz)	Cgb (nF)	Rgb (Ω)	Rg (Ω)
23	3	16.8	(3.0-6.8)E+06	21	2	5.7	(1.2-1.3)E+07	22
58	25	5.5	(1.1-1.2)E+06	14	29	5.3	(1.0-1.1)E+06	14
89	159	5.3	1.9.E+05	10	177	5.2	(1.7-1.8)E+05	10
114	708	5.2	(4.2-4.4)E+04	7	658	5.2	(4.5-4.8)E+04	7
171	7443	5.4	(3.9-4.1)E+03	4	7070	5.3	(4.2-4.3)E+03	5
197	19818	5.4	1.5.E+03	4	18046	5.3	(1.6-1.7)E+03	4
225	48248	5.3	(5.8-6.6)E+02	4	424498	5.3	7.1.E+02	4

Total impedance has decreased significantly when the temperature is increased from 23°C to 225°C for both the samples despite the measuring atmospheres. Position of the maximum of the arcs is shifted to higher frequency when increasing the temperature from 23°C to 225°C regardless of the atmosphere. This shifting indicates the thermally activated electrical response for both the samples.

Interestingly, Cgb is relatively stable and temperature-independent in N_2 atmosphere at all the temperatures while it is stable in air atmosphere only beyond 89°C for both the samples suggesting the role of moisture/air on the GB capacitance.

Average grain size of the samples S1070 and S1100 determined as explained in the results in Chapter 5 was found to be 5 μm and 7 μm, respectively, indicating larger sized grains for sample S1100.

The frequency dependent dielectric properties were also studied on samples exposed to different atmosphere as described below.

6.3.2 Dielectric Properties

Dielectric constant (ε') was measured at various temperatures from 23°C to 225°C in air and dry N_2. Figure 6.7 and Figure 6.8 show the ε' measured at various temperatures (23°C, 58°C, and 89°C) as a function of frequency for the samples S1070 and S1100, respectively.

A frequency independent plateau region can be seen from 100 Hz to 1 MHz for both the samples in dry N_2. Irreproducible behaviors of ε' observed at frequencies from 1 Hz to below ~1 MHz in air atmosphere at low temperatures (23-58°C) are eliminated by changing the measuring atmosphere from air to N_2 for both the samples. However, ε' became relatively stable for both the samples by increasing the temperature to 89°C irrespective of the exposed atmospheres.

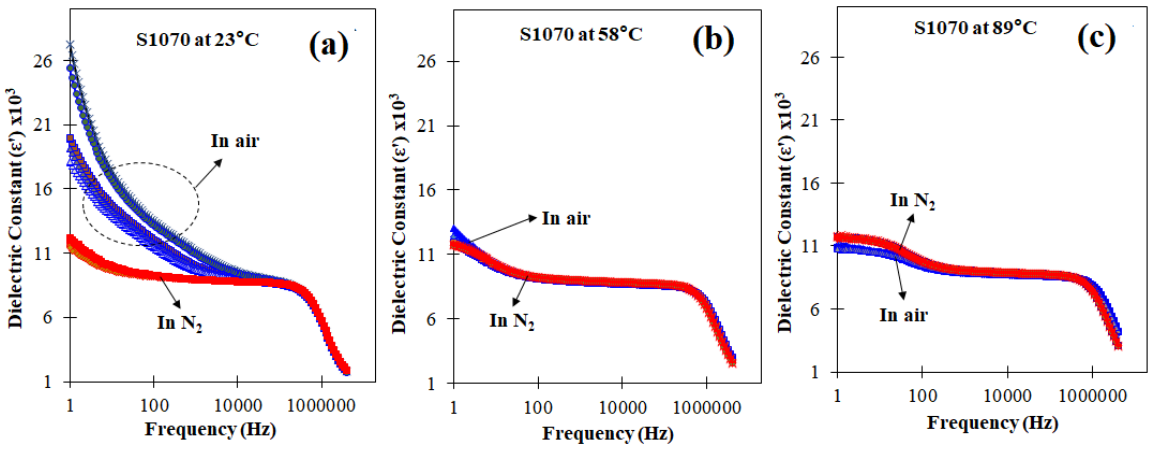

Figure 6.7. Frequency dispersion of the dielectric constant (ε′) of the same sample S1070 measured at temperatures (a) 23°C, (b) 58°C, and (c) 89°C in both air and N_2.

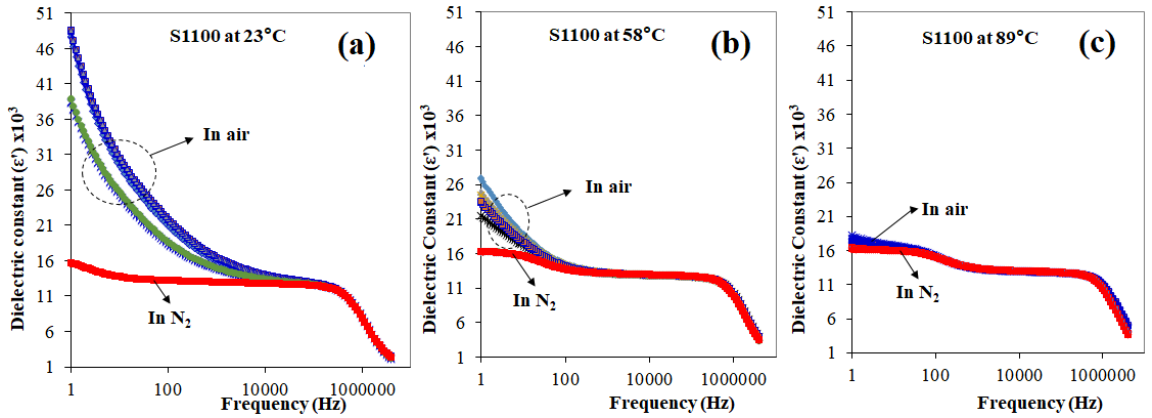

Figure 6.8. Frequency dispersion of the dielectric constant (ε′) of the same sample S1100 measured at temperatures (a) 23°C, (b) 58°C, and (c) 89°C in both air and N_2.

Figure 6.9 and Figure 6.10 show the loss factor, ε″ (imaginary part of the complex permittivity) of various samples that were measured at 23°C in both air and dry N_2 atmospheres as a function of frequency. As depicted by Figure 6.9 (a), S1070 shows a large discrepancy of the ε″ measured in air at frequencies <1MHz. However, this low frequency dispersion observed in air atmosphere has suppressed by changing the

measuring atmosphere from air to N_2. At very high frequencies, the loss factor is merged indicating stable high frequency dielectric loss despite the measuring atmosphere. Despite the measuring atmosphere a large increase of dielectric loss factor is indicated by the slope ε″ toward 1 Hz.

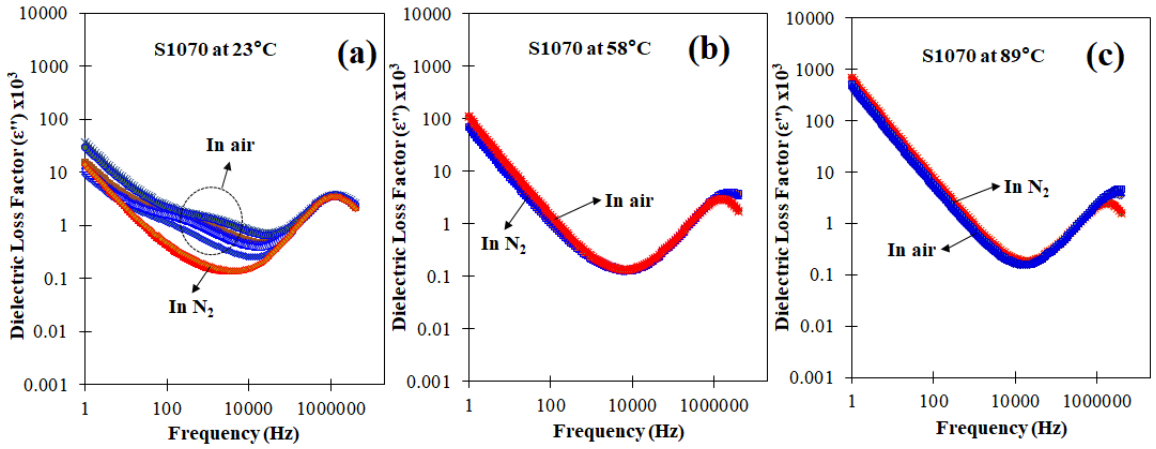

Figure 6.9. Frequency dispersion of the dielectric loss factor (ε″) of the same sample S1070 measured at temperatures (a) 23°C, (b) 58°C, and (c) 89°C in both air and N_2.

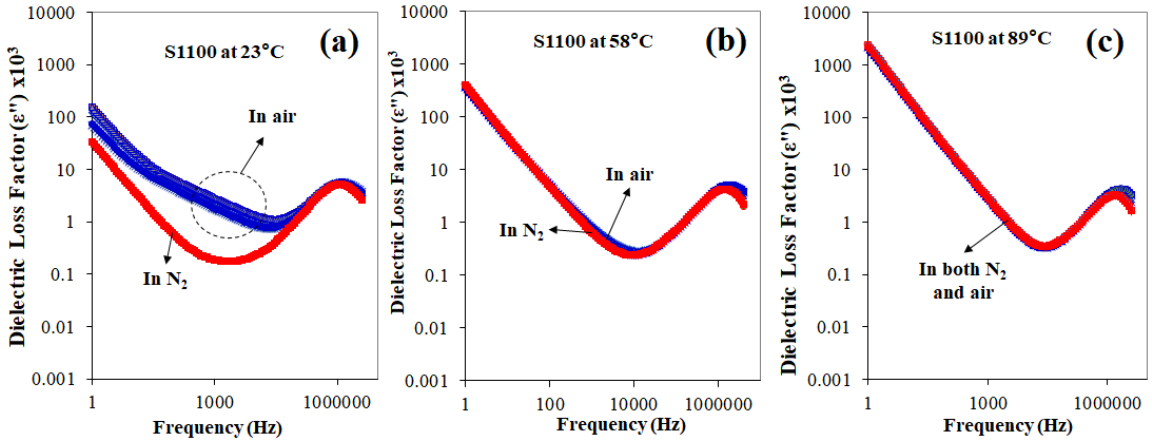

Figure 6.10. Frequency dispersion of the dielectric loss factor (ε″) of the same sample S1100 measured at temperatures (a) 23°C, (b) 58°C, and (c) 89°C in both air and N_2.

One can distinguish the dielectric relaxation steps by observing the shapes of the real part (ε') and the imaginary part (ε") of the complex dielectric function (ε*=ε'+ jε"), which are plotted as a function of frequency. Presence of high frequency loss peak in the current samples can be due to the relaxation of dipoles (mobile charge carriers that do not involve long range motion) which are related to the bulk properties [50, 140, 141]. Higher the frequency, molecular orientation time is reduced and hence polarization cannot follow the externally applied. This contribution is time-dependent i.e. frequency dependent and dependent on the type of material [50]. The low frequency relaxation is associated with the losses due to ohmic conductivity and/or relaxation of space charge polarization associated with transportation of charge carriers that are moving a longer distance [50].

Dipoles relaxational processes are identified by the peak of the imaginary part (ε") and step like decrease in the real part (ε') of the complex dielectric function (ε*=ε'+ jε") when increasing the frequency. In contrast, the conductive losses show an increase of imaginary part (ε") when decreasing the frequency as shown in Figure 6.11 (a). Pure ohmic conduction process as seen schematically in Figure 6.11 (a) at which the real part (ε') is frequency independent while imaginary part shows a negative slope [142]. The low frequency slope of the curve log ε″ vs. log ω is close to (-1) indicating the predominance of the dc conduction in this frequency region in Figure 6.11 (a). However, due to the presence of both conductive losses and space charge polarization at low frequencies, the slope of the imaginary part (ε") is greater than negative one (>-1) while real part (ε') show step like increase at low frequencies as indicated schematically in Figure 6.11 (b).

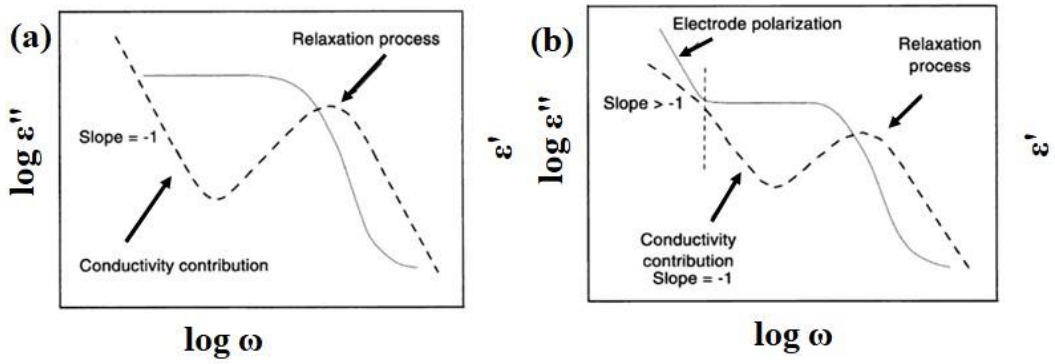

Figure 6.11. (a) Pure ohmic or (b) non ohmic conduction. Due to non ohmic conduction, GB or electrode polarization is observed [142].

To find the further evidence of relaxation of charge carries, frequency dependent ε' and ε'' of measured at various temperatures in N_2 were further studied. Figure 6.12 shows the ε' of a chosen sample S1100 measured at various temperatures in N_2 atmosphere. As can be seen in Figure 6.12, there are two reduction steps in the ε' accompanied by two plateau regions.

The first plateau at high frequencies can be attributed to defect induced polarization at grains. In all the investigated CCTO samples even at high temperatures, it is evident that there is a second charge-transport process that leads to a second plateau at low frequencies despite the measuring atmosphere. The second plateau is becoming wider and temperature independent when increasing the temperature. An increased value of the second plateau at low frequency is due to the space charge polarization at GBs. ε' related to the space charge polarization is slightly increased at high temperatures compared with the ε′ at 23°C as shown in the Figure 6.12 (a). Therefore, energy storage in the CCTO under study can be due to both dielectric polarization and charge accumulation.

As can be seen Figure 6.12 (a), the ε′ related to space charge effect (second plateau at low frequencies) is shifted to higher frequencies indicating the thermal activation of charge carriers. Increasing the temperature has increased the low frequency ε′ slightly while the first plateau at high frequencies (defect induced dipoles) remained unchanged.

In the current experiments, in the low frequency second plateau region, dielectric loss factor (ε") is increasing abruptly with increasing the temperature while high frequency relaxation peak is barely changed as seen in Figure 6.12 (b). Loss factor (ε") is orders of magnitude larger than the dielectric constant (ε') at low frequencies toward 1 Hz for both the samples. This indicates that the total dielectric loss is not only due to space charge relaxation, but also due to conductive losses. When increasing the frequency of the applied electric field, losses related to increased dipole relaxation losses because charge carriers cannot keep up with the applied field.

Presence of large increase of the dielectric loss factor in both S1070 and S1100 can therefore be attributed to the combined effect of conductive losses and space charge relaxation losses. Presence of large conductive losses in CCTO dielectric materials, which is placed between two platinum electrodes on the other hand indicates that there is a partial blocking of charge carriers at GBs and no barrier layer is formed at the sample–electrode interface to inhibit the migration of free charge carriers (i.e. it is a non-blocking electrode in the current experiments). Therefore, at lower frequencies, conductive losses are possible due to the non-blocking electrode and/or partial blocking of GBs. Upon increasing the frequency, contribution from charge carriers are low and hence low ε" is reached to a minimum value.

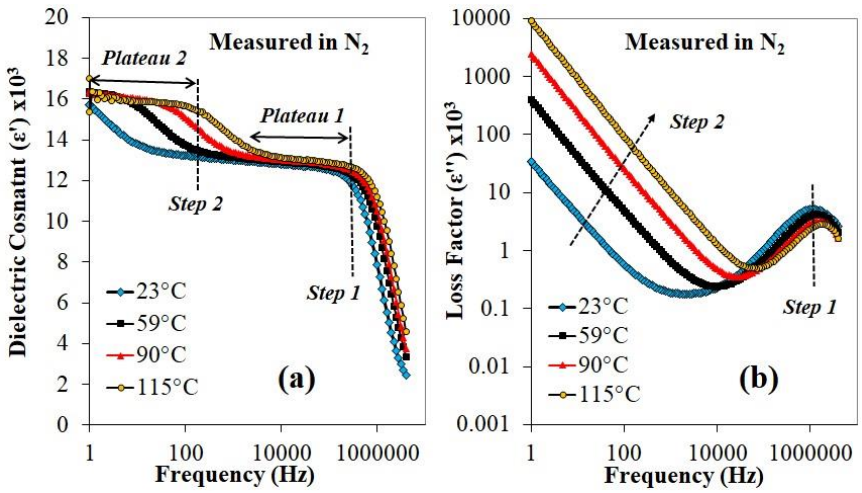

Figure 6.12. Frequency dispersion of the (a) dielectric constant (ε′) and (b) dielectric loss factor (ε") of the same S1100 measured from 23°C to 115°C in N_2.

Dielectric properties were further studied by analyzing tan δ, which indicates the ratio of the lossy to the lossless component (ratio ε"/ε′) in the application of AC electric field. Figure 6.13 (a)-(c) and Figure 6.14 (a)-(c) show the frequency dependence of tan δ of the two CCTO samples measured at 23°C, 58°C, and 89°C, respectively. The frequency dependence of tan δ exhibits a minimum at the frequency around which the dielectric constant shows a plateau region for both the samples.

In air atmosphere, tan δ observed at 23°C is much larger and inconsistent than that measured in N_2 for both the samples. Much smaller tan δ at 23°C in dry N_2 than in air implies that the conductive mobile charge carriers from air atmosphere has been eliminated. Hysteresis observed at 23°C due to surrounding ambient atmosphere has also been eliminated by increasing the temperature (58-89°C). As can be seen in Figure 6.13 and Figure 6.14, when both the samples are exposed to dry N_2 at low temperatures (23-58°C), tan δ values are less than 0.1 over a wide frequency range (100 Hz to 180 kHz)

were observed. However, dielectric loss is much smaller, ~0.01, over a narrow frequency range when the same samples were exposed to N_2 atmosphere at 23°C.

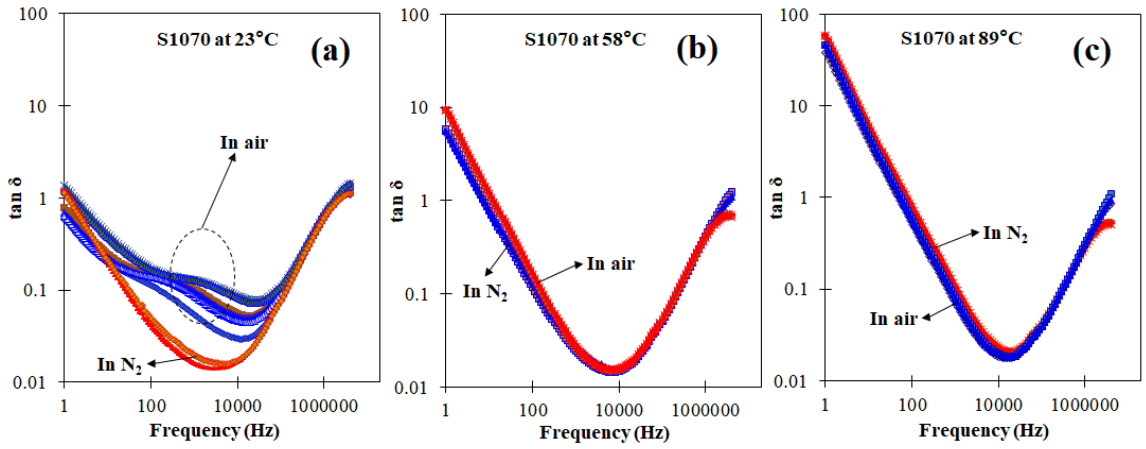

Figure 6.13. Frequency dispersion of the tan δ of the same sample S1070 measured at temperatures (a) 23°C, (b) 58°C, and (c) 89°C in both air and N_2.

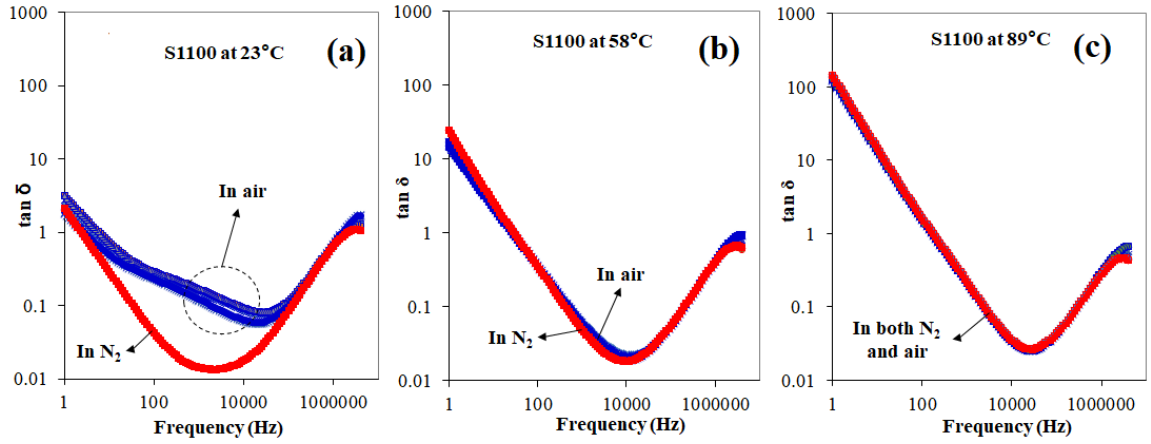

Figure 6.14. Frequency dispersion of the tan δ of the same sample S1100 measured at temperatures (a) 23°C, (b) 58°C, and (c) 89°C in both ambient air and N_2.

Table 6.4 shows that the dielectric loss related to the minima of both the samples is greatly reduced by switching the testing atmosphere from air to dry N_2 at 23°C despite

their sintering temperatures. Minima observed at 23°C has been shifted to lower frequencies when the measuring atmosphere is changed from air to N_2 for both the samples. Increasing the temperature from 23°C to 114°C, the minimum tan δ values are relatively unaffected by the atmosphere.

Table 6.4. Minimum values of dielectric loss measured in air and N_2 atmospheres for samples S1070 and S1100.

Temp. (°C)	tan δ (1070)		Dielectric constant (ε′)		Frequency (kHz)	
	Air	N_2	Air	N_2	Air	N_2
23	0.054 ± 0.016	0.015 ± 0.001	8,956 ± 216	8,841 ± 3	20	4
58	0.015 ± 0.001	0.015 ± 0.000	8,709 ± 10	8,868 ± 6	7.1	6.3
89	0.018 ± 0.000	0.020 ± 0.000	8,680 ± 14	8,856 ± 7	20	20
114	0.027 ± 0.001	0.028 ± 0.000	8,678 ± 13	8,856 ± 7	40	40
Temp. °C	**tan δ (S1100)**		**Dielectric constant (ε′)**		**Frequency (kHz)**	
	Air	N_2	Air	N_2	Air	N_2
23	0.069 ± 0.010	0.014 ± 0.000	13,245 ± 181	12,935 ± 2	25	2.2
58	0.021 ± 0.001	0.019 ± 0.000	12,891 ± 10	12,933 ± 7	13	10
89	0.025 ± 0.000	0.020 ± 0.000	12,888 ± 3	12,913 ± 7	28	14
114	0.039 ± 0.000	0.027 ± 0.000	12,884 ± 4	12,930 ± 6	71	28

Value of tan δ is increased when increasing the temperature from 23°C to 114°C in N_2 for both the samples while the opposite behavior is observed in air atmosphere. The sample S1100 shows the lowest tan δ at 23°C when exposed to dry N_2 at 23°C. Large-ε′ is retained with the minimum values of loss tangent when the same samples were measured at high temperature (114°C) despite the testing atmosphere. However, ε′ is much stable when CCTO are exposed to dry N_2 especially at low temperatures (23°C). A large ε′ even at high measuring temperatures indicates its temperature stability.

Table 6.5 shows comparison of the minima values of tan δ of all the samples (S1080, S1070, S1080, S1100, and S1115) tested in air and dry N_2 at 23°C in this research. As presented in Table 6.5, tan δ of all the samples are greatly reduced by switching the testing atmosphere from air to dry N_2 at 23°C despite their sintering temperatures. Samples S1070, S1080, and S1100 show very small minima values of tan δ at 23°C with a relatively large ε′ when exposed to both N_2 and air atmospheres at 23°C.

A relatively stable ε′ can be seen with a small standard deviation when all the samples were exposed to N_2 despite their sintering temperatures. As presented in Table 6.5, the ε′ related to the minima of tan δ of sample S1100 attains the highest value of all in both dry N_2 and air atmospheres. The sample S1080, which showed a relatively smaller relative density (91%) attains the lowest value of tan δ at 23°C in dry N_2.

Table 6.5. The lowest values of loss tangent and corresponding dielectric constants (ε′) observed for various samples S1060, S1070, S1080, S1100, and S1115 when exposed to air and N_2 atmospheres at 23°C.

Sample	Density	tan δ		Dielectric constant (ε′)		Frequency (kHz)	
		Air	N_2	Air	N_2	Air	N_2
S1060	93%	0.153 ± 0.033	0.052 ± 0.000	7,628 ± 159	7,090 ± 0	50	20
S1070	94%	0.054 ± 0.016	0.015 ± 0.001	8,956 ± 216	8,841 ± 3	20	4
S1080	91%	0.033 ± 0.006	0.010 ± 0.000	9,099 ± 243	9,664 ± 1	13	1.4
S1100	90%	0.069 ± 0.010	0.014 ± 0.000	13,245 ± 181	12,935 ± 2	25	2.2

Although S1060 has a large relative density (93%), it has the lowest ε′ and the highest tan δ values in both the atmospheres when compared with other samples. Therefore, CCTO sample S1060 was excluded from further analysis and investigations at high temperatures in this work. On the other hand, despite the relatively homogeneously distributed grains

and GBs among all samples (as explained in Chapter 5 of this dissertation), S1115 shows a relatively smaller minimum value of tan δ (0.026) than S1060 accompanied by much larger ε″ at 23°C.

6.3.3 Electrical Conductivity Measured in Dry N_2

As explained in the experimental procedure in Chapter 4, the DC conductivity, σ = t/(AR) of a ceramic sample, where, t is the sample thickness, A is the cross sectional area of electrode, and R is the real part of the impedance, can be expressed in terms of the reciprocal of the measuring temperature (1/T) by an Arrhenius relation [133],

$\sigma = \sigma_0 \exp(-E_a/k_B T)$ or R=t/(A σ)

Where, σ, σ_0, E_a, and k_B are the DC conductivity, the pre-exponential factor, the activation energy, and the Boltzmann constant, respectively.

A linear relationship between ln R (DC resistance) and 1000/T, was displayed for samples measured in dry N_2 as shown in Figure 6.15 (a) and (b) for the samples S1070 and S1100, respectively. The DC conduction activation energy of grain and GBs are shown as Eg and Egb, respectively.

Both the samples show relatively similar activation energies for both the grains and GBs irrespective of their sintering temperatures. Activation energies for intra-grain conduction of this study are closer to the typical reported values of 0.08 eV [9] and 0.084 eV [82]. GB activation energies are also comparable for the typical reported values 0.60 [9] and 0.678 eV [82] for CCTO.

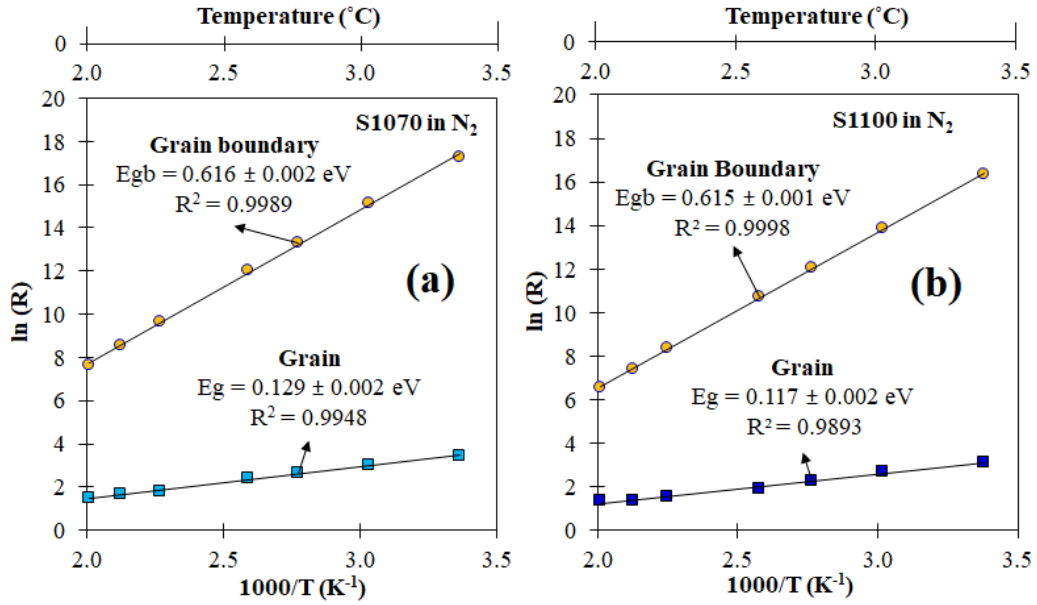

Figure 6.15. DC resistances of grain boundary and grain as a function of temperature measured in N_2 for (a) S1070 and (b) S1100.

It is preferable to plot the complex conductivity (ac conductivity, σ_{ac}) as commonly reported for high conducting material CCTO ceramics when dealing with its charge carrier system [143]. Complex conductivity is useful to find evidences for a second charge-transport process that leads to a second plateau in the frequency-dependent conductivity. Therefore, ac conductivity of all CCTO samples in this research were evaluated using the expression $\sigma_{ac}=\omega\varepsilon_0\varepsilon''$ [143].

AC conductivity of S1070 and S1100 are shown in Figure 6.16 exhibit the systematic change in ac conductivity with temperature at different frequencies. As seen in Figure 6.16, two different regions; a nearly-frequency independent ac conductivity region and then increase of the ac conductivity with frequency can be seen in both the samples. The ac-conductivity is very small at lower temperatures in comparison to that of high

temperatures for all the samples. A decrease of σ_{ac} (hence large resistance) toward 1 Hz indicate blocking of the charge carriers involved at low frequencies. Increasing the frequency, σ_{ac} increases indicating the mobility of charge carriers and merged at high frequencies indicating the bulk responsibility.

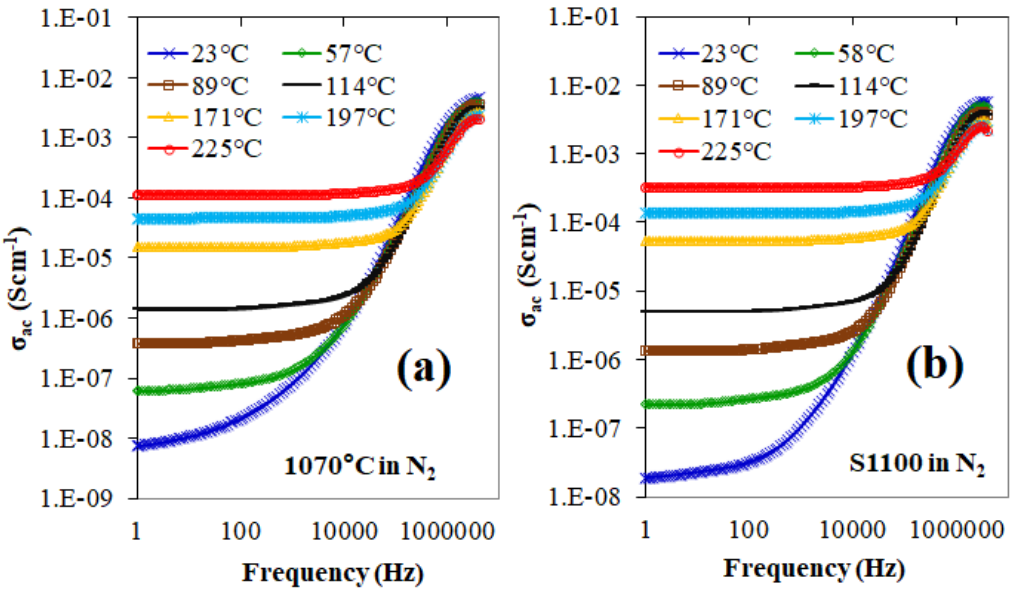

Figure 6.16. AC conductivity as a function of frequency for the as-prepared samples (a) S1070 and (b) S1100 measured in N_2 atmosphere at various temperatures.

6.4 Discussions

The impedance analysis over a wide frequency range showed consistent impedance spectra when measured in N_2 than in air atmosphere for both the samples. For the sample S1070, Rgb measured at 23°C in N_2 is within the range and comparable to Rgb measured in air. However, for S1100, Rgb value ($1.2x10^7$ Ω) is little higher in N_2 at 23°C than the same measured in air ($0.3\text{-}0.7x10^7$ Ω). Changes in bulk resistance (Rg) due to atmosphere

at 23°C are relatively negligible from our experiments. When increasing the measuring temperature, the total resistance of CCTO was decreased in both the atmospheres.

Authors [23] reported an unstable low frequency arc for CCTO ceramics. They argued that grains and GBs will not be sensitive to atmosphere when kept in air at RT. They [23] showed that only the impedance related to sample/Au- and In-Ga electrode-contact of some of the samples were sensitive to the surrounding atmosphere but not all the samples. They [23] observed a gradual increase of electrode contact resistance from the initial value of 7.7 kΩcm to 23 kΩcm and then to 75 kΩcm, respectively, after aging the samples in air for 4 h and then for 18 days at RT while no change were observed for the bulk. After annealing in air at 300°C, a large reduction in electrode resistance and capacitance were reported with no changes to GB or grain resistances [23]. Furthermore, in their study [23], modeling was carried out using three ideal RC circuits connected in series to account for the electrode contact, grain, and GB contributions. Authors [23] claimed that the electrode contact impedance can be sensitive to sample/electrode treatments and surrounding atmosphere if the Rgb of CCTO samples are considerably low. They also suggested that adsorption of oxygen at the sample electrode interface might play a role to alter sample electrode contact impedance. However, they did not measure the impedance at different testing atmosphere to verify the stability of the results. CCTO on the other hand is proven to be dominated by the resistance of the barrier layers formed at GBs [6, 7, 29] and less dependent on electrode contact resistance [24].

Our results appear to be similar to the work reported by authors [23] only in that air exposure makes the data more irreproducible possibly due to influence on the GB resistance, which is sensitive to surrounding atmosphere. It also suggests that the low frequency impedance cannot be attributed to surfaces (sample-electrode), which are sensitive to the ambient air and electrode materials used [19, 21].

In the current study, a single impedance semicircular arc was observed with no obvious electrode effect in both air and N_2 atmospheres throughout the measuring temperatures for both the samples with the same platinum electrode. Even with the same electrode material used with the same sample preparation conditions, both the samples showed an unstable low frequency arcs when exposed to ambient air atmospheres. The impedance data were modeled using modified Cole-Cole function to account for the depressed semicircles for the grain and GB contributions of each sample. We could not produce the repeatable impedance spectra at RT in air even by changing the electrode material from silver to platinum as reported elsewhere [144, 145].

The results of this study demonstrated that by heating the CCTO samples in N_2 at 400°C, one can eliminate the air, physically-absorbed moisture and associated surface ionic conductivity at the surfaces, GBs, and at pores to avoid unfavorable impedance hysteresis. Physically adsorbed moisture can change the low frequency impedance and dielectric constant of CCTO as reported earlier by another group [55, 56]. Therefore, the reason for repeatable impedance data for both the samples in N_2 of the present work could be due to the thermal cleaning of samples to get rid of both moisture and air prior to impedance measurements.

Impedance analysis clearly shows that the resistance of GBs (Rgb) for both the samples are much larger than that of the grains (Rg) at all the temperatures irrespective of the surrounding atmosphere, which is consistent with the reported trend for CCTO ceramics [25]. However, the deviation between impedance spectra measured in air and N_2 atmospheres is significant at room temperature than at higher temperature for both types of samples with different microstructures.

A much larger Rgb for both the samples can therefore dominate the electrical properties of CCTO. When an electric field is applied to such a system, migration of charge carriers can occur readily through the conducting grains, but it is hindered at the resistive boundaries leading to the charge accumulation at GBs. Increasing the temperature from 23°C to 225°C can enhance the mobility of charge carries to overcome the barrier at GBs leading to decreased Rgb. Much larger activation energy for GBs and much lower activation energy related to grains indicate more resistive nature of the GBs than the intra-grain.

Observed impedance changes in samples S1070 and S1100 can be directly related to their microstructures. The large number of fine grains in S1070 can increase the number of resistive GBs and hence can increase its overall resistance. On the other hand, a large average grain size and less number of resistive GBs in S1100 can lead to a lower overall Rgb. This is consistent with the behavior observed in CCTO ceramics by others [25]. Fitted impedance data (Table 6.2) showed highly conductive grains in both the samples, which indicates the presence of sufficient mobile charge carriers in the CCTO lattice [72].

It is known that preparation of perovskite CCTO sintered at high temperatures will easily introduce intrinsic oxygen vacancies defects V_O^+ and V_O^{++} into ceramic samples. These intrinsic defects have activation energies, which is 10-70 meV for V_O^+ and 100-200 meV for V_O^{++}, respectively [40, 75]. The activation energy of 0.62-0.63 eV for all the samples in the current work is within the probable ionization of V_O^{++} activation energy level. These observations clearly indicate that relaxation of CCTO GBs is related to point defects.

The possible charge carriers in CCTO ceramics are reported as point defects such as oxygen vacancies (V_o), partial charges of Ti^{3+}/Ti^{4+} and Cu^{1+}/Cu^{2+}, which are formed during sintering in air at high temperatures above 1000°C [73]. Positively charged V_o, Ti^{3+}, and Cu^{1+} are reported as acceptor centers and can introduce p-type charge carriers [51, 58]. The local fluctuation of these p-type carriers and electrons (n-type carriers) would increase the dipolar effect and contribute to the dielectric polarization [81, 82]. On the other hand, complex polar ordering of space charges and the hopping of electronic defects between them can give rise to space charge polarization at GBs and conductivity in CCTO as a result of energy minimization of the system [64].

When CCTO samples were exposed to air, ions such as H^+ and OH^- or some dissolved ions in the moisture can also increase the accumulation of charge carriers at GBs. Therefore, space charge polarizability at GBs can be varied depending on the concentration of defects in the CCTO structure [51, 58]. Accumulation of these charges at the highly resistive GBs can give rise to a large Cgb in the structure. Therefore, large

dielectric constant in air atmosphere can be attributed to the accumulation of more charges at the GBs.

On the other hand, the large sized conductive grains and/or thin insulating GBs in the sample S1100 than in S1070 can increase the Cgb of S1100. Studies indicated that effective static dielectric constant of CCTO is directly proportional to the Cgb at frequencies much lower than the dielectric relaxation frequency [24, 133]. While another study predicts that if the average grain size of the sample is increased, the volume fraction of GBs will decrease leading to a relation $\varepsilon_{eff} = \varepsilon_{gb}\varepsilon_0(D/t)$, where ε_{gb} is the relative permittivity of GBs, which was assumed to be same as the relative permittivity of grains and ε_0 is the permittivity of vacuum [24]. Also, *D* and *t* are the average grain size and average thickness of the GB region, respectively. This implies that if the ratio *D*/*t* is large, it can produce a larger Cgb. Although, a detailed study of arriving at above relation using barrier layer capacitor model is required, our results appear to be agreeing with reference [24].

Large sized conductive grains in S1100 than in S1070 can therefore be the reason for larger Cgb in S1100 than that of S1070. A relatively temperature independent Cgb in both the samples imply that the Cgb from GB does not change much with the temperature. Permittivity of lattice contribution to the static dielectric constant of CCTO is reported to be very small (~40-70) compared to that of the GBs [146]. Therefore, the apparent dielectric constant of the CCTO samples can be nearly equal to the permittivity of GBs [24]. Therefore, a much larger-ε' observed in S1100 than in S1070 can be attributed to the large Cgb in S1100.

In the present work, a large decrease in ε′ with frequency or the relaxation behavior is observed at very high frequencies. One must also note that the large-ε′ observed at low temperatures (23-58°C) and low frequencies in air atmosphere has been suppressed and weakened substantially when the same sample was exposed to N_2. However, the retention of a large-ε′ even at high measuring temperatures indicates the temperature stability of the ε′ of CCTO samples in both the atmospheres despite their sintering temperatures.

In our experiments, we did not see an increased dielectric loss due to N_2 atmosphere at low temperatures (23-58°C). However, increased mobile charge carriers due to humidity can increase the electrical conductivity leading to an increased tan δ values when both the samples were exposed to air atmosphere [64, 146]. Reduced tan δ, stable and large-ε′ in dry N_2 of the present study can therefore be attributed to the removal of air and mobile ions due to humidity that are enhancing conductivity at the GBs. Re-measuring the same samples in air after treating in dry N_2 showed unpredictable nature of the impedance at low temperatures. This behavior further indicates that adsorbed moisture and/or mobile ions in the air has a definite role in controlling the dielectric properties of CCTO.

It is reported earlier that even after evacuating the system at 500°C chemically absorbed moisture (OH^-) is difficult to eliminate completely [125, 126]. Therefore, in our experiments, a small increase of ε′ even in dry N_2 at frequencies less than 100 Hz could be attributed to polarization of chemisorbed moisture, which couldn't be eliminated completely. This suggests that chemically adsorbed moisture could still exist in CCTO samples of the present study. These observations show that ambient atmosphere has an important effect in controlling the dielectric properties of CCTO. These discussions also

suggest that consistent impedance spectra, dielectric constant, and tan δ seem to be associated with the removal of surface moist air.

On the other hand, the plateau at low frequencies is usually attributed to the space charge effect at GBs [9, 133] or electrode sample contact [139]. Since the large response time of the charge motion involved in the space charge accumulation is higher, they are typically observed at low frequencies. The polarization associated with the charge carriers that are accumulated on the GBs or electrodes is described by the ‘‘interfacial polarization or space charge polarization”, which is often seen in heterogeneous samples (such as conductive grains with resistive surface or GBs) [142].

If there is no barrier layer formed at the sample–electrode interface to inhibit the migration of free charge carriers, it is known as a non-blocking electrode. Interfacial or space charge polarization is also known as Maxwell-Wagner (MW) polarization [142]. MW polarization exhibits frequency dependent dielectric properties and hence the separation of charges at boundary layers can give rise to additional increase of the ε′.

Presence of high frequency relaxation can be attributed to dielectric polarization due to mobile charge carriers that do not involve long range motion [50, 131, 141]. While the low frequency relaxation is from the conductivity polarization associated with transportation of charge carriers over a long distance [50, 131, 141]. Two relaxations in the current experiments can therefore be explained as the following. Space charge relaxation at GBs and conductive relaxation at low frequencies probably due to the inhibiting charge carrier migration. As the frequency increase, an intrinsic relaxation concerning grains appears.

In the current experiments, we also see “non-blocking’’ electrodes, which might be resulted in negligibly small MW effects due to electrode polarization despite the measuring atmosphere or temperature is observed. Non-blocking electrodes on the other hand cannot produce a RC element and hence no spike or semicircle can be seen in the impedance spectra, which agrees with our impedance analysis. In the current experiments, the associated complex impedance and permittivity can be attributed to MW polarization at GBs, which is so large in air atmosphere than that of N_2 particularly at low frequencies. Fitted data in the current work showed a large capacitance for the samples exposed to air at 23°C implying a large accumulation of charges carriers at GBs.

Current experiments show that a large increase of dielectric loss (both ε" and tan δ) is seen even in dry N_2 atmosphere for all the samples at very low and at high frequencies. Therefore, the total dielectric loss in the current CCTO samples is the total energy loss due to dielectric relaxation process (space charge and dipole relaxation) and conductive losses [11].

6.5 Summary of Dielectric Properties of As-prepared Pure CCTO

Dielectric properties on various as-prepared CCTO samples at various temperature from 23°C to 225°C as a function of frequency shows that the nature of charge at interfaces (surface or GBs), their accumulation, and their contribution to polarization processes can be altered due to the surrounding atmosphere as we observed a large ε′ in air. Both the ε′ and ε″ exhibit high value in air atmosphere reflects the effect of large space charge polarization and conducting motion.

In the current research, the dispersion in ε″ is stronger than that in ε′ even in dry atmosphere implying combined effect of conductivity and space charge relaxation at low frequencies. Conduction (dc and ac) can be due to due to freely connected charge carriers and defects induced space charge and dipole relaxations. The value of ε″ at low frequencies becomes very high due to free charge motion within the material. Loss factor, ε″ is connected to ac conductivity relaxation at high frequencies.

Moisture related space charges in the air can prevent a good measurement reproducibility and accuracy as shown by the results in the current study. On the other hand, large effective ε′ can be associated with large sized grains. Therefore, we propose that the differences of real and imaginary parts of complex relative permittivity (ε*) in all the samples of the current study are caused by the differences in Rgb and C_{gb}, which is changing due to the differences in microstructure and accumulation of more charge carriers in the ambient.

CHAPTER VII

THICKNESS DEPENDENT ELECTRICAL PROPERTIES OF CCTO CERAMICS MEASURED IN AIR AND DRY N_2 ATMOSPHERES.

Contents published in: *Ceramics International* (Samarakoon et al., 2019)

Chapter Abstract: Phase pure $CaCu_3Ti_4O_{12}$ CCTO) ceramics are prepared by solid-state synthesis route. The effect of measuring atmospheres (air and dry N_2) on the stability and reproducibility of electrical properties of CCTO as a function of sample thickness (as-prepared to thinned down) is investigated. As-sintered CCTO prepared at 1080°C for 5 h with an initial thickness of 2.31-2.32 mm is reduced subsequently by fine grinding to 1.835 mm and then to 1.65-1.5 mm. Large inconsistency in the impedance spectra is observed when the samples are measured in air despite the thickness variations. Stable and reproducible dielectric properties are obtained in dry N_2. A relatively closer resistivity (~$2x10^8$ Ωcm at 23°C in N_2) regardless of the sample thickness suggests the absence of any barrier layer at the sample surface. Increased space charge accumulation at grain boundaries (GBs) leading to much larger dielectric constant (ε') was observed air at 23°C.

Increased space charge accumulation at grain boundaries (GBs) leading to much larger dielectric constant (ε') was observed air at 23°C. A temperature (from 23°C to 225°C) and frequency (from 1 Hz to 1 MHz) independent and stable ε′ is observed when samples are tested in N_2. Much lower tan δ values with large ε' are observed for both as prepared (0.010 ± 0.001 with ε′ of 9,663 ± 4 at 1.4 kHz) and the thinned down (0.015 ± 0.000 with ε′ of 9,352 ± 5 and 4.5 kHz) samples at 23°C in N_2.

7.1 Introduction

Studies report that dielectric constant (ε') in CCTO is due to Barrier Layer Capacitors (BLCs) that are formed via sintering CCTO in air [9]. Either a thin layer at the surface or grain boundaries (GBs) are re-oxidized to form an insulating layer at GBs and/or sample surface during sintering and subsequent cooling in air. Until now, various mutually exclusive hypotheses for explaining the origin of BLCs either by surface effect (electrode sample contact and surface barrier layer) or internal barrier layers (GBs and domain boundaries) have been suggested in the literature.

The origin of large ε′ in CCTO has been attributed to BLC effect originated by defects such as internal twining or domain boundaries [17, 147] in single crystals and GBs in polycrystals [8, 9]. Strong evidences from numerous studies suggest GBs as the most likely origin of the large internal BLCs in CCTO ceramics. Therefore, BLC effect in CCTO ceramics are attributed to space charge polarization at GBs giving rise to large effective ε′ [8, 15, 16]. Therefore, it has been established that an internal BLC structure of CCTO ceramics is due to conducting grains and insulating GBs.

In addition, a thin insulating layer at the sample surface or a surface barrier layer can also act as capacitors giving rise to effective ε′ in CCTO ceramics as reported by some studies. Two types of external barrier layers namely; surface barrier layer capacitor structure and sample electrode interface effects are schematically shown in Figure 7.1. Thin insulating layers (sample contact and surface barrier layers) can act as capacitors giving rise to effective ε′ in CCTO ceramics.

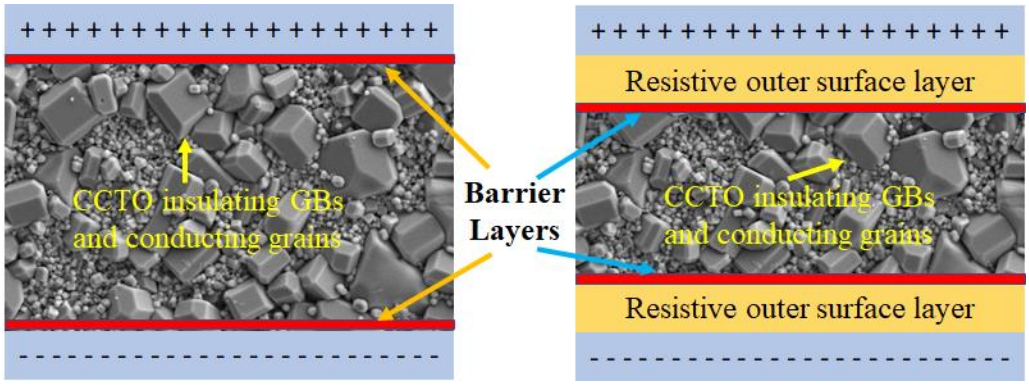

Figure 7.1. Schematic images for the effects of resistive barriers at the interfaces between sample-electrode and resistive outer surface-conductive inner core on the CCTO dielectric properties.

Therefore, surface barrier layers as well as sample electrode contact effect are also reported as possible sources that affect the overall dielectric properties in CCTO. As per some reports, space charge accumulation at the sample-electrode contact can create a blocking effect across which charge-transportation may become difficult [19, 21]. However, such propositions have turned out to be controversial as some reports [97] claimed that sample electrode contact effects are not playing a dominant role in controlling the dielectric properties of CCTO ceramics.

In contrast to the electrode effect, some studies indicated that CCTO surface barrier layers are formed due to the limited re-oxidation of sample interior compared with the sample surface during sintering of CCTO ceramics in air [20, 38]. The presence of gradient of the oxygen vacancies between the sample surface and the inner core due to inhomogeneous oxygen distribution during sintering is the suggested driving force for CCTO surface resistive layers [20].

On the other hand, CCTO ceramics and thin films are multifunctional due to its gas [123, 135, 136] and moisture sensitivity [55, 56], respectively. However, none of the above studies indicate whether the dielectric measurements were conducted in a controlled atmosphere. Therefore, dielectric response of CCTO is hard to explain clearly and still the reasons for large variations in its properties require further studies for providing new ways to reduce variability in measured properties and high values of tan δ.

In our recent studies [148, 149], we reported a strong influence of the ambient on the dielectric properties of as-prepared CCTO presumably due to the presence of moisture in air. A relatively stable and repeatable low temperature impedance data are obtained by switching the measuring atmosphere from air to dry N_2. We reported earlier [148, 149] and as indicated in Chapter 5 of this dissertation that a very low tan δ values at 23°C can be obtained by measuring the various as-prepared CCTO samples in dry N_2 than the same measured in air despite their sintering microstructure. No indication of electrode contact resistance were observed in the as-prepared samples in the current research despite the microstructural variations in the as-prepared samples. However, surface resistive barrier layer due to oxygen concentration gradient between as-prepared surface and sample

interior could still exist in the as-prepared samples and contribute to the measured dielectric properties.

If one uses CCTO for miniaturization of energy storage devices such as capacitors, then it is achieved by reducing the thickness of the dielectric layers in a capacitor. Therefore, investigations of the effects of testing atmosphere on the thickness dependent dielectric properties may not only be able to provide important clues about the underlying mechanism governing the intriguing dielectric behavior of CCTO, but also be useful for optimizing the sample preparation conditions for intended future applications.

However, no study is reported on the thickness dependent dielectric properties of CCTO samples measured in various testing environments or moisture/air free controlled atmospheres. Due to the discrepancy of the reported literature data even for materials prepared in a similar way, thickness dependent CCTO dielectric properties in various testing environments or in a controlled atmosphere is highly necessary for further study. Then one can correlate such data to already reported data and find out whether the new mechanisms of dielectric loss are related to surface layers. We have not seen any such study on a comparison of dielectric properties of as-sintered vs. thinned down samples, which were measured at various temperatures while exposing to moisture/air free atmospheres.

Therefore, the aim of this study is to investigate the effects of the sample thickness (such as as-prepared and thinned down) and testing atmospheres (air vs. dry N_2) on the dielectric properties of CCTO. The thickness dependent electrical properties of CCTO are measured by impedance spectroscopy of CCTO samples (as-prepared to thinned down)

using the same platinum electrode while testing the samples exposed to different heating and cooling cycles, and while exposing to air and dry N_2 between 23°C and 225°C. We observed a much larger ε′ at 23°C with large inconsistency in the impedance spectra when the samples were measured in air despite the thickness variations. These results are analyzed and presented in this chapter.

7.2 Sample Preparation for Complex Impedance Analysis

As explained in the experimental procedure in the Chapter 4 of this dissertation, phase pure CCTO powder was synthesized by solid-state reaction using $CaCO_3$ (VWR, 99.95%), CuO (VWR, 99.7%), and TiO_2 (Sigma-Aldrich, Anatase 99.8%). Calcined CCTO powders were mixed with 0.5 weight % PVB (polyvinyl butadiene) binder in ethanol and were uniaxially pressed at 165 MPa into 13 mm diameter and ~2.3 mm thick green pellets. De-binding of the pressed pellets was performed at 550°C for 2 h followed by pre-sintering at 950°C for 5 h. To study any effect of oxidized surface layers on the dielectric properties, sintering was done on green pellets S1 (2.31 mm) and S2 (2.32 mm) in air at 1080°C for 5 h at a constant heating and cooling rate of 2 °C/min.

As schematically shown in Figure 7.2, surface layers of as-sintered sample (S2) were removed from both sides by fine grinding the two parallel sides of the pellets from its initial value of 2.32 mm first to 1.84 mm and then to 1.5 mm. While as-sintered surfaces of sample (S1) were removed from initial values of 2.31 mm to 1.65 mm. Final thickness of the S1 (1.65 mm) and S2 (1.5 mm) were about 29% and 35%, respectively of their initial thicknesses (2.31 mm and 2.32 mm).

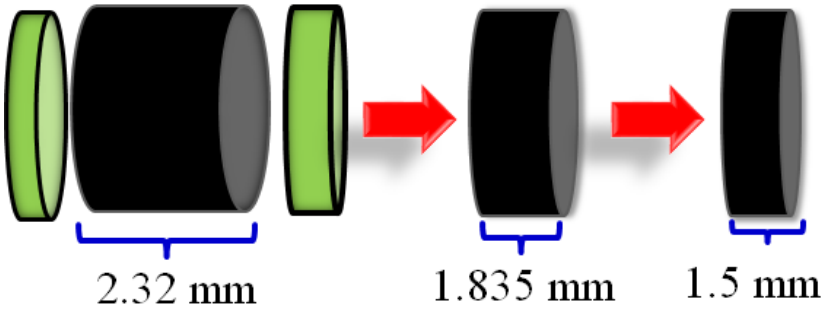

Figure 7.2. Schematic of thinning down steps of sample sintered at 1080°C for 5h.

Densities of the sintered pellets were determined using Archimedes method. Platinum electrodes were applied on the opposing surfaces of as-sintered pellets and were re-applied after thinning down (S1 and S2). Electrodes were cured at 600°C for 2 h. Impedance spectra of as-prepared sample S1 (2.31 mm) and thinned down sample S2 (2.32 mm, 1.84 mm, 1.5 mm, and 1.65 mm) first in air and then in dry N_2 were measured while heating and cooling between 23-225°C for a comparative study as explained in the experimental procedure in Chapter 4 and Chapter 6 of the current dissertation.

7.3 Results and Discussions

The average particle size of the calcined and sieved powders was measured as 500 nm [144, 145]. Similar particle size range (250-500 nm) was observed in SEM micrographs as well [144, 145]. As can be seen in Figure 7.3 (also shown also in Chapter 5), XRD of CCTO calcined powders (at 850°C for 6 h) and sintered ceramics (at 1080°C for 5 h) were fully indexed to be all CCTO related peaks with no observable secondary phases.

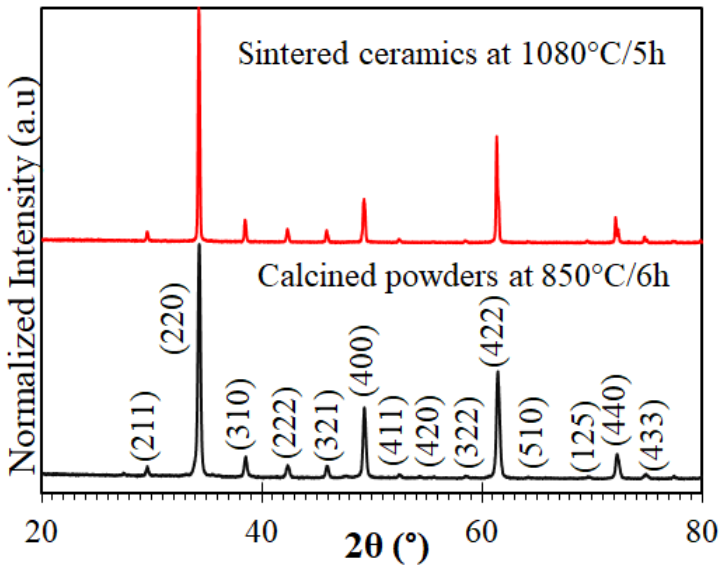

Figure 7.3. XRD of calcined CCTO powders at 850°C for 6 h and sintered ceramics prepared at 1080°C for 5 h.

Density of the sample sintered at 1080°C for 5 h is 4.579 ± 0.048 g/cm^3 (91%). SEM micrographs of the as-sintered ceramics, slightly polished surface, and thinned down to sample interiors are shown in Figures 7.4 (a), (b), and (c), respectively. All three images in Figure 7.4 within which islands of isolated small sized grains (1-2 µm) are present despite the thickness variations (as-prepared or thinned down). The polished sample shows some grain pull outs during polishing. The average grain size of the sample is ~5 µm (4.57 ± 0.23 µm).

Due to the differences in the oxygen vacancy concentration, limited re-oxidation of grain interior and oxidized GBs or surfaces are possible in CCTO resulting an inhomogeneous charge carrier concentration in the sample surface and grain interior [9]. Another study by authors [38] showed that surface layers originated by segregation of Cu-rich phase during

sintering can be removed upon thinning down of the outer surface layers of the pellet samples.

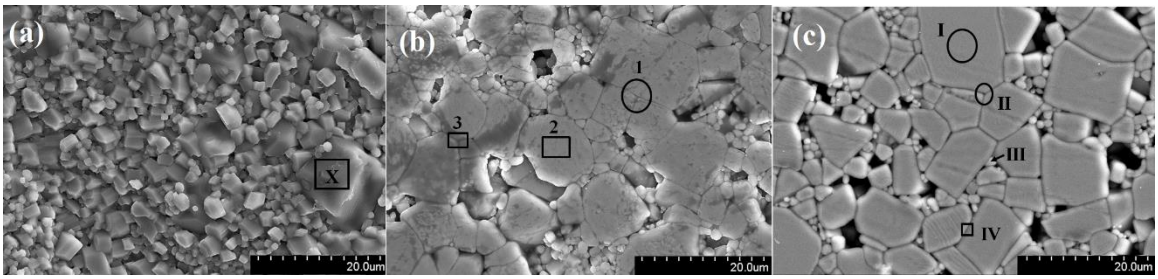

Figure 7.4. SEM micrographs of CCTO prepared at 1080°C for 5 h (a) as-sintered, (b) polished (closer to the as-sintered surface), and (c) thinned down into the interior of the sample (middle).

Therefore, we carried out EDS of each sample shown in Figure 7.4 to find out the compositional variations from sample surface to the interior.

Table 7.1 shows the distribution of all the elements from locations shown in Figures 7.4 (a), (b), and (c). EDS of as-prepared and slightly polished sample surfaces in Figure 7.4 (a) and (b) show stoichiometric ratio of Ca:Cu:Ti:O, which is 1:3:4:12 indicating no compositional variations in sample surface, intra-grain and inter-grain of as-prepared samples.

Typical inter-grain regions with two or three GBs in Figure 7.4 (c) indicated by locations II and IV and the intra-grain region (I) show slightly reduced oxygen concentration (1:3:4:10) but not significant.

Table 7.1. Distributions of all the elements of CCTO at different location points shown in Figure 7.4 (a), (b), and (c).

Element	X	1	2	3	I	II	III	IV
Ca	5.3	5	5.2	5.2	5.6	5.6	5.1	5.6
Cu	15.0	14.6	14.9	15.3	16.6	15.9	15.1	16.6
Ti	20.8	20.1	21.2	21.4	23.1	22.3	20.7	22.8
O	58.0	60.3	58.6	57.9	54.5	56.1	59.1	54.8

Figure 7.5 shows EDS elemental mapping of the same thinned sample (shown in Figure 7.4 (c)) showing a homogeneous distribution of all the elements even in CCTO sample core.

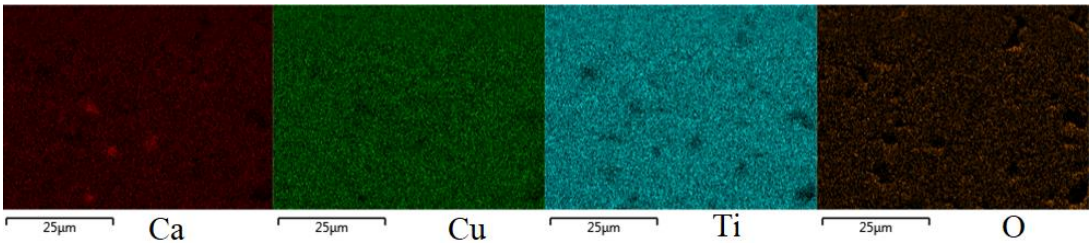

Figure 7.5. Element mapping of the thinned down sample shown in SEM image in Figure 7.4 (c) prepared at 1080°C for 5 h.

Cole-Cole plots of the CCTO as-prepared S1 (2.31 mm) and S2 (2.32 mm) as well as thinned down samples S1 (1.65 mm) and S2 (1.84 mm, and 1.5 mm) are measured at 23°C in air and N_2 atmospheres are shown in Figure 7.6 (a) and (b), respectively. Figure 7.6 (a) shows much closer impedance arcs when S1 and S2 were measured in air at 23°C. As we know bulk resistance of the CCTO pellets is related to its thickness (t), surface

area (A), and resistivity (ρ) by R=(tρ)/A. Therefore, the total resistance (R) observed at low frequencies in the complex impedance diagram should decreases as the sample thickness is reduced. However, when the thickness of S2 was reduced and tested in air at 23°C, thicker (1.84 mm) sample show a smaller arc compared with the thinner sample (1.5 mm). Moreover, thinner samples S1 (1.65 mm) has a larger arc than the thick sample S2 (1.84 mm) showing a large discrepancy when they were exposed to air atmosphere.

However, after switching the measuring atmosphere from air to dry N_2, thicker sample (1.84 mm) show a large arc than both the thinner samples (1.65 mm and 1.5 mm). As seen in Figure 7.6 (b), impedance arcs of thicker S1 and S2 are relatively closer due to small variations in their thickness 2.31 mm and 2.32 mm, respectively. Above observations indicate that in air atmosphere, impedance data are irreproducible despite the changes in the surface conditions (such as as-prepared or thinned down).

As reported by authors [55, 56], an increased impedance can be seen in the CCTO ceramics when the ionic conductive species related to physically adsorbed moisture is reduced. This is also the case when samples S1 and S2 were measured in dry N_2 in the current experiments. Relatively large arcs can be observed in N_2 atmosphere than in air atmosphere despite the thickness variations as can be seen in Figure 7.6 (b).

Interestingly, as can be seen in Figure 7.6 (c), no significant change in high frequency arcs is observed due to measuring atmosphere. At high frequencies, real part of the complex impedance (Z') is decreasing when the sample thickness is decreasing despite the measuring atmosphere, as expected. This indicates that only the low frequency impedance is sensitive to the measuring atmosphere despite the thickness changes. This

behavior is the same for the as-sintered samples of our previous studies published [148, 149] and as discussed in Chapter 6 of the current dissertation.

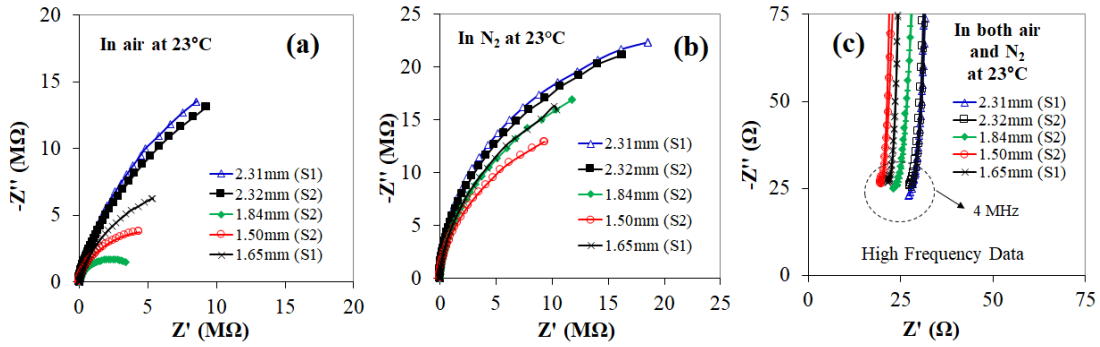

Figure 7.6. Impedance spectra of the same CCTO samples S1 and S2 measured at 23°C in (a) air, (b) N_2 and (c) is the corresponding high frequency data from (a) and (b).

Thin insulating CCTO surface barrier layers are formed during sintering CCTO in air at very high temperatures (>1000°C) [9]. In the current experiments, surface layers are removed by grinding and are therefore absent in the thinned down samples. Large impedance arcs of the thinned down samples in dry N_2 at 23°C compared to the same in air indicates that observed changes are not related to surface resistive layers of current samples. In this study before all the samples were introduced into the N_2 atmosphere, a thermal cleaning procedure was employed to remove the air and moisture by evacuation at 400°C and then exposed to dry N_2 atmosphere. Therefore, large arcs observed in dry N_2 can be attributed to removal of the air/moisture.

Since the impedance measurements are not stable in air atmosphere at 23°C despite the thickness, thickness dependent impedance spectra of S1 and S2 are further studied at high temperatures between 58°C and 225°C in dry N_2. Figure 7.7 (a), (b), and (c) show the

impedance spectra of S1 as-prepared (2.31 mm) and thinned down (1.65 mm) measured at 58°C, 89°C, and 114°C in N_2, respectively. As can be seen in Figures 7.7 (a) and (b), there is a variation of the total impedance between thin (1.65 mm) and thick (2.31 mm) CCTO samples at high temperatures (58-114°C). Thinner S1 shows a decreased total impedance compared to the thick S1 at high temperatures in N_2. Total impedance of both the samples are decreasing upon increasing the temperature from 58° to 114° as indicated by decreased diameter on the real axis (Z').

Some authors [23, 139] showed that as-prepared CCTO sample electrode contact impedance is sensitive to oxygen in air atmosphere and hence can affect the stability of the electrical properties when CCTO are aged in air (due to oxygen adsorption). They observed additional low frequency arc related to sample-electrode contact effect.

In the present experiments, no electrode and sample contact related impedance second arcs are seen even at high temperature (up to 225°C) either in the controlled N_2 or in air atmospheres despite the thickness variations. On the other hand, one strong overlapping peak is observed indicating the presence of dominant single relaxation response in both samples S1 and S2. As the temperature increases, the peaks of Cole-Cole plot shift to higher frequencies and gets lowered in intensity (Z" values). This indicates that electrical responses of both samples S1 and S2 are thermally activated. However, these variations are not related to sample and electrode contact effect, which is changing with the sample thicknesses.

Therefore, possible blocking layer at the sample/electrode interface is negligible in the current study. This fact implies that the samples studied contain many highly resistive

layers presumably at GBs. Therefore, impedance spectra with depressed semicircles were analyzed using an equivalent circuit consisting of two parallel RC circuits connected in series to represent the contribution from grains and GBs, respectively [60].

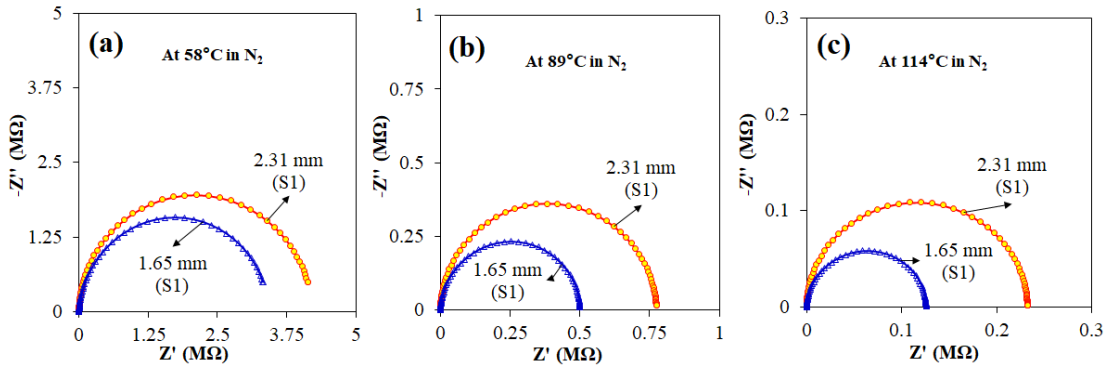

Figure 7.7. Complex impedance plots of the same CCTO samples S1 measured at (a) 58°C, (b) 89°C, and (c) 114°C in N_2.

DC resistance (R) values can be obtained from the intercept on the real axis (Z′), which is the diameter of each semi-circle. The capacitance (C) can be determined by the maximum of each arc at which $\omega\tau=1$ and $\tau=RC$ where, τ is the relaxation time and $\omega=2\pi f_{max}$ is the angular frequency and f_{max} is the peak frequency [60]. Fitted values of grain resistance (Rg), GB resistance (Rgb), GB capacitance (Cgb), peak frequencies (f_{max}), and resistivity of samples S1 and S2 (measured in N_2) are summarized in Table 7.2.

As shown in Table 7.2, the total impedance (Rgb plus Rg) of as-prepared sample (2.31 mm) is larger than that of thinned down sample (1.65 mm) at all temperatures. Total resistance is steadily decreased when increasing the measuring temperature for both the samples. Much larger Rgb>>Rg implies the presence of highly resistive GBs in both samples S1 (2.31 mm and 1.65 mm) that are dominating the overall resistance despite the

thickness variations of the CCTO. Upon reducing the thickness of as-prepared sample from 2.31 mm to 1.65 mm, Rgb measured at 23°C has decreased slightly from $4.2x10^7$ Ω to $3.6x10^7$ Ω.

Table 7.2. Fitted values of grain resistance (Rg), grain boundary resistance (Rgb), grain boundary capacitance (Cgb), and peak frequencies (f_{max}) of sample S1 as-prepared (2.31 mm) and thinned down (1.65 mm) and measured in dry N_2 at various ambient temperatures.

Temp.	2.31 mm (S1) in N_2					1.65 mm (S1) in N_2				
	f_{max}	Cgb	Rgb	Rg	Resistivity	f_{max}	Cgb	Rgb	Rg	Resistivity
(°C)	(Hz)	(nF)	(Ω)	(Ω)	(Ωcm)	(Hz)	(nF)	(Ω)	(Ω)	(Ωcm)
23	1	3.9	4.2.E+07	30	1.8.E+08	1	5.5	3.6.E+07	23	2.2.E+08
58	9	4.4	4.2.E+06	19	1.8.E+07	8	6.0	3.3.E+06	13	2.0.E+07
89	50	4.1	7.9.E+05	13	3.4.E+06	57	5.6	5.0.E+05	9	3.1.E+06
114	176	3.9	2.3.E+05	11	1.0.E+06	227	5.6	1.3.E+05	6	7.7.E+05
171	2090	4.1	1.9.E+04	6	8.2.E+04	2863	5.7	9.8.E+03	3	6.0.E+04
197	6842	4.0	5.8.E+03	5	2.5.E+04	8798	5.7	3.2.E+03	3	1.9.E+04
225	21109	3.9	1.9.E+03	4	8.4.E+03	23468	5.6	1.2.E+03	2	7.5.E+03

Some authors [28] suggested that current can detour across the material if the CCTO ceramics has a duplex microstructure. Application of electric field through such a microstructure can be restricted across the islands of small grains due to large number of resistive GBs resulting in varied electrical properties as a function of pellet thickness. Therefore, by reducing the thickness evenly from both sides of the as-prepared sample can change the number of serially connected active GBs between sample and the electrode. In such a case, Rgb, which is obtained from the low frequency arc of the impedance spectrum can be dependent on sample thickness.

Therefore, in the current samples as the thickness is decreased the number of oxidized GBs can be varied due to heterogeneous grain size distribution. Therefore, for the same GB thickness, upon thinning down the sample, a smaller number of highly resistive GBs can lead to slightly smaller Rgb in thinner S1 (1.65 mm) than the thicker sample.

Some authors [124] suggested that if the surface resistivity of CCTO is as high as $1.2x10^8$ Ωcm, then the mobile space charges may be absent on the surface at RT and hence electrode-contact related barrier layers are difficult to form despite the changes in the electrode materials. While others [20, 38] showed that surface barrier layers can be modified by changing the oxygen concentration by heat treatments in O_2 and N_2 at very high temperatures (800°C). They [20] reported that the as-prepared CCTO surface is less oxygen deficient and hence less conductive, while the inner core is more oxygen deficient and hence more conductive.

In the current samples, relatively closer and much larger resistivity values (~$2x10^8$ Ωcm) can be seen in both samples S1 (2.31 mm and 1.65 mm) despite the surface conditions (as-prepared or thinned down) when exposed to N_2 at 23°C. Even after removal of the surface layers, the similar resistivity of the as-prepared (outer) and thinned down (inner core) surfaces suggest that the observed changes are not related to either the surface BLC effect or sample-electrode contact effect.

Increasing the temperature has shifted the peak frequencies to higher frequencies implying the thermal activation of charge carriers. Time constant for GB relaxation (τgb), which is estimated from peak frequencies as τgb =RgbCgb has slightly increased from ~0.165 S to 0.197 S at 23°C, when reducing the thickness from 2.31 mm to 1.65 mm.

Increasing the measuring temperature has decreased the GB time constant ($\tau_{gb} = R_{gb}C_{gb}$) of both the samples due to reduction of R_{gb} by increased temperature.

C_{gb} of both samples remains practically unchanged as the measuring temperature is increased. However, C_{gb} has increased from ~4 nF to 6 nF as the sample thickness is decreased from 2.31 mm to 1.65 mm. This is because C_{gb} was estimated using $C_{gb} = \tau_{gb}/R_{gb}$, in which R_{gb} was smaller for the thinner sample. Therefore, C_{gb} is bit larger for the thin sample (1.65 mm) than the thick sample (2.31 mm). This assumption is consistent with the large R_{gb} in the thick samples of the current study.

The dc conductivity, $\sigma = t/(AR)$ of a ceramic sample where, t is the sample thickness and A is the cross-sectional area of the electrode, can be expressed in terms of the reciprocal of the measuring temperature (1/T) by an Arrhenius relation [133],

$$\sigma = \sigma_0 \exp(-E_a/k_B T)$$

Where, σ, σ_0, E_a, and k_B are the DC conductivity, the pre-exponential factor, the activation energy, and the Boltzmann constant, respectively. A linear relationship between ln (R) and 1000/T is displayed as shown in Figure 7.8 (a) and (b), respectively, for samples S1 with different thickness. The dc conduction activation energy of grain and GBs are shown as E_g and E_{gb}, respectively.

Both the samples show relatively comparable activation energies for grains, regardless of their thicknesses. Activation energies of intra-grain conduction of this study are also closer to the typical reported values of 0.08 eV [9] and 0.084 eV [82].

Changes in GB activation energies are slight for samples 2.31 mm (0.621 eV) and 1.65 mm (0.647 eV) and are comparable with the typical reported values 0.60 [9] and 0.678 eV [82] for CCTO. Large GB activation energy of both samples than the same of their grains indicates that the resistance of the GBs dominates the electrical properties of CCTO samples despite the thickness variations. Therefore, thickness reduction experiments of the current study do not show dramatic influence on dc resistance of grains and GBs.

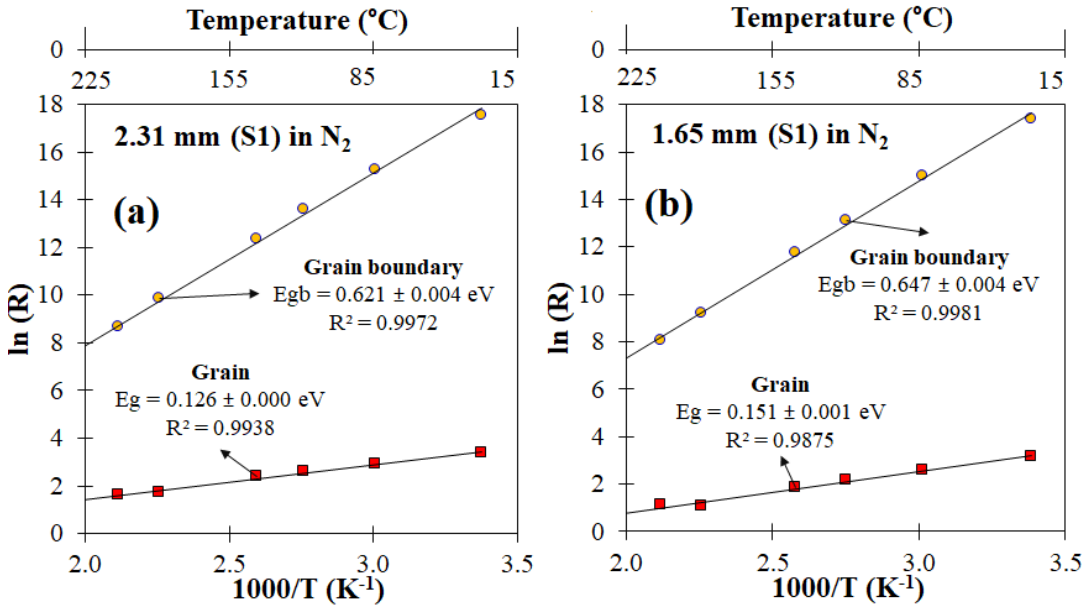

Figure 7.8. DC resistances of grain boundary and grain as a function of temperature measured in N_2 for S1 (a) as-prepared (2.31 mm) and (b) thinned down (1.65 mm).

The thickness dependent dielectric properties are further studied for samples S1 and S2. Figure 7.9 (a) and (b) show the thickness dependent ε′ (real part of complex relative permittivity, ε*=ε'+ jε") measured in air and N_2 atmospheres, respectively, at 23°C. As can be seen in Figure 7.9 (a), a strong dispersion with a large ε′ can be seen when the

samples were kept in air atmosphere at 23°C despite the variations in their thicknesses. In both the atmospheres, high frequency dielectric response does not vary significantly to alter the ε′ indicating the stability of charge carriers related to grains.

In contrast, Figure 7.9 (b) shows greatly suppressed and merged values of the ε′ into a plateau region with no noticeable influences of the sample thickness when switching the atmosphere from air to N_2. This behavior is attributed to a space charge effect from movable ions near the GBs from air/moisture (no electrode effect was seen by the impedance analysis). Therefore, large ε′ in air atmosphere can be attributed to large Cgb due to accumulation of more charge carriers at GBs in air. Notably, upon thermal cleaning in N_2, all the samples show reduction of accumulated charge carriers at GBs leading to decreased ε′.

A study [19] showed that the dielectric properties of CCTO are sensitive to the type of electrode contacts and sample thicknesses, and thus, large ε′ (below 1 MHz) was ascribed to the formation of the barriers between the electrodes and the CCTO sample. In their experiments, the observed changes in ε′ due to changes in electrode-type (using brass, Ag and Au) and the pellet thickness (polished for two different thicknesses 0.69 mm and 0.24 mm) were attributed to space charge effect at sample-electrode contact.

By contrast, in the present study, even for the same platinum electrode material there is an irreproducible dielectric property when measured in air atmosphere irrespective of the as-prepared or thinned down samples. On the other hand, ε′ data from samples S1 and S2 with the same platinum electrode show a relatively stable and much closer ε′ when exposed to N_2 atmosphere. The observation of no noticeable change to the ε′ for all the

samples measured in N_2 indicates that there is no surface barrier layer in the current samples. After switching the atmosphere from air to N_2, a frequency independent response over a wide frequency range is observed.

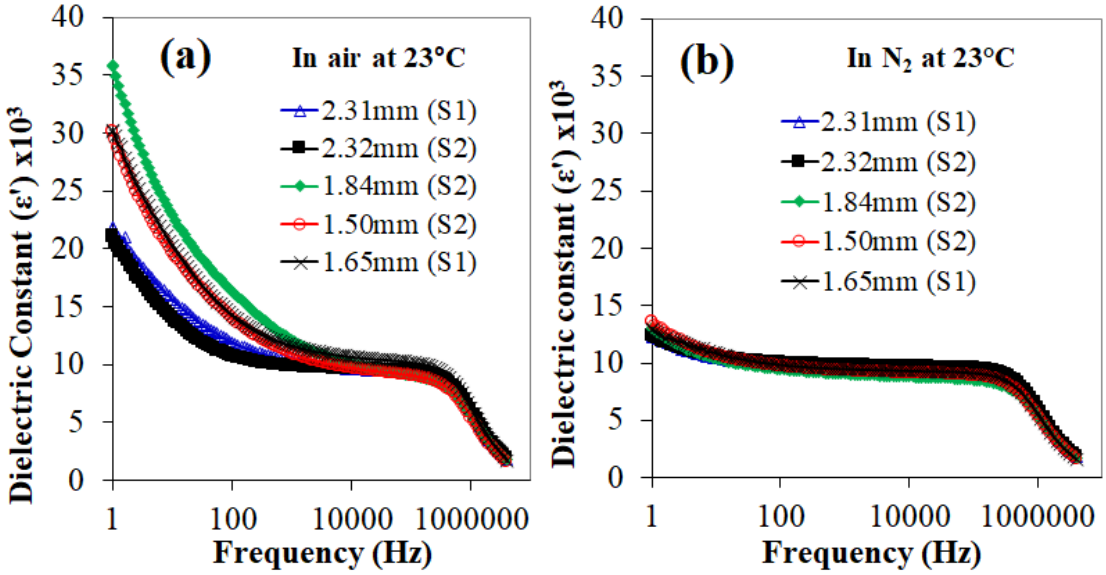

Figure 7.9. Frequency dispersion of the dielectric constant (ε′) of the same sample S1 and S2 of different thickness measured at 23°C in (b) air and (b) N_2 atmospheres.

We continued to measure the dielectric properties (ε′) in N_2 atmosphere at high temperatures as well. Figure 7.10 (a), (b), and (c) show the thickness dependence of ε′ for sample S1 measured at 58°C, 89°C and at 114°C. The sharp decrease of ε′ at high frequencies (>1 MHz) is most probably due to relaxation of dipoles related to grains. At higher frequency molecular orientation time is reduced and hence polarization cannot follow the externally applied field. The reported behavior of high frequency relaxations of CCTO ceramics is attributed to the relaxation of polar mixed valence cations Ti^{3+}/Ti^{4+} and Cu^{1+}/Cu^{2+} [73, 150, 151]. Upon increasing the temperature from 58°C to 114°C, no

noticeable shift of the high frequency relaxation for both the sample is observed (Figures 7.10 (b) and (c)).

On the other hand, complex polar ordering of space charges and the hopping of electronic defects between them can give rise to another step like increase of ε′ due to space charge polarization at GBs at low frequencies. Step like decrease at low frequencies is shifted to higher frequencies when increasing the measuring temperatures. A wide two plateaus (from 1 Hz to 1 MHz) indicates a relatively stable and consistent ε′ over a large range of frequencies when measured in N_2.

Thickness dependence of ε′ below 100 Hz is relatively small for both the samples when measured in N_2 from 58°C to 114°C while as-prepared sample S1 (2.31 mm) shows a slightly larger ε′ than that of thinned down sample (1.65 mm) at frequencies greater than 1000 Hz. However, these differences are insignificant.

Another study [38] reported the disappearance of large ε′ upon thinning down of the outer surface layers of CCTO, which were found to be Cu-rich. Segregation of Cu during sintering [38] and oxidation near the surface [94] can change the concentration of defects near the surface, GBs, and grain interior, which are contributing to the polarization and conductivity of CCTO [50]. Dielectric spectroscopic studies [19, 21, 69] on both single and polycrystalline CCTO samples indicated that a large low frequency relaxation is due to surface layer effect. Some studies reported the instability of CCTO surface/electrode barrier layers. Some authors [21, 69] observed a much stable low frequency ε′ when as-prepared sample was exposed to air compared to the thinned down sample measured in vacuum at RT.

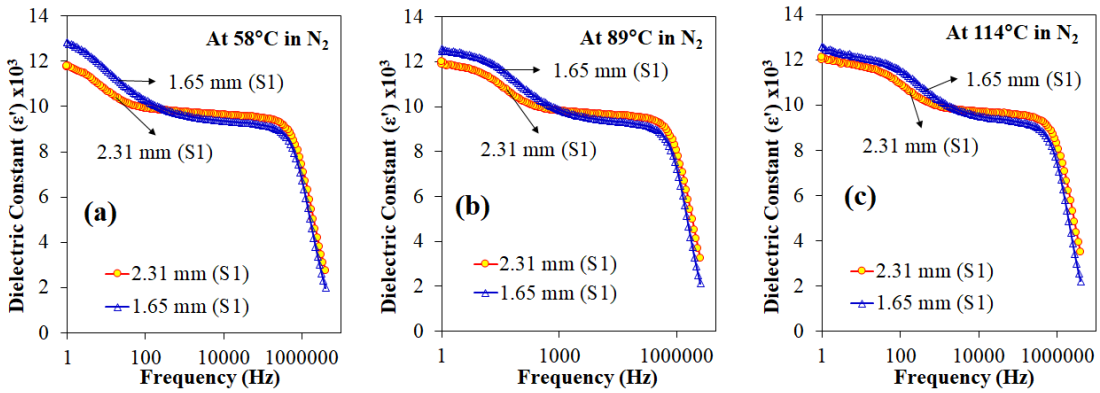

Figure 7.10. Frequency dispersion of the dielectric constant (ε′) of the same sample S1 with different thickness measured at (a) 58°C, (b) 89°C, and (c)114°C all in N_2 atmospheres.

On the contrary, in this study, elemental mapping by EDS revealed no Cu-rich GBs or surfaces. Large variation of ε′ was observed at low frequency region when the samples were exposed to air at 23°C despite the variation of the thicknesses even for the same electrode material used. On the other hand, the ε′ of the samples S1 and S2 with the same electrode show a relatively stable and much closer ε′ when exposed to N_2 atmosphere. This large low frequency variation disappeared when the measurements were performed in N_2 at the same temperature despite the thickness variations. This implies that the variations in impedance and ε′ of CCTO in the current study are not due to the sample thickness but due to the measuring atmosphere.

When changing the measuring atmosphere from air to N_2, the large dispersion of the dielectric loss factor, ε″ (imaginary part of complex relative permittivity ε*) is suppressed and became stable (not shown here) with no noticeable change due to thickness at 23°C. Therefore, the thickness dependence of ε″ is further investigated in N_2 at various

temperatures. Figure 7.11 (a), (b), and (c) show the thickness and frequency dependences of ε″ measured in N_2 at 23°C, 58°C and 89°C, respectively. A sharp increase of ε″ at low frequencies (toward 1 Hz) followed by a peak maximum around ~1 MHz with a minimum at ~ 10 kHz is seen for both the samples despite the measuring temperatures and thickness.

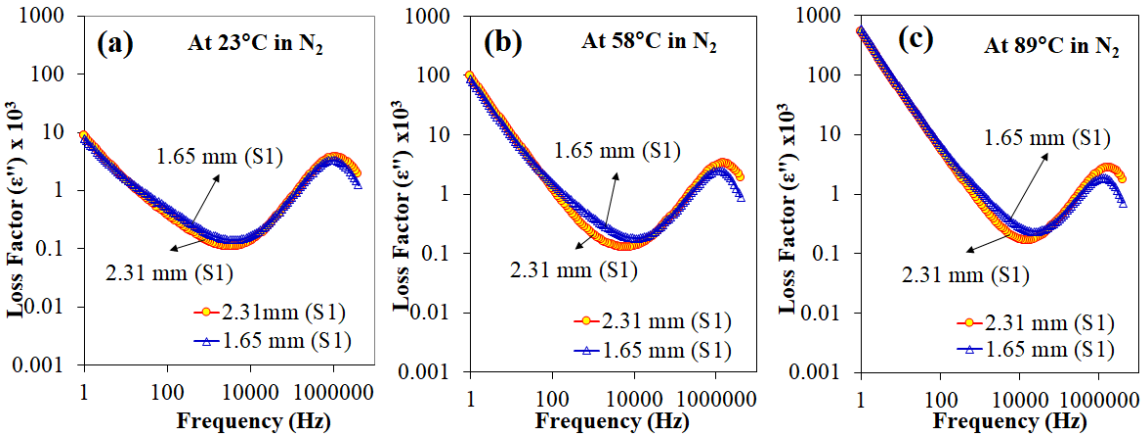

Figure 7.11. Frequency dispersion of loss factor (ε") of the same sample S1 and S2 measured at (a) 23°C, (b) 58°C, and (c) 89°C, respectively, in N_2 atmospheres.

Dipole relaxation process is identified by the peak of the imaginary part (ε") and step like decrease in the real part (ε') of the complex dielectric function when increasing the frequency. Therefore, the presence of high frequency loss peak (>1 MHz) can be attributed to relaxation of dipoles due to mobile charge carriers that do not involve long range motion that are related to the bulk CCTO [50, 152]. Ohmic conductivity losses are reported to be associated with transportation of free charge carriers over the longer distance [50]. The dc conductive losses show an increase of dielectric loss (ε") when decreasing the frequency. For pure ohmic conduction process, real part (ε') is frequency

independent while imaginary part (ε") show a negative slope [142]. However, due to the presence of both conductive losses and space charge polarization at low frequencies, the slope of the imaginary part (ε") is greater than negative one (>-1) while real part (ε') show step like increase at low frequencies.

Therefore, a slope of ε" (a sharp increase) toward low frequencies (1 Hz) in the current study indicates that dielectric losses in CCTO are related to dc conduction or space charge relaxation. At high temperatures (from 58°C to 89°C), orders of magnitude larger ε″ than ε′ toward 1 Hz indicates that the total dielectric loss is not only due to space charge relaxation, but also due to conductive losses. Therefore, large increase of ε″ at low frequencies can be due to combined effect of space charge relaxation at GBs and conduction losses.

At low frequencies toward 1 Hz, changes in ε″ are hardly observed despite the sample surface conditions in either as-prepared (2.31 mm) or thinned sample (1.65 mm). Therefore, space charge relaxation losses related to surface barrier layers are absent in the current samples. It appears that there is a partial blocking of charge carriers at GBs and no barrier layer is formed at the sample–electrode interface to inhibit the migration of free charge carriers (i.e. it is a non-blocking electrode in the current experiments).

Therefore, at lower frequencies, conductive losses are possible due to the non-blocking electrode and/or partial blocking by GBs. However, upon increasing the frequency, contribution from these charge carriers are small and therefore, a minimum value ε″ is seen for both samples (2.31 mm and 1.65 mm). At the moderate frequencies around ~10

kHz (between 100 Hz and 1 MHz), ε″ attains a minimum value at all the temperatures from 23°C to 89°C for both samples.

At the minima, as-prepared sample (2.31 mm) has lower ε″ values than the thinner sample (1.65 mm) whereas at high frequencies the contrary is observed. A slightly increased ε″ of the thinner sample at the minima point indicates lower number of the less resistive GBs in the inner core because of the slightly oxidized (less resistive) GBs for the thinned down sample. This can lead to large energy dissipation due to combined effect of the space charge relaxation at GBs and conduction. Conduction losses for both samples indicate the existence of non-blocking (i.e. ohmic) sample-electrode contact and partially blocking GBs.

Upon increasing the frequency of the applied electric field, ε″ is increased because the charge carriers cannot keep up with the applied field. When the frequency of the applied field is equal to the time required for charge carriers to orient themselves in the applied field leading to maximum dielectric losses as can be seen at peak maxima at high frequencies (peak at ~1 MHz).

Loss tangent, which is the ratio of ε″/ε′, was also measured in air and N_2 atmospheres for samples S1 and S2 at 23°C as a function of frequency. Loss tangent is greatly reduced by changing the measuring atmosphere from air to N_2 despite their thickness variations (not shown here). The position of the minima of tan δ is also shifted toward lower frequencies when changing the testing atmosphere from air to N_2. The behavior of the as-prepared sample and thinned down sample of the current study is same as our previous studies where changing the atmosphere from air to N_2 reduced the tan δ [148, 149].

Therefore, tan δ values measured at various temperatures in dry N_2 were further evaluated. Figures 7.12 (a), (b), and (c) show the frequency dependence of tan δ for sample S1 measured in N_2 at 23°C, 58°C and at 89°C, respectively. Relatively larger tan δ values are observed for both S1 samples (2.31 mm and 1.65 mm) at low frequencies (<100 Hz) and at high frequencies above (>1 MHz). However, at low frequencies (<100 Hz) both the samples do not show a significant change due to thickness variations. A very small change of tan δ at low (<100 Hz) frequencies indicates an almost identical increase in the real (ε') and imaginary (ε") parts of the ε* (ε*=ε'+ jε") in various thickness of sample S1.

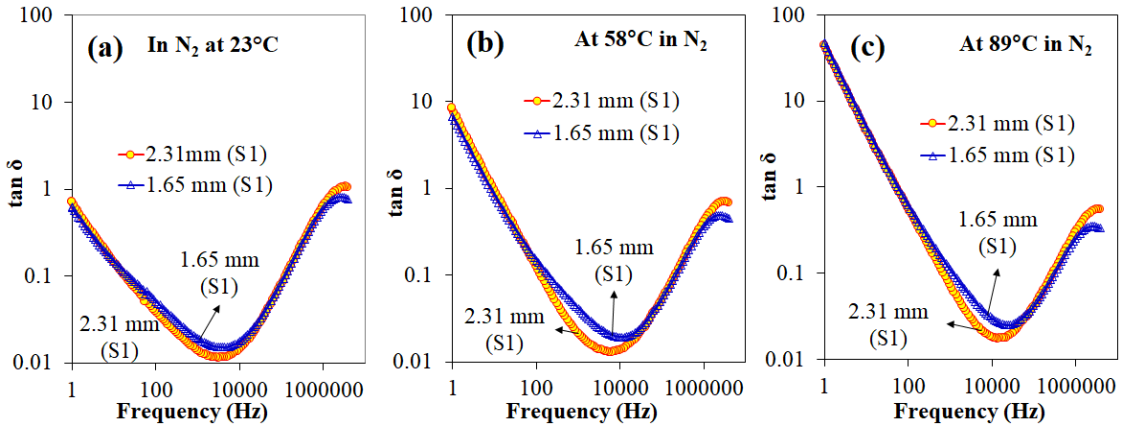

Figure 7.12. Frequency dispersion of tan δ of the same sample S1 measured at (a) 23°C, (b) 58°C, and (c) 89°C in N_2 atmosphere.

On the contrary when decreasing the as-prepared sample thickness, a slightly decreased tan δ is observed at high frequencies (>1 MHz). However, at high frequencies (>1 MHz) the dielectric loss peak position is unchanged despite the sample thickness. In both the samples, tan δ is varied through a minimum at moderate frequencies centered between 100 Hz and 1 MHz. A slightly increased minima tan δ value in thin S1 sample (1.65 mm)

can be attributed to a decreased contribution from the GB resistance (increased conductance) for thinner samples (less number of GBs).

Table 7.3 shows the lowest value of tan δ related to the minima measured in N_2 for samples S1 (2.31 mm and 1.65 mm). Corresponding frequencies, ε′, and ε″ related to the minima are also included for comparison. Frequency at which minimum tan δ is observed is shifted to higher frequencies with increasing temperatures from 23°C to 225°C despite the sample thickness. The minima tan δ values are increased very slightly from 0.010 to 0.015 when decreasing sample thickness from 2.31 mm to 1.65 mm at 23°C. Small changes to tan δ for both S1 can be related to slight changes in observed values of both ε′ and ε″.

If we assume that a barrier layer at GBs are contributing to the measured capacitance of both the samples, then the barrier layer at GB should not change with the thickness. As the apparent dielectric constant (ε) of the CCTO samples can be nearly equal to the permittivity of GBs, which lead to the relation, $\varepsilon \approx C_{gb}/C_0$ [133]. Here, Co is the capacitance of the vacuum. Increasing the sample thickness can increase the ε′ as reported for other CCTO ceramics [19] and thin films [153]. Other authors [36, 38] observed variations in ε′ due to thickness in the CCTO samples, which contain regions of fine-grains and extremely large grains, where Rgb>>Rg. Therefore, reducing the thickness from surface might lead to less number of more resistive GBs in duplex nature of CCTO as reported earlier [94] leading to lower overall GB resistance contribution to overall impedance. In the current study, although thinner sample (1.65 mm) has larger Cgb (~6 nF) than that of thick (2.31 mm) sample (~4 nF), apparent ε′ of thinner sample is

slightly smaller than that of thicker sample as can be seen in Table 3. This observation can be explained by roughly assuming the same BLC at GBs contributing to the measured complex impedance (Z*) across the sample thickness. A reduction in the number of more resistive GBs would also decrease the GB resistance slightly leading to slight increase of the measured value of Cgb (as Cgb = τgb/Rgb) in the thinned down sample (1.65 mm) as shown earlier by the impedance analysis. However, the reduction of number of highly resistive GBs and reduced overall dipole density (less number of charge carriers) can lead to a slight reduction of the apparent ε′ in the thinner sample compared with the same of the thick sample.

Table 7.3. Minimum values of tan δ and its corresponding ε′, ε", and frequencies measured in N_2 atmosphere for as prepared S1 (2.31 mm) and thinned down S1(1.65 mm) samples.

Temp. (˚C)	2.31 mm (S1) in N_2				1.65 mm (S1) in N_2			
	tan δ	ε'	ε''	Frequency (kHz)	tan δ	ε'	ε''	Frequency (kHz)
23	0.010 ± 0.001	9663 ± 4	101 ± 5	1.4	0.015 ± 0.000	9352 ± 5	143 ± 1	4.5
58	0.013 ± 0.000	9646 ± 6	125 ± 1	6	0.019 ± 0.000	9342 ± 6	180 ± 1	11
89	0.017 ± 0.000	9636 ± 0	166 ± 1	14	0.025 ± 0.000	9342 ± 8	234 ± 2	25
114	0.023 ± 0.000	9633 ± 3	220 ± 1	28	0.033 ± 0.000	9369 ± 7	310 ± 2	40
171	0.047 ± 0.000	9605 ± 2	454 ± 3	127	0.059 ± 0.000	9253 ± 6	544 ± 6	200
197	0.077 ± 0.001	9561 ± 1	733 ± 7	252	0.089 ± 0.001	9086 ± 7	809 ± 15	357
225	0.118 ± 0.001	9407 ± 4	1110 ± 9	504	0.120 ± 0.002	8628 ± 12	1034 ± 13	634

AC conductivity ($\sigma_{ac}=\omega\varepsilon_0\varepsilon''$) of samples are shown in Figure 7.13 (a) and (b) for as-prepared and thinned down samples 2.31 mm and 1.65 mm, respectively, in N_2 atmosphere. A very large resistive behavior, which is dominated by a relatively frequency independent ac conductivity is seen for both the samples at lower frequencies. At high

temperatures, σ_{ac} is increased rapidly and at 225°C, it is about 10^{-4} Scm^{-1} (or resistivity, $\rho \approx 10^{4}$ Scm^{-1}). Whereas at frequencies below 100 Hz at 23°C, σ_{ac} is $<10^{-8}$ Scm^{-1}. Upon increasing the frequency, σ_{ac} is also increased and showed a dispersion for both the samples. Both samples show similar response with frequency and temperature. These observations further confirm that there is no surface layer effect based on the data on samples with thickness variations when measured in N_2.

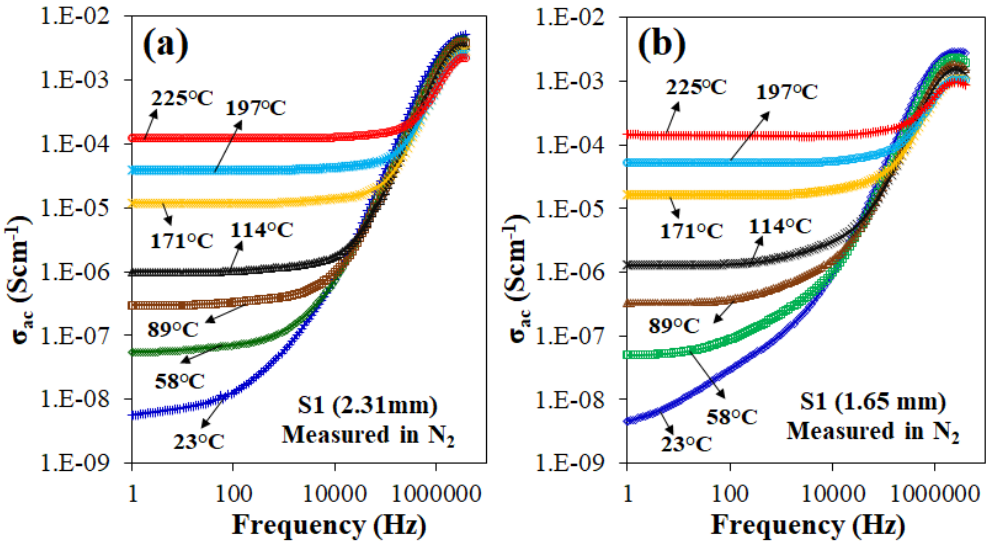

Figure 7.13. Frequency dispersion of the AC conductivity (σ_{ac}) of the same sample S1 (a) as-prepared (2.31 mm) and (b) thinned down (1.65 mm) measured at various temperatures in N_2.

Results in this chapter tend to prove that the large discrepancy and variations of dielectric properties reported in the literature for thickness related experiments in CCTO materials cannot be solely due to its sensitivity to processing, sintering conditions, and annealing conditions but also probably due to its large sensitivity to testing atmosphere.

CHAPTER VIII

INFLUENCE OF ALUMINA DOPANT AND ENVIRONMENT ON THE ELECTRICAL PROPERTIES OF CALCIUM COPPER TITANATE CERAMICS

Chapter Abstract: Calcium copper titanate ($CaCu_3Ti_4O_{12}$; CCTO) ceramics are useful as capacitor dielectrics for many applications. In this study the effect of doping with alumina and testing atmospheres in air and dry N2 on the stability and reproducibility of electrical and dielectric properties of CCTO-xAl_2O_3 system, where x=0, 0.5, and 4wt.% as a function of temperature are investigated. Solid-state synthesis route is used to fabricate the pure and doped CCTO samples sintered at 1080°C and 1100°C for 5 h in air. Stable and reproducible dielectric properties are obtained only by switching the measuring atmosphere from air to dry N_2. Increased space charge accumulation at the grain boundaries leading to large dielectric constant (ε') and tan δ are measured in air. Much lower tan δ values of 0.021-0.020 are obtained with a large ε' (8,815-11,090) at low frequencies (500-800 Hz) in N_2 at 23°C for 0.5wt.% alumina in both samples sintered at 1080°C and 1100°C suggesting the possibility of developing CCTO for applications as capacitor dielectric.

8.1 Introduction

Perovskite type (ABO_3) CCTO microstructure is well known to be composed of semi conducting grains (n-type) and insulating grain boundaries (GBs) [8, 9]. Although the dielectric mechanism in CCTO are not completely understood until now, the origin of large-ε′ in CCTO ceramics has been widely attributed to barrier layer capacitance effect originated at GBs [9, 25]. The value of dielectric loss (tan δ) is an important parameter determining a dielectric material's suitability for capacitor applications. However, a large value of tan δ (~0.1) in CCTO is still larger than the acceptable values (<0.01) for its capacitor applications [11].

The dielectric loss and ε′ in CCTO are closely related to resistance and capacitance of GBs [8, 9]. Therefore, many researches have focused on optimizing GB characteristics via changing the processing parameters and conditions such as grain size [154], non-stoichiometry [76], sintering conditions [38], and doping [41]. However, preparation of either phase-pure or doped-CCTO materials with a very low tan δ while retaining its ε' above 10^4-10^5 has been challenging. This indicates that CCTO requires additional research to find evidence of factors that are affecting the overall dielectric properties of CCTO.

Doping of various cationic substitutions on either A site (Ca and Cu), or B site (Ti), and/or on both sites have been studied by many. Some recent studies indicated the possibility of doping with Al [1, 41, 42] or Al_2O_3 [45, 46, 155] to modify the CCTO compositions and grain size to enhance the breakdown field. However, some reports indicated that low frequency electrical properties of CCTO measured in air at RT can be

changed either by moisture [57, 58, 156, 157] or by changing the electrode materials being used [21].

CCTO ceramics are reported to have shown an enhanced humidity sensitivity compared with undoped CCTO due to partial substitution of A-site Ca by Mg [157]. While some author studies [23, 139] have shown that as-prepared CCTO sample and electrode contact impedance was sensitive to oxygen in air atmosphere and hence can affect the stability of the electrical properties of CCTO. However, none of the above studies indicated whether the dielectric measurements of doped or undoped CCTO were conducted in a controlled or moisture free atmospheres.

It is reported in the recent work [148, 149] as well as in the Chapter 6 and Chapter 7 in the current research that that air atmosphere can significantly affect the stability of low frequency impedance spectra of pure CCTO ceramics measured at RT (~23°C) despite the sample microstructure or surface conditions (as-prepared and thinned down). As we reported in the Chapter 6 and 7 of the current dissertation and earlier [148, 149, 158] that a relatively stable and repeatable low temperature impedance data are obtained in dry N_2 atmosphere presumably due to elimination of moisture and/or volatile ions from the sample present in the ambient air.

To reliably use the CCTO materials as capacitors, its atmosphere dependent dielectric properties require careful study and elimination for reliable performance. However, to the best of our knowledge, electrical properties of pure and doped CCTO ceramics have not been systematically investigated in various testing atmospheres as a function of frequency and temperatures.

In the light of these shortcomings, the electrical properties of Al_2O_3 doped CCTO ceramics are investigated in the current study by exposing them to moisture/air free testing environments to identify the conditions in which low loss CCTO can be achieved. The alumina doping is expected to reduce conductivity thereby decreasing dielectric loss while maintaining large ε'. This will be possible either by adjusting the defects or changing the concentration of the commonly observed charge carriers in CCTO such as Ti^{4+}/Ti^{3+}, Cu^{2+}/Cu^{1+}, oxygen vacancies, free electrons, and accumulation of ions (such as H^+ and OH^-) due to moisture [73, 150, 151]. These approaches are expected to provide a better understanding of the important roles of surrounding atmosphere and doping on the stability of electrical response of pure and doped CCTO ceramics useful for capacitor application.

The results from this chapter suggest that dielectric properties of CCTO are sensitive to microstructure, doping, and testing atmospheres. A decreased dielectric loss was seen when alumina doped samples were measured in dry N_2 due to large increase of the GB resistance as well as partly due to elimination of conductive charge carriers at GBs.

8.2 Experimental Procedure

As explained in the experimental procedure in the Chapter 4 of this report, phase pure CCTO powder was synthesized by solid-state reaction to achieve stoichiometric ratio (1:3:4:12) using precursors of $CaCO_3$ (VWR, 99.95%), CuO (VWR, 99.7%), and TiO_2 (Sigma-Aldrich, Anatase 99.8%) and calcined at the temperature of 850°C for 6 h in air. To incorporates Al_2O_3 into the finely ground calcined CCTO powders, appropriate amounts of aluminum nitrate ($Al(NO_3)_3.9H_2O$) (Sigma-Aldrich, 99.997%) as per

0.5wt.%, and 4wt.% Al_2O_3 were added to a suspension of calcined pure CCTO powders and mixed in ethanol. Aluminum-nitrate-added CCTO precursors were mixed in ball milled for 24 h in ethanol. Dried precursor powder was then calcined for 6 h at 850°C followed by ball milling for 72 h in ethanol media into fine powders.

Average particle size for all the calcined powders was analyzed using Malvern Zetasizer Ver. 7.11 instruments. Calcined and sieved CCTO powders were mixed with 0.5 weight % PVB (polyvinyl butadiene) binder in ethanol and were uniaxially pressed at 165 MPa into 13 mm diameter and ~2.3 mm thick green pellets. De-binding of the pressed pellets was performed at 500°C for 2 h followed by pre-sintering at 950°C for 5 h and then sintering at different temperatures from 1080°C (S1080) to 1100°C (S1100) for 5 h. Densities of the sintered pellets were determined using Archimedes method.

X-ray diffraction (XRD, Bruker AXS D8 Discover) with Cu-Kα radiation was carried out to confirm the phases present and structural variations in the precursor powders and sintered ceramics. Morphology of precursor powders and the microstructure of sintered samples were examined at RT by Field Emission Scanning Electron Microscope (FE-SEM, Hitachi S-4800) and optical microscopy. The average grain size was determined by the linear intercept method using ImageJ software. Energy Dispersive Spectroscopy (EDS, Oxford INCA Energy 300) was used to identify the type of elements as well as the quantitative chemical analysis of the sintered CCTO samples.

As explained in the experimental procedure in Chapter 4 of this report, impedance was measured at three heating/cooling cycles between 23°C and 225°C for samples placed between two platinum foils first in air and then in dry N_2 atmospheres, respectively. For

electrical impedance measurements, platinum electrodes were applied on the opposing surfaces of as-sintered pellets and were thermally cured at 600°C for 2 h to burn off the solvent/binder. Before applying the platinum paints, CCTO samples were carefully cleaned by ultra-sonicating in acetone.

Real and imaginary parts of the complex impedance Z* (Z*=Z'-jZ", where, $j=\sqrt{-1}$ and Z' and Z", are real and imaginary parts) were measured by two-probe method (using two platinum leads attached to two platinum thin foils) in the frequency range from 1 Hz to 4 MHz and 100 mV AC signal by an impedance analyzer (Solartron 1260A) and dielectric interface (Solartron 1296). Impedance was measured at three heating/cooling cycles between 23°C and 225°C for samples placed between two platinum foils first in air and then in dry N_2 atmospheres. The temperature was measured by a thermocouple mounted close to the sample placed inside a tube (fused silica) furnace.

Before impedance measurements in N_2 atmosphere were carried out, the samples (pure and alumina doped) were thermally cleaned by heating them up to 400°C in dry N_2 and evacuating the chamber for 30 minutes. Complex impedance of the leads/instrument impedance (with no sample) was separately measured and was subtracted from the data before interpretation. More details of the experimental procedures [144, 145] and characterization [148, 149, 158] can be found elsewhere in these references and Chapter 4 and Chapter 5 of this report.

Table 8.1 show the description of the sample thickness, diameter, density, sample surface conditions, and testing atmosphere/temperature for the and as-prepared CCTO/x Al_2O_3 (x=0, 0.5, 4wt.%) samples prepared for ac impedance analysis in the current chapter.

Table 8.1. Description of the Al_2O_3 incorporated CCTO samples used for the analysis of electrical properties.

Description	S1100		S1080	
Wt.% of Al_2O_3	0.5	4	0.5	4
Diameter (mm)	11.44	11.33	11.34	11.01
Thickness (mm)	2.33	2.33	2.32	2.19
Density (g/cc)	4.474	4.547	4.523	4.611
% Relative density	89%	90	90	91
Average grain size (μm)	6.08 ± 0.31	6.45 ± 0.08	6.86 ± 0.15	7.94 ± 0.48
Surface conditions	As prepared			
Testing temperatures	23°C to 225°C			
Testing atmosphere	In air and N_2			

8.3 Results and Discussion

8.3.1 Analysis of Phase Evolution, Microstructure, and Chemical Composition

The average particle size of the calcined and sieved powders was measured as 500 nm [144, 145]. Similar particle size range (250-500 nm) was observed in SEM micrographs as well [144, 145]. The XRD scans indicated in Figure 8.1 (a) and (b) are for the phase compositions of two chosen pure and Al_2O_3 doped (0.5wt.% and 4wt.%) CCTO ceramics. In the current work, XRD pattern in the Figure 8.1 was indexed as per the two references [1, 45].

Apparently, no secondary phases are detected in the pure CCTO samples (S1080 and S1100). As indicated in each Figure 8.1 (a) and (b), a clear separation of secondary reflections from phases like TiO_2 and $CuAl_2O_3$ were seen mostly closer to the major CCTO reflections (211) and (220) in both the alumina doped samples S1080 and S1100.

S1100 shows stronger secondary peaks such as TiO_2 when increasing the alumina doping up to 4wt.%. As can be seen in Figure 8.1 (b), S1100 with 4wt.% Al_2O_3 indicates the presence of $CaTiO_3$ peak as well.

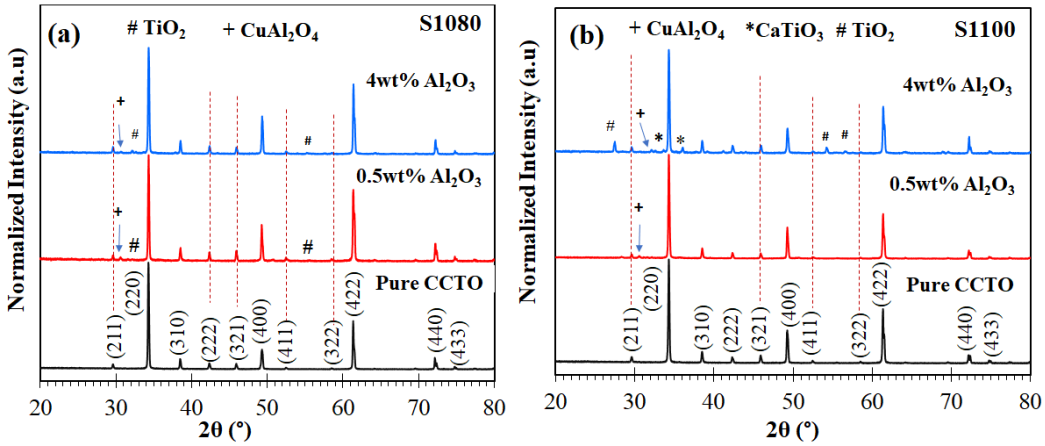

Figure 8.1. XRD patterns of CCTO pure and (0.5wt.% and 4wt.%) Al_2O_3 doped CCTO ceramics sintered at (a) 1080°C and (b) 1100°C for 5 h.

However, mutually exclusive explanations regarding the solid solubility of Al_2O_3 in CCTO (either for the formation of secondary phases or substitution of cations) is reported in earlier studies. According to the first report on Al-added CCTO by authors [41], if the Al_2O_3 doping level is very low (~0.5-1wt.%) Al^{3+} can substitute Ti sites leading to no Al-containing phase. However, authors [45] reported no secondary phases in the 4wt.% Al_2O_3 in CCTO. They [45] observed the presence of $CuAl_2O_4$ with more than 8wt.% Al_2O_3 while TiO_2 and $CaTiO_3$ phases were seen with Al_2O_3 6wt.%-20wt.% in CCTO. Some authors [1] also reported the presence of minor phases of spinel $CuAl_2O_4$ and rutile TiO_2 when CCTO is doped with increased Al_2O_3 (6-10wt.%).

As reported by many for CCTO, when CCTO is sintered at ≥1000°C, liquid copper rich phase with low melting point can act as a sintering aid [18, 35, 147]. Copper rich phase is finally oxidized to composition of CuO upon cooling from sintering temperature [18, 147]. The liquid copper oxide CuO is shown to be mostly segregated at GBs while some of the CuO is reduced to Cu_2O at high sintering temperatures. These CuO/Cu_2O can react with Al_2O_3 in-situ to produce $CuAl_2O_4$ during sintering [1]. In the current work, no CuO phase is seen in either pure or Al_2O_3 doped CCTO ceramics. Its content might be too small to be detected by XRD. However, secondary phases such as TiO_2 and $CuAl_2O_3$ were seen even with 0.5wt.% Al_2O_3 in CCTO indicating the incorporation of Al_2O_3 into CCTO lattice. Therefore, the effect of grain size distribution as a function of alumina content in the CCTO is also further studied. As indicated by SEM in Figure 8.2 (a) and (b), respectively, CCTO with 4wt.% alumina showed a reduction of the grain size with a wide grain size distribution compared with the pure S1100.

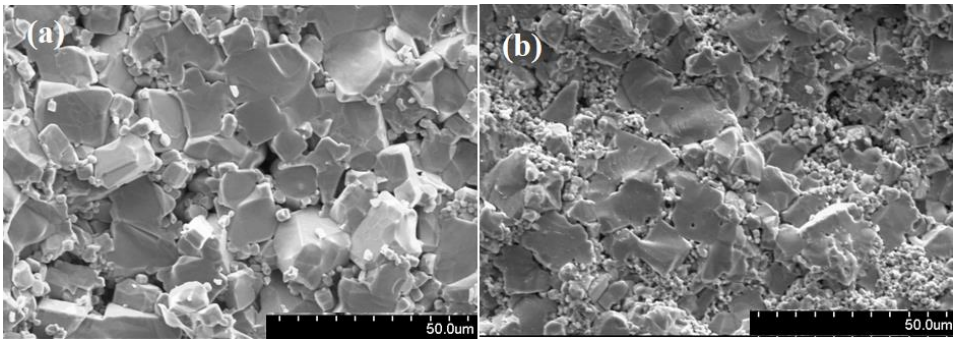

Figure 8.2. Fractured surface SEM micrographs of S1100 (a) pure and (b) 4 wt. % Al_2O_3 doped CCTO samples.

Optical micrographs in Figure 8.3 and Figure 8.4 are from the polished surfaces of various alumina doped samples S1080 and S1100. Pure S1100 and S1080 showed

average grain size of ~7 µm and ~5 µm, respectively, as reported elsewhere [148, 149]. Alumina doped S1080 with 0.5wt.% and 4wt.% show average grain size of ~6.9 µm and ~8 µm, respectively, indicating an increased grain size for the sample with largest alumina content (4wt.%). The average grain size of alumina doped S1100 in Figure 8.4 (a) and (b) estimated as ~6.1 µm (0.5wt.% Al_2O_3) and ~6.5 µm (4wt.% Al_2O_3), respectively, indicating a relatively closer average grain size for both doping levels.

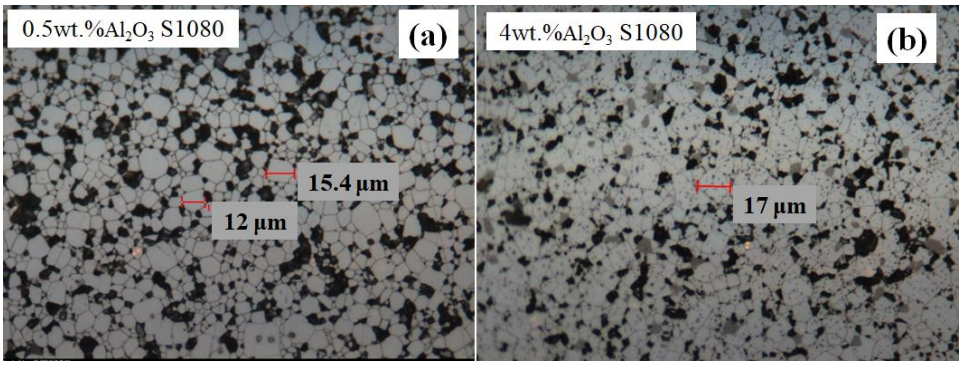

Figure 8.3. Optical micrograph of (a) 0.5wt.% and (b) 4wt.% Al_2O_3 doped CCTO samples S1080 (sintered at 1080°C for 5 h).

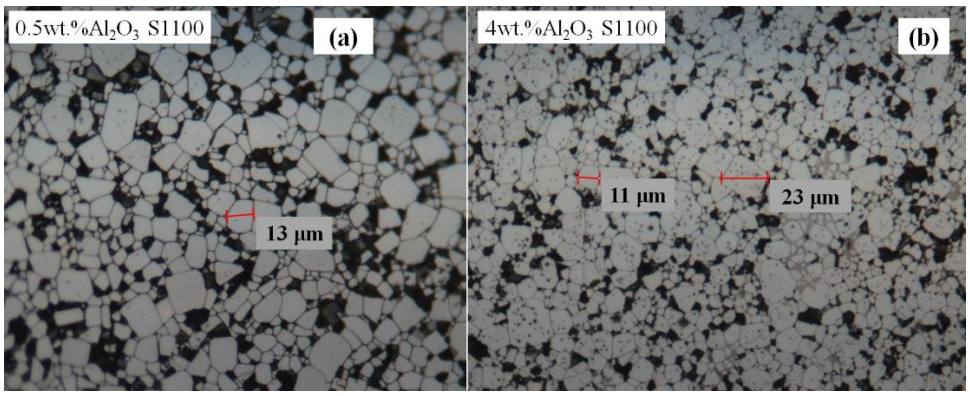

Figure 8.4. Optical micrograph of (a) 0.5wt. % and (b) 4wt. % Al_2O_3 doped CCTO samples S1100 (sintered at 1100°C for 5 h).

SEM micrographs of the polished surfaces of undoped sample S1080 is shown in Figure 8.5 (a) while Figures 8.5 (b) and (c) show the two magnifications of Al_2O_3 doped (4wt.%) CCTO. As indicated in Figures 8.5 (a), the undoped sample S1080 exhibits a duplex microstructure consisting of large sized grains (10-20 µm) with islands of small sized grains (1-2 µm).

As can be seen in Figure 8.5 (b) and its magnified image in Figure 8.5 (c), when the CCTO is doped with 4wt.% Al_2O_3, grain size is increased, and its duplex nature is minimized. At the same time, grain size becomes relatively uniform.

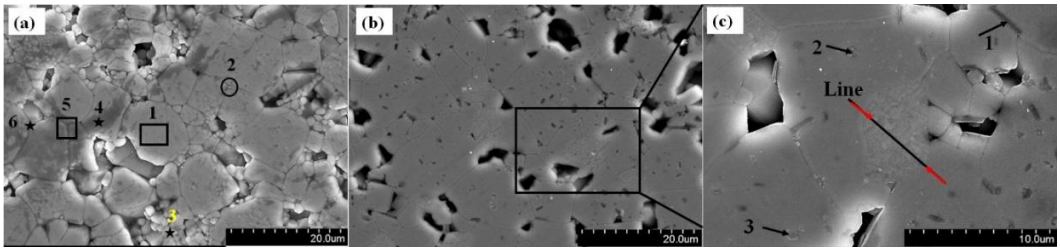

Figure 8.5. SEM micrographs of CCTO sample S1080 (prepared at 1080°C for 5 h) (a) undoped, (b) 4wt.% alumina doped, and (c) is the magnified region indicated in (b).

In order to determine the distribution of elements and the compositions in the inter-grain and intra-grain, EDS of pure and Al_2O_3 doped (4wt.%) S1080 was carried out.

Table 8.2 shows the analysis of distribution of all the elements from various locations shown in Figures 5 (a) for undoped S1080. Stoichiometric ratio of Ca:Cu:Ti:O, which is 1:3:4:12 indicates no compositional variations in intra-grain and inter-grain of undoped S1080.

Table 8.2. Distributions of all the elements of CCTO at different locations shown in Figure 5 (a).

Element	1	2	3	4	5	6
Ca	5.2	5	4.7	5.2	5.2	5.4
Cu	14.9	14.6	12.7	15.2	15.3	15.6
Ti	21.2	20.1	17.4	21.6	21.4	22.3
O	58.6	60.3	65.2	57.9	57.9	56.6
Ca:Cu:Ti:O	1:3:4:11	1:3:4:12	1:3:4:14	1:3:4:11	1:3:4:11	1:3:4:10

EDS area mapping of Figure 8.5 (c) is also measured, and the results are shown in Figure 8.6. Table 8.3 shows the results of EDS analysis of Figure 8.5 (c) and Figure 8.6. As can be seen in Table 8.3, inhomogeneous distribution of Al is seen in both inter-grain and intra-grains regions of Figure 8.5 (c). As indicated by arrow marks in Figure 8.6, the presence of Al in both Ca and Ti sites indicates that Al is co-doped and reacted with CCTO lattice. Furthermore, EDS elemental mapping in Figure 8.6 further confirm that Ca, Cu, and Ti are randomly distributed but the Al has more inhomogeneous distribution. Nevertheless, second phase $CaTiO_3$ is not observed in the XRD results for S1080. This might be due to lower elemental detectability by XRD.

As reported by [78], although Cu-rich phase in CCTO can promote the grain growth during sintering process, CuO particles gradually dissolve in the lattice during the long-time sintering at high temperatures (such as 1060°C for 6 h). This might be the case for observing relatively small variations of the Cu at some of the regions after doping with Al^{3+} in the EDS area mapping in the current experiments. Oxygen ratio in the alumina doped CCTO is also higher than the stoichiometric value of 12. This further confirms that alumina incorporated into CCTO ceramics is not uniformly distributed.

Authors [1] noted the presence of secondary phase of $CuAl_2O_4$ as an important factor to control the liquid phase sintering process in CCTO ceramics. In the current experiments, $CuAl_2O_4$ phase is commonly observed in all the alumina doped samples indicating that liquid CuO/Cu_2O has been consumed to produce $CuAl_2O_4$ which is consistent with the reported behavior of alumina doped CCTO [1].

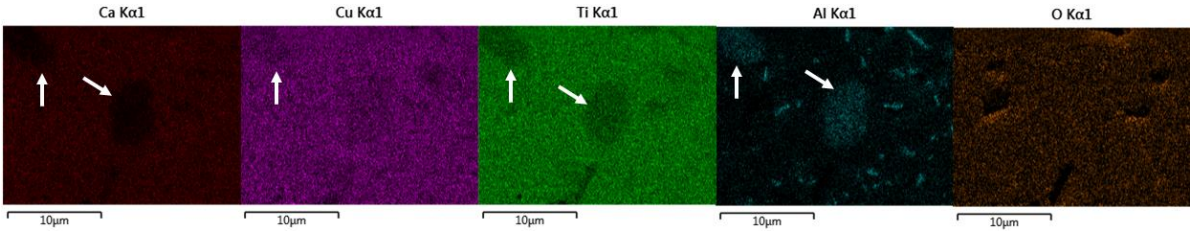

Figure 8.6. Element mapping of the 4wt.% alumina doped CCTO sample S1080 (prepared at 1080°C for 5 h) shown in magnified SEM image of Figure 8.5 (c).

Table 8.3. Distributions of all the elements of CCTO at different location points shown in Figure 8.5 (c) and area element mapping of Figure 8.6.

Element	1	2	3	Map
Ca	3.8	3.4	3.4	4.5
Cu	9.8	9.3	8	14
Ti	14.8	13.6	10.8	19.2
Al	18.4	11	1.5	2.9
O	53.1	62.6	54.7	59.4
Ca:Cu:Ti:Al:O	1:3:4:5:14	1:3:4:3:18	2:5:7:1:16	2:5:7:1:20

Sintered samples were further studied by measuring the relative densities of alumina doped CCTO in the current experiments. We did not observe large variations of the sintered density in alumina doped CCTO. Density of the pure S1080 and S1100, respectively are 4.579 ± 0.048 g/cc (91%) and 4.439 ± 0.05 g/cc (90%). The density of alumina doped S1080 samples with 0.5wt.% and 4wt.% Al_2O_3, respectively are 4.519 ±

0.024 g/cm^3 (90%) and 4.598 ± 0.013 g/cc (91%). While the density of alumina doped S1100 samples with 0.5wt.% and 4wt.% Al_2O_3, respectively are 4.452 ± 0.033 g/cc (88%) and 4.481 ± 0.037 g/cc (89%).

8.3.2 Complex Impedance Spectroscopy

Images in Figure 8.7 show the impedance spectra of S1080 CCTO/xAl_2O_3 (x=0, 0.5, and 4 wt.%) measured at 23°C in air and dry N_2 atmospheres, respectively. The different curves in Figure 8.7 represent the repeated complex impedance (Z*) measurements on the same samples while heating and cooling in air and N_2 atmospheres. It is noteworthy to mention that even with the same electrode material (platinum) used, the total impedance measured at 23°C in air were considerably different and unstable despite the Al_2O_3 doping. However, the total impedance observed (at low frequency) for all the samples at 23°C in N_2 is larger and highly stable when compared with the impedance of the same sample measured in air atmosphere.

Furthermore, the high frequency arcs are indicated in the insets in Figure 8.7 for all the samples measured at 23°C. High frequency data are coincident with each other despite their testing atmosphere suggesting the negligible impedance change in the bulk of the CCTO in both atmospheres. Therefore, it is suggested that atmosphere has a definite role controlling the impedance spectra at low frequencies at 23°C. Impedance spectra of pure and alumina doped CCTO samples (S1100 and S1080) were further studied at high temperatures in both air and dry N_2 atmospheres. Repeatable impedance spectra measurements were observed (not shown here) at high temperatures (≥58°C), irrespective of the measuring atmosphere or alumina doping.

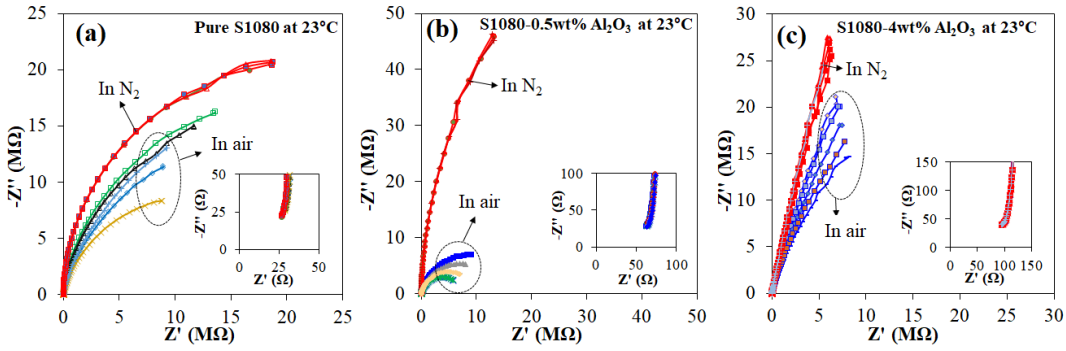

Figure 8.7. Impedance spectra of the same CCTO samples S1080 (a) pure and Al_2O_3 doped CCTO with (b) 0.5wt.% and (c) 4wt.% measured repeatedly in air and dry N_2 atmospheres at 23°C.

Physically adsorbed moisture can change the low frequency impedance of CCTO as reported earlier [156, 157]. Therefore, in the present work, the reason for producing reproducible impedance spectra in dry N_2 can therefore be partly attributed to the removal of physically adsorbed moisture in air due to the thermal treatment of samples to evacuate out the water vapor at 400°C. Above observations further indicates that a stable low frequency impedance measured in dry N_2 seems to be associated with the elimination of mobile ion species due to moisture or air exposure on CCTO GBs, sample surface, on defects, etc. of all the samples.

Figure 8.8 shows a comparison of the impedance spectra of S1080 CCTO/xAl_2O_3 (x=0, 0.5, and 4 wt.%) measured at 23°C and 89°C, respectively in dry N_2. Fully or partially resolved semicircular arcs were seen for all the samples at high temperatures ≥ 58°C with no indication of arc/spike related to sample-electrode contact impedance despite alumina doping or measuring atmosphere. In addition, no electrode sample-contact impedance was observed throughout the measuring temperatures from 23°C to 225°C (not shown

here) suggesting a negligible effect from a possible blocking layer at the sample/electrode interface. This fact implies that the samples studied contain a large number of highly resistive layers presumably at GBs controlling the overall electrical behavior of all these samples.

As shown in Figure 8.8 (a) and (b), large arcs indicate large intercepts on the real axis (Z') at low frequencies for all the alumina doped samples than the pure CCTO measured at the same temperature. High frequency arcs of each samples as indicated in the insets of Figure 8 show a gradual increase of the intercepts on the real axis when alumina doping is increased. Therefore, these results suggest that alumina doping increased both the intra-grain and grain boundary resistances for sample S1080.

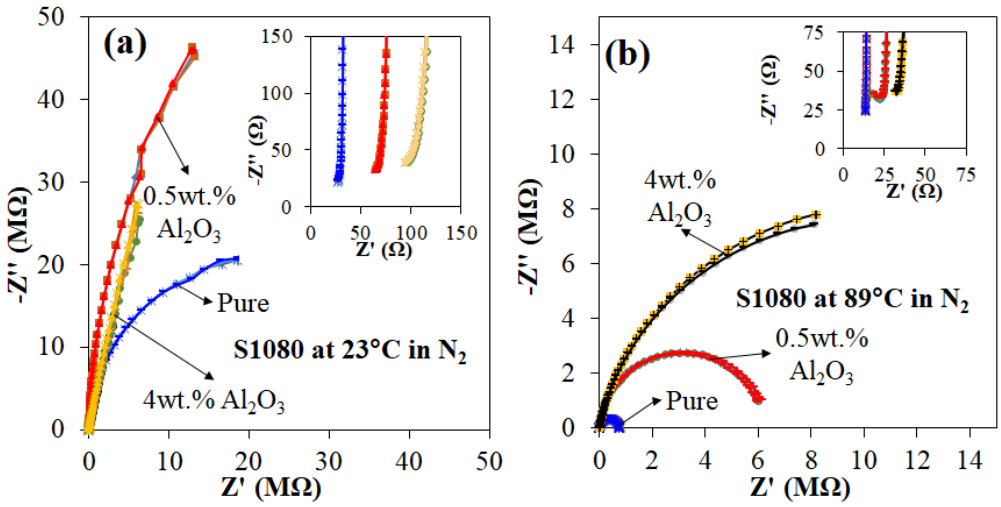

Figure 8.8. Cole-Cole plots of the pure and alumina doped CCTO sample S1080 measured at (a) 23°C and (b) 89°C in dry N_2.

To clearly see the effect of relaxation peaks, frequency and temperature dependent imaginary part (Z'') of S1080 (measured in dry N_2) is separately shown in Figure 8.9. A

dominant presence of single relaxation response can be seen for all the samples despite the Al_2O_3 doping. Peak value of the Z" (at which ωRC=1) represents the maximum in the Cole-Cole diagram, which is shifted to high frequencies with increasing temperatures and to lower frequencies with increasing alumina content. The same behavior was observed for all the same samples measured in air atmosphere (not shown here). This indicates that electrical responses of CCTO are thermally activated irrespective of the measuring atmosphere or Al_2O_3 doping.

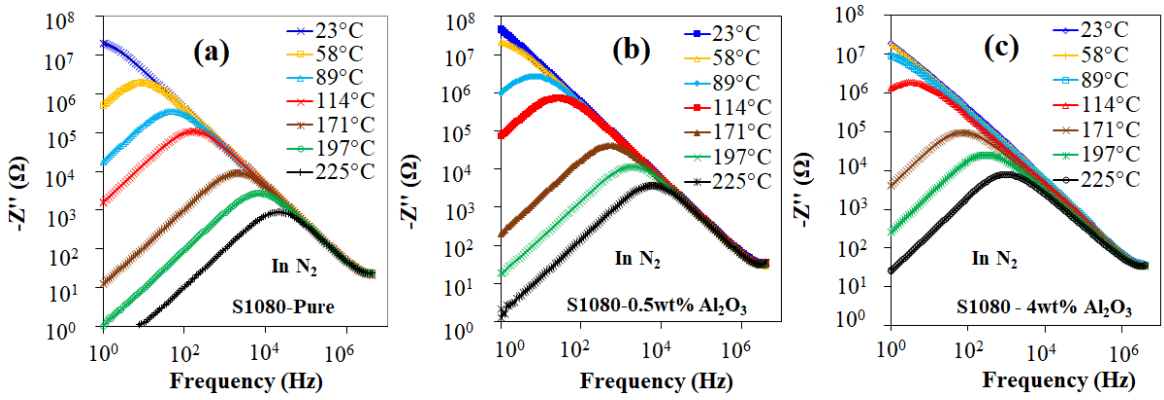

Figure 8.9. Frequency and temperature dependent of imaginary (Z") part of the complex impedance of S1080 of (a) pure and Al_2O_3 doped CCTO with (b) 0.5wt.% and (c) 4wt.% measured in dry N_2.

In the absence of sample-electrode contact effects, the heterogeneous electrical structure of CCTO ceramics can be described by an equivalent circuit consisting of two parallel RC circuits connected in series to represent the resistances and capacitances of grain (RgCg) and GBs (RgbCgb), respectively. Since the single arc is observed in the measured frequency range, Rg can be estimated from a nonzero intercept on the Z' axis at high frequencies while total resistance (Rg+Rgb) is implied by the intercept on the real axis at

low frequencies. The capacitance (C) can be determined by the maximum of each arc at which $\omega\tau=1$ and $\tau=RC$ where, τ is the relaxation time and $\omega=2\pi f_{max}$ is the angular frequency and f_{max} is the peak frequency [50]. Table 8.4 shows the results of equivalent circuit analysis carried out for the pure and two Al_2O_3 doped CCTO samples (S1080 and S1100) measured in N_2.

As seen in Table 8.4, Rgb and total resistivity values of S1100 are increased by two orders of magnitude when increasing the alumina content from 0 to 4wt%. Rgb of alumina doped S1080 increased by an order of magnitude compared to the pure S1080. These results indicate the formation of more resistive GBs in all the samples with alumina incorporated into CCTO. Grain resistance (Rg) is also increased due to alumina doping in both S1080 (30 Ω for undoped and 92 Ω for 4wt.% Al_2O_3) and S1100 (22 Ω for undoped and 120 Ω for 4wt.% Al_2O_3) when they were measured at 23°C in N_2. Increased values of both Rg and Rgb are consistent with the reported behavior for alumina doped CCTO [41, 42, 46].

According to IBLC mechanism, highly resistive GBs and semi-conducting GBs are known to form due to the limited re-oxidation of grains and oxidized GBs in pure CCTO during sintering in air at high temperatures [8, 9]. Therefore, both grain and GB resistivity values are different due to equilibrium concentration of oxygen vacancies, which are formed during sintering. Upon cooling, insulating GBs are re-oxidized faster than that of semiconducting grain interiors leading to the formation of barrier layer effect in CCTO ceramics. The mechanism of conduction in stoichiometric CCTO is attributed to the hopping of the charge carriers (electrons) between the Ti^{4+} and Ti^{3+} or Cu^{2+} and

Cu^{1+} [73, 150, 151]. Some studies proposed that conductivity mechanism in CCTO is mainly due to n-type electron hopping between Ti^{3+} and Ti^{4+} [80].

Behaving as acceptors, if a lower-valent cation Al^{3+} (radius=0.535 Å) substitutes a cation Ti^{4+} (radius=0.605 Å), it can provide positive holes. These holes are able to recombine with the free electrons in the n-type semiconducting CCTO grains increasing the resistance Rg [1, 45]. Behaving as donors, if Al^{3+} substitutes the Ca^{2+} (radius=1.00 Å) or Cu^{2+} (radius=0.730 Å) sites, it can possible to provide extra free electrons in CCTO grains, which in turn can increase the negative charge carriers in CCTO grains leading to decreased Rg [1, 45]. However, in the current experiments, alumina doping has increased the Rg indicating that Al^{3+} seems to occupy in Ti sites mostly in CCTO grains decreasing the charge carrier concentration (electrons) in alumina doped samples (S1080 and S1100). Therefore, Rg found to increase in alumina doped samples compared with the undoped CCTO can be attributed to the removal of conduction of free electrons in semiconducting grains.

On the other hand, it is shown in the literature that more insulating $CuAl_2O_4$ is segregated preferably at GBs leading to higher GB resistance as well [47, 48]. Therefore, much larger Rgb values in alumina doped CCTO in the current experiments can be related to much resistive secondary phases at GBs (highly resistive GBs). EDS analysis showed that $CuAl_2O_4$ in the inter-grain regions might be the reason for large Rgb values in both the alumina doped S1080 and S1100 in the current experiments.

Increasing the measuring temperature has decreased the total resistance of all the samples despite the alumna doping indicating thermal activated charge carriers in CCTO. Another

essential aspect to consider is an increased Cgb when alumina content is increased in S1080. On the contrary, S1100 show progressively decreasing Cgb as the alumina addition is increased. Much larger Cgb in alumina doped S1080 than that of S1100 indicates that the alumina doped S1080 has smaller Rgb compared with the alumina doped S1100. This is because Cgb was estimated by peak values of the Cole-Cole diagrams at which Cgb=1/(ωRgb) and Rgb is smaller for S1080. It seems that combined effect of both microstructure and secondary phases has led to the observed changes in the Rgb, Cgb, and Rg.

Table 8.4: Comparison of the equivalent circuit analysis of the pure and Al_2O_3 incorporated CCTO samples S1100 and S1080 measured in dry N_2.

Temp.(°C) ± 2°	Pure S1080 in N_2				CCTO/0.5wt%Al_2O_3 S1080 in N_2				CCTO/4wt.% Al_2O_3 S1080 in N_2			
	Cgb (nF)	Rgb (Ω)	Rg (Ω)	ρ (Ωcm)	Cgb (nF)	Rgb (Ω)	Rg (Ω)	ρ (Ωcm)	Cgb (nF)	Rgb (Ω)	Rg (Ω)	ρ (Ωcm)
23	3.9	4.2E+07	30	1.8E+08	3.1	1.8E+08	68	7.9E+08	4.8	1.9E+08	92	8.1E+08
58	4.4	4.2E+06	19	1.8E+07	3.0	4.3E+07	39	1.9E+08	7.2	9.4E+07	31	4.1E+08
89	4.1	7.9E+05	13	3.4E+06	2.0	6.2E+06	26	2.8E+07	8.6	1.8E+07	20	7.8E+07
114	3.9	2.3E+05	11	1.0E+06	3.4	1.7E+06	20	7.4E+06	9.0	3.1E+06	15	1.4E+07
171	4.1	1.9E+04	6	8.2E+04	3.1	9.0E+04	10	4.0E+05	8.4	1.4E+05	12	6.1E+05
197	4.0	5.8E+03	5	2.5E+04	3.4	2.5E+04	10	1.1E+05	7.6	3.3E+04	12	1.4E+05
225	3.9	1.9E+03	4	8.4E+03	3.2	8.0E+03	6	3.6E+04	8.1	1.2E+04	11	5.4E+04
Temp.(°C) ± 2°	Pure S1100 in N_2				CCTO/0.5wt%Al_2O_3 S1100 in N_2				CCTO/4wt.% Al_2O_3 S1100 in N_2			
	Cgb (nF)	Rgb (Ω)	Rg (Ω)	ρ (Ωcm)	Cgb (nF)	Rgb (Ω)	Rg (Ω)	ρ (Ωcm)	Cgb (nF)	Rgb (Ω)	Rg (Ω)	ρ (Ωcm)
23	5.7	1.3E+07	22	8.5E+07	3.9	1.7E+08	50	7.3E+08	2.4	4.4E+08	120	1.8E+09
58	5.3	1.1E+06	14	7.2E+06	4.0	2.2E+07	26	9.8E+07	2.3	2.9E+08	66	1.2E+09
89	5.2	1.8E+05	10	1.2E+06	4.0	3.5E+06	18	1.6E+07	2.2	4.9E+07	43	2.0E+08
114	5.2	4.7E+04	7	3.1E+05	3.9	9.2E+05	13	4.1E+06	2.4	1.4E+07	32	5.5E+07
171	5.3	4.3E+03	5	2.8E+04	4.1	5.4E+04	7	2.4E+05	2.2	6.4E+05	17	2.6E+06
197	5.3	1.7E+03	4	1.1E+04	4.0	1.5E+04	6	6.8E+04	2.1	1.6E+05	16	6.5E+05
225	5.3	7.1E+02	4	4.7E+03	3.8	5.0E+03	5	2.2E+04	2.3	4.5E+04	10	1.8E+05

Temperature dependent DC resistance (Rg and Rgb) and dc resistivity increases as the alumina concentration in CCTO is increased [41]. These authors [41] observed pure CCTO with grain activation energy of 0.05 eV was unchanged upon increasing the alumina doping. However, they [41] observed that GB activation energy was increased

from 0.52 eV (pure) to 0.65 eV (0.5wt.%) when increasing the alumina doping content. This trend is true in the current experiments as well.

In the current experiments, the fitted values of Rgb and Rg (for both S1080 and S1100) are plotted as a function of temperature.

A linear relationship could be seen despite the alumina doping in CCTO. DC resistance of grains and GBs of the pure and alumina doped S1080 and S1100 are plotted against temperature in Figure 8.10, which clearly indicate that increasing the alumina content increases the activation energy of GBs (Egb) (~0.62 eV for pure and 0.76-0.78 eV for 4wt.% Al_2O_3).

However, activation energy for intra-grains (Eg) is only slightly changed for alumina-doped samples (0.08-0.16 eV for 4wt.% Al_2O_3) compared to the undoped (0.12-0.13 eV).

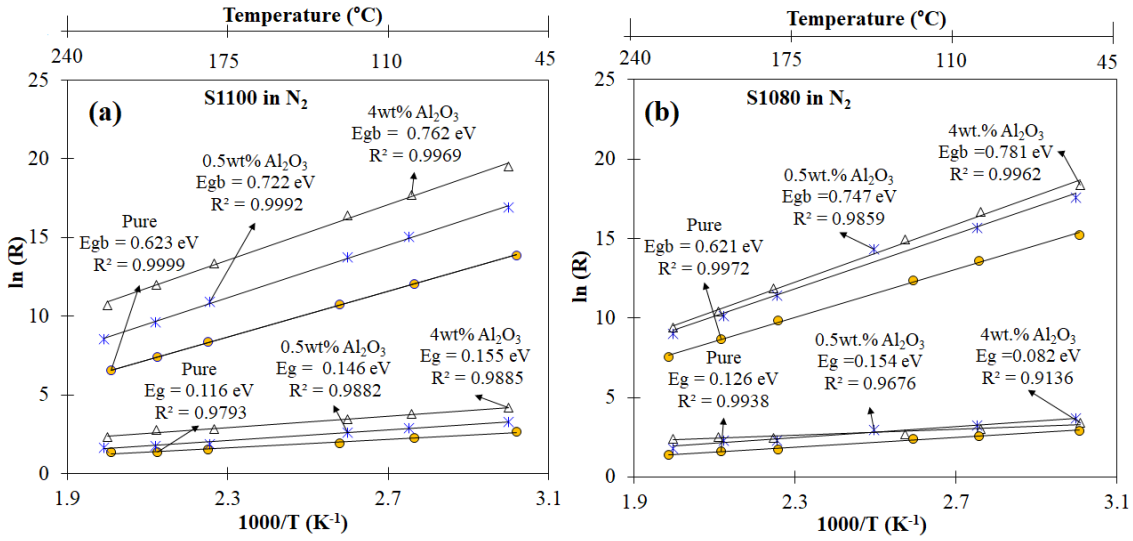

Figure 8.10. DC resistances of grain boundary and grain as a function of temperature measured in N_2 for pure and alumina doped CCTO (a) S1100 and (b) S1080.

8.3.3 Dielectric Properties

In order to gain more information of the effect of atmosphere, dielectric constant, ε' (real part of the complex relative permittivity, ε*= ε'-jε"), dielectric loss factor, ε" (imaginary part of ε*), and loss tangent (ratio of ε"/ε') were further studied for samples exposed to different atmosphere as described below. Figure 8.11 and Figure 8.12 represent the ε' for samples S1080 CCTO/xAl_2O_3 (x=0, 0.5, and 4 wt.%) measured in air and dry N_2 at 23°C and at 89°C, respectively.

Irreproducible behaviors of ε' observed at frequencies from 1 Hz to below ~1 MHz in air atmosphere at low temperatures (23°C) is seen for all the samples despite the alumina doping. However, unstable ε' are eliminated for all the samples by changing the measuring atmosphere from air to N_2. Furthermore, as can be seen in Figure 8.12, insignificant changes in ε' are seen when the measuring temperature is increased (89°C) despite the atmosphere. These results further confirm that CCTO can produce the repeatable ε' irrespective of the atmosphere (air or N_2), doping, provided that the measuring temperature is above 23°C or the measurements are done in controlled atmosphere.

As can be seen in Figure 8.11(a)-(b) and Figure 8.12(a)-(b), a relatively frequency independent and slightly decreased ε' is seen in both the pure and 0.5wt.% Al_2O_3 doped sample S1080 tested in N_2 over the frequency from 100 Hz to 1 MHz for both the samples in dry N_2. Conversely, as indicated in Figure 8.11(c) and Figure 8.12(c), an abnormally large increase of ε' is observed at low frequencies when the doping level is increased from 0.5wt.% to 4wt.% for S1080 especially in N_2 atmosphere.

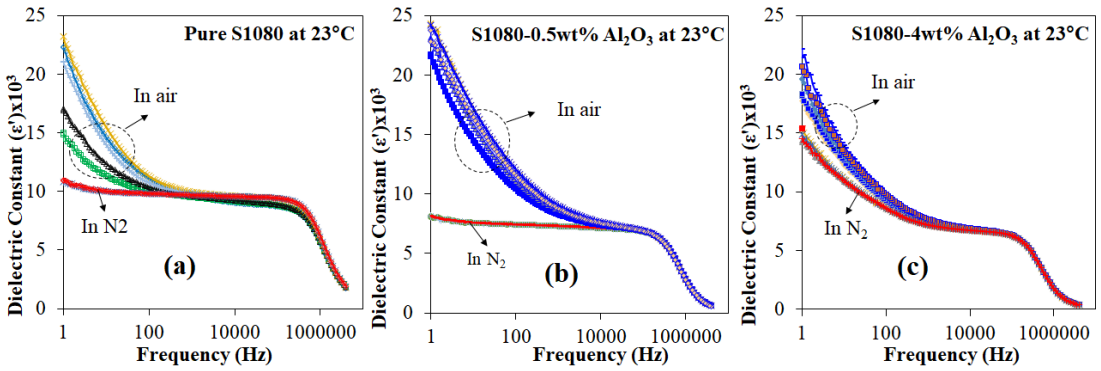

Figure 8.11. Frequency dispersion of the dielectric constant (ε′) of the CCTO samples S1080 (a) pure, (b) 0.5wt.%, and (c) 4wt.% Al_2O_3 measured at 23°C in air and dry N_2.

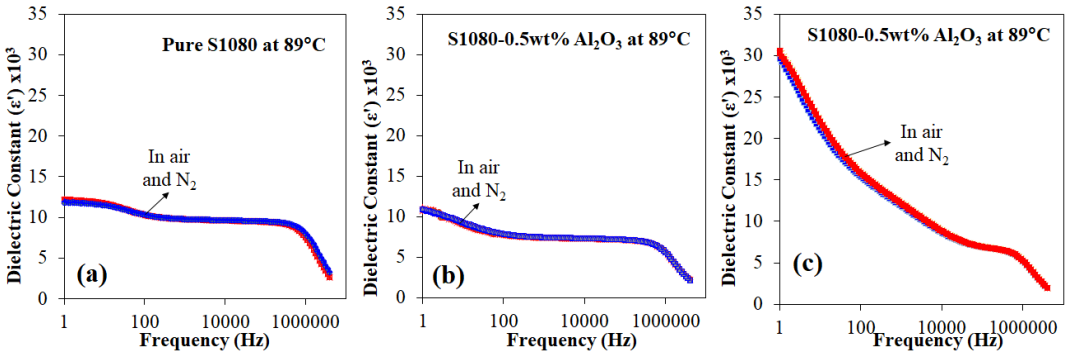

Figure 8.12. Frequency dispersion of the dielectric constant (ε′) of the CCTO samples S1080 (a) pure, (b) 0.5wt.%, and (c) 4wt.% Al_2O_3 measured at 89°C in air and dry N_2.

As reported earlier by several groups, Al_2O_3 doped CCTO samples show a decreased ε' when increasing the alumina content. Authors [41] observed a slightly reduced ε' for the Al_2O_3-doped CCTO (at 10 kHz ε' were 58000, 41000, and 27000 for the pure, 0.5wt.%, and 1wt.% Al_2O_3, respectively). This is true in the current experiments where, S1080 showed a decreased ε' when increasing the alumina content (at ~10 kHz ε' were 9567 ± 2, 7138 ± 0, and 6735 ± 1 for the pure, 0.5wt.%, and 4wt.% Al_2O_3 in CCTO, respectively).

In contrast, alumina doping in CCTO can also result in an increased or decreased ε'. Authors [42] reported varied values of ε' at 1 kHz for Al_2O_3 doped CCTO such as pure, 1wt.%, 3wt.%, and for 5wt.%, respectively as 12050, 16000, 12710, and 28600. This behavior is true in the current experiments for S1080 when the frequency is low (between 1 Hz and ~1 kHz). In the current experiments, ε' at 400 Hz are 9738 ± 6, 7360 ± 1, and 7599 ± 2 for the pure, 0.5wt.%, and 4wt.% Al_2O_3 in CCTO, respectively when measured in dry N_2.

Therefore, behavior of ε' was further studied as a function of temperature to find more clues for large ε' only in S1080 with 0.5wt.% Al_2O_3. Frequency dependency of ε' in S1080 (pure and alumina doped) measured in dry N_2 from 23°C to 197°C are shown in Figure 8.13. As noted in Figure 8.13, effective ε' at step 2 is larger than that at step 1 (high frequency) despite the alumina content in each S1080. Step like decrease at low frequencies is shifted to higher frequencies when increasing temperatures for pure and alumina doped CCTO.

Relatively temperature and frequency-independent two plateau regions (step 1 and step 2) of ε' with two reduction steps is seen only in pure and 0.5wt.% Al_2O_3 doped S1080. A wide two plateaus (from 1 Hz to 1 MHz) indicates a relatively stable and consistent ε' over a large range of frequencies when measured in N_2 only for pure and alumina doped CCTO with 0.5wt.% alumina. However, step 2 (at low frequency) is becoming highly temperature and frequency dependent for sample S1080 with 4wt.% alumina. Step 2 is only observed at higher temperatures for all the samples despite the alumina doping as can be seen in Figures 8.13 (a), (b), and (c).

In the current experiments, the sharp decrease of ε′ at high frequencies (>1 MHz) is most probably due to relaxation of dipoles related to CCTO grains. At higher frequency molecular orientation time is reduced and hence polarization cannot follow the externally applied field. The reported behavior of high frequency relaxations of CCTO ceramics is attributed to the defect induced relaxation via ordering of electrons and oxygen vacancies on mixed valence Ti^{3+}/Ti^{4+} and Cu^{1+}/Cu^{2+} [73, 150, 151]. Upon increasing the temperature from 23°C to 197°C, no noticeable shift of the high frequency relaxation is observed for S1080 despite the Al_2O_3 doping.

On the other hand, the plateau and another step like increase of ε' at low frequencies is usually attributed to space charge effect at GBs, which arise due to complex polar ordering of space charges and the hopping of electronic defects between them [9, 133]. Since the response time of the charge motion involved in the space charge accumulation is higher, they are typically observed at low frequencies [142]. Therefore, the differences in two steps of S1080 (step 1 and step 2) in Figure 8.13 can be attributed to the presence of space charge polarization at GBs at low frequencies.

According to IBLC mechanism, the grains act like electrodes of micro-capacitors connected in series and GBs play the role of the dielectric in between. Within this framework studies indicated that effective ε' of CCTO is directly proportional to the Cgb at frequencies much lower than the dielectric relaxation frequency [97]. Therefore, observed changes in ε' in the current experiments can be related to fitted values of Cgb. A large value of Cgb as large as~5-9 nF was observed in S1080 with 4wt.% alumina compared with the same with the 0.5wt.% alumina (~3 nF) and undoped (~4 nF) CCTO

samples. Therefore, large effective ε' in the 4wt.% alumina doped S1080 sample at low frequencies can be attributed to its large Cgb. Therefore, our results appear to be agreeing with the barrier layer capacitor model relations explained by the reference [97].

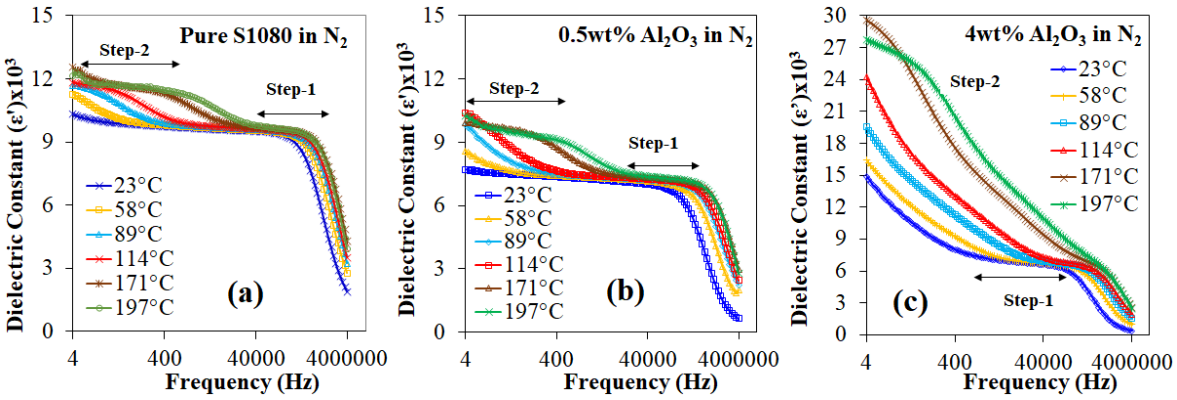

Figure 8.13. Dietetic constant (ε') of the CCTO sample S1080 (a) pure, (b) 0.5wt.%. and (c) 4wt.% alumina measured in dry N_2.

The alkaline cations on A-sites of perovskite-type oxides (ABO_3) ceramics are sensitive to humidity and partial substitution of A site elements can enhance the humidity sensitivity [159, 160]. This enhancement was attributed to a strong electronic interaction between the adsorbed species and the oxides surface [159, 160]. Some studies have also reported earlier that humidity sensitivity of CCTO microstructure can be enhanced due to Mg^{+2} doping onto Ca sites such that a second phase $CaTiO_3$ is formed. Alternatively, $CaTiO_3$ is reported [161] as an excellent humidity sensitive material. However, even after evacuating the system at 500°C chemically absorbed moisture (OH^-) is difficult to eliminate completely [126] as reported earlier for ceramic oxides. Therefore, chemically adsorbed moisture (OH^-) could still exist in CCTO samples of the current study.

Therefore, another hypothesis to explain the difference in ε' observed in S1080 can be the modified moisture sensitivity and defects at GBs. In the current experiments, EDS analysis and XRD show strong evidence of random occupation of Al^{3+} on both the Ca and Ti sites in CCTO and changes in the concentration of oxygen vacancies (Vos) in both inter and intra grains due the presence of Al^{3+} in CCTO lattice. As reported for other perovskite-type titanates (PZT) by other authors [162] that donor doping did not completely suppress the formation of Vos but rather accumulated near GB regions. They [162] also noted that co-doping by acceptors and donors in PZT can change conductivities due to changes in concentration of Vos when keeping the net dopant concentration constant [162]. It is also known that doubly charged Vos actually serve as active absorbing centers for water absorption [163]. Another report [163]also indicated that when Ti sites are replaced by acceptors, the resulting electrostatic field of the defects can dissociate the absorbed H_2O leading to the formation of OH^- groups and serve as active centers for chemisorption of water molecules.

These observations indicate the possibility of increased accumulation of charge at GBs due to Al_2O_3 doping and moisture absorption in CCTO. This might be the case for highly Al_2O_3 doped (4wt.%) CCTO as can be seen in Figure 8.13 (c) hence a large low frequency ε'. Secondary charge at GBs seem to be highly volatile even at low temperatures as can be seen in the large spread in ε' in Figure 8.13 (c) for S1080 with 4wt.% Al_2O_3 compared with other two samples (pure and 0.5wt.% Al_2O_3 doped S1080).

Therefore, an unstable ε' in air can be attributed to space charge polarization at GBs due to accumulation of more charge carriers at GBs. When CCTO samples were exposed to

air, accumulation of ions such as H^+ and OH^- (or some dissolved ions in the moisture) can happen in addition to native point defects in CCTO. Therefore, space charge polarizability at GBs can be varied depending on the concentration of defects in the CCTO structure [75, 81]. Accumulation of these charges at the highly resistive GBs can give rise to a large Cgb leading to large effective ε' in all the samples measured in air atmosphere.

When changing the measuring atmosphere from air to N_2, the large dispersion of the dielectric loss factor, ε″ (imaginary part of complex relative permittivity, ε*= ε'-jε") is suppressed and became stable as shown in Figure 8.14. Despite the measuring atmosphere or alumina doping, the ε″ shows large value at both low and high frequencies. Since the loss factor is unstable when measured in air atmosphere, the shapes of the ε″ measured in dry N_2 as a function of frequencies and temperatures (from 23°C to 225°C) were further studied to understand the conduction and dielectric relaxation mechanisms due to the presence of alumina in CCTO ceramics.

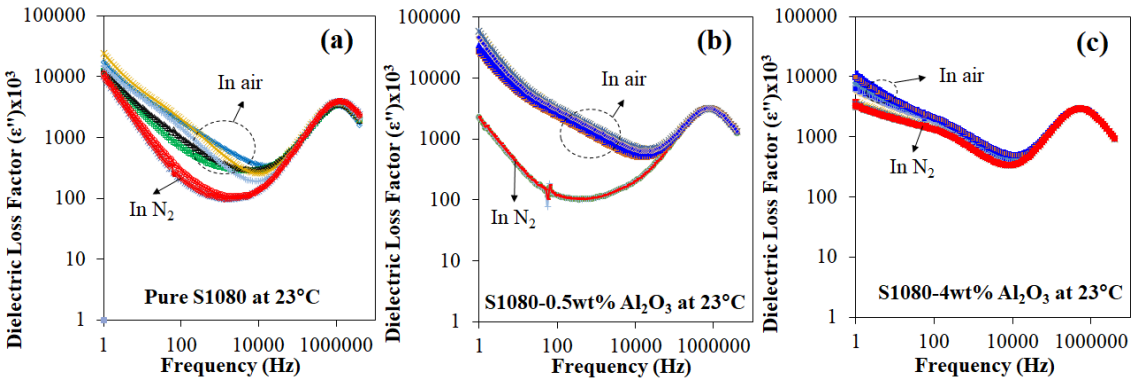

Figure 8.14. Frequency dispersion of the dielectric loss factor (ε″) of the CCTO samples S1080 (a) pure, (b) 0.5wt.%, and (c) 4wt.% Al_2O_3 measured at 23°C in air and dry N_2.

Figure 8.15 (a), (b), and (c) show ε″ measured in N_2 for pure and alumina doped CCTO S1080 at different temperatures. A sharp increase of ε″ at low frequencies (toward 1 Hz) followed by a peak maximum around ~1 MHz with a minimum at ~ 10 kHz is seen for all the samples despite the doping. These observations further confirmed the strong dielectric dispersion at low frequencies followed by merged peaks at high frequencies by impedance analysis (see Figure 8.9).

Dipole relaxation process is identified by the peak of the imaginary part (ε") and step like decrease in the real part (ε') of the complex dielectric function when increasing the frequency. Therefore, the presence of high frequency loss peak (>1 MHz*)* can be attributed to relaxation of dipoles due to mobile charge carriers that do not involve long range motion that are related to the bulk CCTO [50]. On the contrary, presence of dc conductive losses (ohmic) and space charge relaxation at low frequencies can be identified by the slope in ε", which is greater than negative one (>-1) [142].

Therefore, a slope of ε" (toward 1 Hz) and orders of magnitudes large ε″ than ε′ toward low frequencies in the current study further confirm the presence of dc conduction and space charge relaxation in CCTO despite the doping and measuring atmosphere. As shown in the Figure 8.15 (a) a steep slope is seen for the pure S1080, which is decreasing when alumina doping is increased. At low frequencies toward 1 Hz, a slope changes in ε" are smaller for S1080 with 4wt.% alumina compared with pure and 0.5wt.% alumina. This indicates that conduction losses are reduced at low frequencies due to the presence of highly resistive GBs in Al_2O_3 doped CCTO. Conduction losses in all the samples on

the other hand indicates the existence of non-blocking (i.e. ohmic) sample-electrode contact and partially blocking GBs.

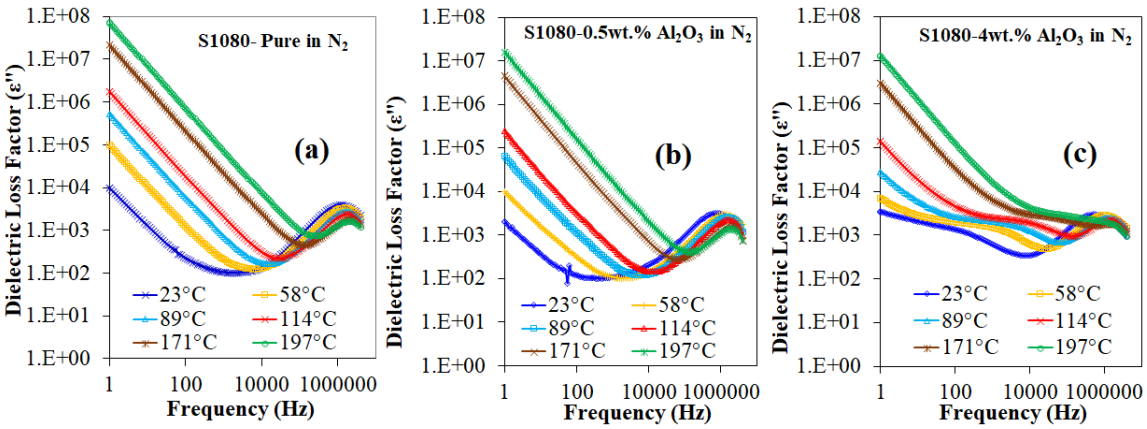

Figure 8.15. Dietetic loss factor (ε") of the CCTO sample S1080 (a) pure, (b) 0.5wt.% and (c) 4wt.% alumina measured in dry N_2.

Dielectric loss tangent, tan δ (ratio of ε"/ε'), values of the different CCTO/Al_2O_3 samples S1080 are presented in Figure 8.16. Increased mobile charge carriers due to humidity can increase the electrical conductivity leading to increased tan δ in air atmosphere [159, 160]. As can be seen in Figure 16, a reduced tan δ in dry N_2 for all the samples can be attributed to the removal of moisture and mobile ions due to humidity that are enhancing the large conductivity and space charge polarization at GBs.

A large increase of tan δ is observed even in dry N_2 can be seen at very low and at high frequencies for all the CCTO/Al_2O_3 samples despite the doping. Therefore, tan δ of the current CCTO samples is the total energy loss due to the dielectric relaxation process (space charge and dipole relaxation) and ohmic conduction [11]. Similar trend was seen in Al_2O_3 doped S1100 (not shown here).

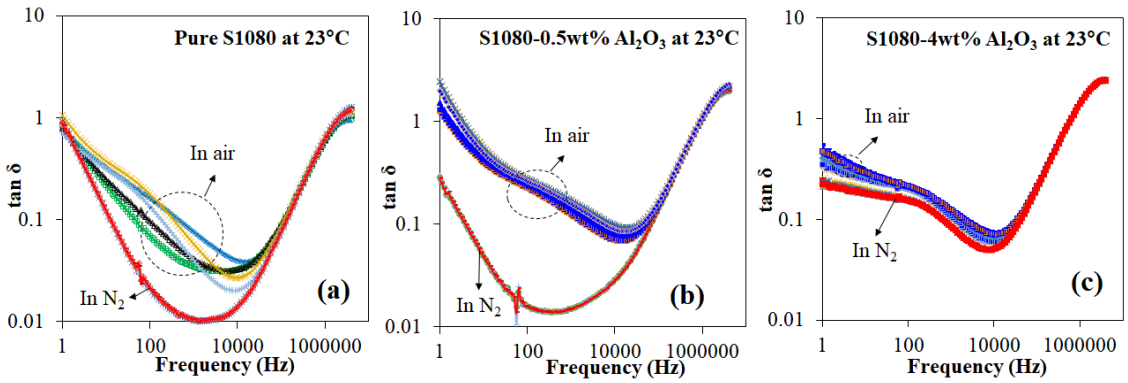

Figure 8.16. Frequency dispersion of tan δ of the same CCTO sample S1080 (a) pure, (b) 0.5wt.%, and (c) 4wt.% Al_2O_3 measured at 23°C in air and dry N_2.

Suppression of tan δ over the low frequency range (<100 Hz) in the alumina-doped sample indicates the reduction of the degree of charge carrier movements that are contributing to conduction losses. In order to clearly observe the reduction of dielectric loss at much lower frequencies due to alumina doping, Figure 8.17 (a) and (b) show a comparison of tan δ of CCTO S1080 measured at 23°C and 89°C, respectively in dry N_2. As seen in Figure 8.16, tan δ is significantly decreased over the entire frequency range <10 kHz for all the samples.

The smaller low frequency tan δ are seen for aluminum doped samples even at high temperature (89°C). However, tan δ is still large for all the samples at 89°C despite the doping indicating conduction losses due to thermal activation of charge carriers across GBs. A large increase of tan δ is seen at frequencies higher than >10 kHz for the sample S1080. At much higher frequencies > 10^5 Hz the samples show increased tan δ indicating dipole relaxation losses.

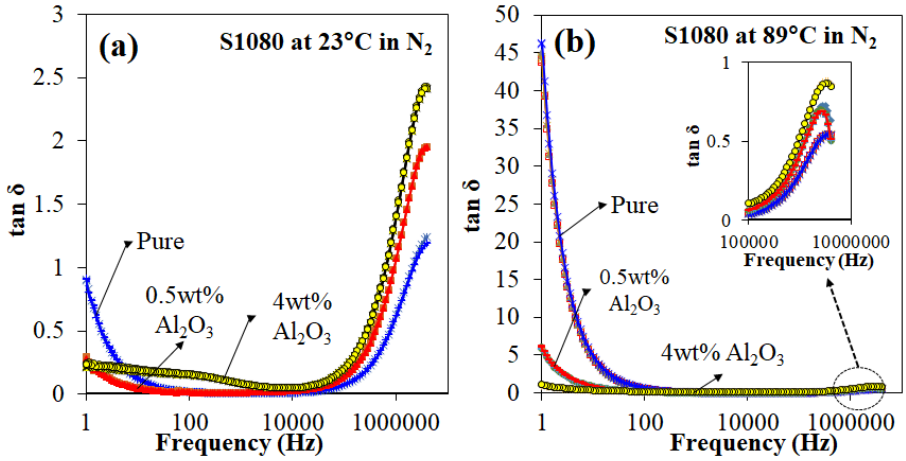

Figure 8.17. tan δ of the pure and alumina doped CCTO sample S1080 measured at (a) 23°C and (b) 89°C in dry N_2.

Some studies [42] reported minimum tan δ value as 0.070 for alumina doped CCTO (0.5wt.% Al_2O_3) at 100 Hz-10 kHz with ε' of 12710. Other authors [155] reported much lower tan δ as low as 0.038 (with ε' of 20000) at low frequency range by Al_2O_3 doping. While another work [41] reported the lowest value of tan δ for alumina doped CCTO of 0.034 (0.5wt.% Al_2O_3) at 10 kHz with ε' of 41000.

By comparison, tan δ values in the current work highlighted that the alumina doped (0.5wt.%) S1080 show tan δ of 0.031-0.033 in the range of frequencies 40 Hz-4 kHz with large value of ε' (~11000-12000). These tan δ values are smaller than the reported values (0.034) [41] indicating the enhanced tan δ in the current CCTO samples. Undoped CCTO sample S1100 in the current work shows tan δ as small as 0.043-0.061 in a wide range of frequencies from 40 Hz to 40 kHz (with ε' of ~8400-9200). It is important to notice in the current experiments that tan δ are lower than 0.5 at 23°C at the frequency range of < 10 MHz for all the samples S1080 and S1100 (pure and Al_2O_3 doped).

In the current experiments, minimum values of tan δ of CCTO/Al_2O_3 (S1080 and S1100) samples measured in dry N_2 are shown in Table 8.5. Lower tan δ values of 0.021 and 0.020 for S1080 and S1100, respectively, can be seen with relatively large ε' of 8,815-11,090 at much lower frequencies (500-800 Hz). For the best of our knowledge the minimum tan δ values in the current experiments are lower than the lowest reported values for alumina doped CCTO (500-800 Hz) measured at RT. Table 8.5 also indicates that ε' is decreased when increasing the alumina content up to 4wt% at the minima values of tan δ for both S1080 and S1100. However, S1080 with 4wt.% Al_2O_3 shows a large ε' toward low frequencies (1 Hz) much lower than the frequency related to the minima (~1 kHz).

Table 8.5. Minimum values of dielectric loss and its corresponding ε', ε'', and frequencies measured at 23°C in N_2 atmosphere for pure and alumina doped (0.5-4wt%) CCTO samples (S1080 and S1100).

Sample	S1080 Measured in N_2 at 23°C				S1100 Measured in N_2 at 23°C			
	Frequency (Hz)	ε'	ε''	tan δ	Frequency (Hz)	ε'	ε''	tan δ
Pure CCTO	1400	9663	101	0.010	2200	12935	176	0.014
0.5wt.% Al_2O_3	500	11090	235	0.021	798	8815	176	0.020
4wt.% Al_2O_3	7981	6767	346	0.051	1419	4988	233	0.047

These observations justify the fact that the addition of alumina doping can produce a more resistive GBs, which resulted in a low dielectric loss at low frequencies.

CHAPTER IX

CONCLUSIONS

This dissertation performed fundamental research focused on the synthesis, characterization, and electrical properties of phase pure and Al_2O_3 doped $CaCu_3Ti_4O_{12}$ (CCTO) dielectric materials as a function of testing atmosphere (air and dry N_2), sample thickness, and temperatures. We hope new approach of characterizing CCTO ceramics and findings described below could be used as guidelines for future investigations on pure and doped CCTO to be useful in capacitor application.

9.1 CCTO Powder Processing and Sintering

Phase pure CCTO powders were synthesized at relatively low calcination temperatures (850°C for 6 h). In this study, phase purity, microstructures, and densities of CCTO. samples namely S1060 (sintered at 1060°C for 5 h), S1070 (sintered at 1070°C for 5 h), S1080 (sintered at 1080°C for 5 h), S1100 (sintered at 1100°C for 5 h), and S1115 (sintered at 1115°C for 5 h) were studied.

Duplex nature of the microstructure with a wide grain size distribution (1-20 μm) was observed in samples sintered at low sintering temperatures (<1100°C). The duplex nature of grains was relatively minimized at very high sintering temperature of 1115°C. Largest average grain size was seen in S1100 (~7 μm) and S1115 (~8 μm).

Sample S1060 shows the maximum value of relative density at 4.735 ± 0.065 g/cm^3 (94% of the theoretical density - 5.049 g/cm^3). Samples sintered at high temperatures, S1100 and S1115 showed a value of 4.439 ± 0.050 g/cm^3 and 4.585 ± 0.019 g/cm^3, respectively Density of the sample sintered at 1070°C for 5 h was 4.669 ± 0.042 g/cm^3 (92%), which was within the density variation observed for sample sintered at 1060°C. The lowest density was observed for sample sintered at 1050°C for 5h, which is 4.326 ± 0.028 g/cm^3 (86%).

9.2 Effect of Measuring Atmosphere and Temperature

This study investigated the effect of testing atmospheres on the dielectric properties of two CCTO samples namely S1070 (sintered at 1070°C for 5h) and S1100 (sintered at 1100°C for 5h). Impedance spectra were measured from 23°C to 225°C and analyzed while exposing the samples to both air and dry N_2 atmospheres. The following conclusions can be drawn from this study.

- The sample S1070 showed larger impedance than that of S1100 because of the large number of resistive GBs (smaller grains) suggesting that significant variations in impedance of CCTO can be realized by changing the microstructure.

- Highly irreproducible impedance spectra were observed when samples were tested in ambient air at 23°C despite the changes in the microstructure of the samples. Switching the measuring atmosphere from ambient air to dry N_2 lead to reproducible impedance spectra for all the measuring temperatures.
- Frequency dependent impedance data could be fitted with only contributions from grain and grain boundaries. There was no evidence of electrode-sample interface contribution to the impedance. Impedance analysis showed that the impedance and capacitance of grain boundaries (GBs) were very sensitive to measuring atmosphere at low temperatures (23-58°C).
- Unusually large dielectric constant observed in air atmosphere at lower frequencies was suppressed substantially when samples were tested in dry N_2. A small relaxation still existed below 100 Hz even in dry N_2, which was attributed to chemically absorbed moisture that might still be present in the samples.
- At higher measuring temperatures beyond 58°C, the effect of atmosphere on dielectric constant and loss tangent was reduced for both the samples.
- Dielectric loss was also greatly reduced by switching the testing atmosphere from air to dry N_2 at lower measuring temperatures (23-58°C). The lowest tan δ for the sample S1070 and S1100, respectively, were 0.015 ± 0.001 (at ε' of $8,841 \pm 3$ and 4 kHz) and 0.014 ± 0.000 (at ε' of 12,935 and 2.2 kHz) when exposed to dry N_2 at 23°C.

Our results suggest that the large discrepancy and variations of dielectric properties in the reported literature for CCTO materials cannot be solely due to its sensitivity to processing conditions but also due to its large sensitivity to testing atmosphere.

Therefore, to simplify the understanding of the dielectric behavior of CCTO for capacitor applications, sample preparation conditions as well as sample storing and measuring atmospheres need to be carefully controlled.

9.3 Thickness Dependent Dielectric Properties

CCTO phase pure calcined powders were prepared at 850°C for 6 h and sintered at 1080°C for 5 h using a simple solid-state reaction in air. Dense ceramics (91%) with a duplex microstructure were obtained with the average grain size of ~5 μm. The presence of relatively stoichiometric grains and grain boundaries (GBs) of the as-prepared surface while slightly reduced oxygen in the sample interior were confirmed by EDS. Slight reduction in oxygen may be due to the existence of oxygen vacancies in the sample interior during sintering at high temperature. Electrical properties of as-prepared and thinned samples (prepared by layer by layer removal and by fine grinding) until 29-35% of the initials thickness were studied by measuring the complex impedance from 23°C to 225°C while exposing the samples to air and dry N_2 atmospheres.

No sample electrode contacts or surface barrier layers were observed. An extremely high low-frequency high dielectric constant due to space charge polarization at GBs was suppressed by changing the measuring atmosphere from air to dry N_2. Impedance measured in controlled dry N_2 atmosphere showed that the thickness dependence of dielectric property was largely affected by GBs, microstructure and defects. Results indicated that GBs were sensitive to the surrounding atmosphere and therefore, electrical properties of GBs can be modified due to adsorbed moisture/air as further concluded from the following.

- An irreproducible low frequency impedance measured at 23°C in air was eliminated when the same samples were measured in N_2 despite the thickness variations. Subsequent measurements in N_2 showed no significant changes to the dielectric properties indicating the stability of measurements.
- Stable total impedance when exposed to N_2 atmosphere indicated the role of air/moisture on dielectric properties at 23°C in CCTO sample despite the thickness variations.
- A decreased dielectric loss at frequencies <1 MHz was seen upon changing the measuring atmosphere from air to N_2 despite their thickness variations.
- Impedance and dielectric measurements in dry N_2 showed that barrier layer capacitance was associated with GBs, which were dominating the electrical properties of CCTO.
- Relatively closer values of resistivity, dielectric constant, and loss tangent at low and high frequencies in dry N_2 as a function of sample thickness suggested negligible changes to electrical properties were not related to sample surface layer affect.
- Improved minimum tan δ values were obtained for as prepared sample, which was 0.010 ± 0.001 at ε′ of 9,663 ± 4 and 1.4 kHz. While the thinned down sample showed slightly larger minimum value of 0.015 ± 0.000 at ε′ of 9,352 ± 5 and 4.5 kHz.

We believe that this research provided comprehensive guidance to eliminate irreproducible dielectric properties measured at low frequencies in CCTO and dielectric loss data measured in ambient to further develop CCTO for future capacitor applications.

9.4 Effect of Alumina Doping

Pure and alumina doped CCTO/xAl_2O_3 (x=0, 0.5, and 4 wt.%) ceramic powders were synthesized by solid-state method at relatively low calcination temperatures of 850°C for 6 h. Dense pure and doped samples with the major phase of $CaCu_3Ti_4O_{12}$ and containing minor secondary phases of $CaTiO_3$, $CuAl_2O_4$, and $CaTiO_3$ were obtained by incorporating 0.5-4wt.% alumina and sintering at 1080°C (S1080) and 1100°C (S1100) for 5 h. The average grain size of CCTO ceramics increased from 5 μm (pure CCTO) to 8 μm (4wt% Al_2O_3) when increasing the alumina content for S1080 while no significant change in the average grain size was observed for sample S1100. The effect of processing conditions such as sintering temperature, phase purity, grain size, and testing atmosphere on the electrical properties of as-prepared pure and alumina doped samples S1080 and S1100 were studied by measuring the complex impedance from 23°C to 225°C while exposing the samples to air and dry N_2 atmospheres. Testing in air lead to irreproducible behavior of impedance and dielectric properties at 23°C due to moisture/air effect as further summarized next.

- Complex impedance analysis showed that resistance of grains (Rg) was slightly increased by the alumina doping while resistance of grain boundaries (GBs) (Rgb) was increased by approximately two orders of magnitude from 13 MΩ (undoped) to 170 MΩ (0.5wt.%) and 440 MΩ (4wt.%) for S1100. While Rgb of S1080 changed by approximately an order of magnitude from 42 MΩ (undoped) to 180 MΩ (0.5wt.%) and 190 MΩ (4wt.%) for doped samples.

- Grain boundary capacitance GBs of S1100 was decreased progressively form 5 nF (undoped) to 2 nF (4wt.%) while for the sample S1080 it increased from 4 nF (undoped) to ~5-9 nF (4wt.%).
- Both samples S1100 and S1080 clearly showed that activation energy of GBs (Egb) was increased (~0.6 for pure and 0.8 for 4wt.% Al_2O_3) when increasing the alumina content. However, activation energy of grains (Eg) is only slightly changed for alumina-doped samples compared to the undoped samples.
- Reduction of low frequency ε' and dielectric loss were seen in alumina doped samples and the improvement of the dielectric loss was mainly attributed to the increase in the DC resistance of the GBs (Rgb).
- Higher the measuring temperature (>23°C), larger was the dielectric loss and smaller was the total impedance for both S1080 and S1100.
- Loss factor verses frequency showed two sets of losses attributed to dielectric relaxation and ohmic conduction.
- The values of minimum dielectric loss were lower than the reported values for alumina doped CCTO due to the moisture/air free atmosphere.
- The lowest tan δ of 0.010 ± 0.001 with ε' of 9663 ± 4 at 1.4 kHz and 23°C in N_2 was measured for pure S1080. While the lowest tan δ for the pure S1100 was 0.014 with ε' of 12935 at 2.2 kHz in N_2 at 23°C.
- Minima values of tan δ 0.021 and 0.020, respectively, for samples S1080 and S1100 were measured with relatively large ε' of 8,815-11,090 at 23°C at much lower frequencies of 500-800 Hz for 0.5wt.% Al_2O_3 in CCTO.

- Dissipation loss and loss tangent were decreased at low frequencies (<100 Hz) as the alumina content was increased from 0.5-4wt.% indicating the possibility to develop the alumina doped CCTO materials for practical applications as capacitors.

CHAPTER X

RESEARCH PUBLICATIONS

1) Disna P. Samarakoon and Raj N. Singh, "Influence of Alumina Dopant and Environment on the Electrical Properties of Calcium Copper Titanate Ceramics," paper submitted to Journal of Materials Science and Engineering B (June 27, 2019).
2) Disna P. Samarakoon and Raj N. Singh, "Thickness dependent dielectric properties of calcium copper titanate ceramics measured in a controlled atmosphere", *Ceramics International*, 45, 2019 , pp. 16554–16563. https://doi.org/10.1016/j.ceramint.2019.05.192.
3) Disna P. Samarakoon, Nirmal Govindaraju, and Raj N. Singh, "Influence of Atmospheres on the Dielectric Properties of Calcium Copper Titanate Ceramics", *Journal of the American Ceramic Society*, 102, 2019, pp. 5271– 5283. https://doi.org/10.1111/jace.16381.
4) Disna P. Samarakoon, Nirmal Govindaraju, and Raj N. Singh, "Dielectric Properties of Calcium Copper Titanate Ceramics Exposed to Air and Dry Nitrogen Atmospheres", *Transactions of the Indian Institute of Metals*, 2019, 0975-1645 (online) pp. 1–7, https://doi.org/10.1007/s12666-018-1551-1.

5) Disna P. Samarakoon, Nirmal Govindaraju, and Raj N. Singh, "Effect of Atmosphere on Dielectric Properties of Calcium Copper Titanate Ceramics", *paper presented in Materials Science & Technology 2018,* October 14 –18: Materials Science & Technology, Columbus, Ohio, USA.
6) Disna P. Samarakoon, Nirmal Govindaraju, and Raj N. Singh, "Influence of Processing and Microstructure on Dielectric Properties of Calcium Copper Titanate Ceramics", *Processing, Properties, and Design of Advanced Ceramics and Composites II, Cearmics Transactions,* 261, 2017, pp. 237–243.
7) Disna P. Samarakoon, Nirmal Govindaraju, and Raj N. Singh. "Calcium Copper Titanate Based High Dielectric Constant Materials for Energy Storage Applications," *Processing, Properties, and Design of Advanced Ceramics and Composites. Cearmics Transactions,* 259, 2016, pp. 131–140.

CHAPTER XI

SUGGESTIONS FOR FUTURE WORK

The current research work so far has been focusing on finding out stable measuring atmosphere for pure and doped alumina doped CCTO ceramics and validating the results. I believe that this research can provide comprehensive guidance to develop CCTO for future capacitor applications. However, still more experiments need to be carried out as per the following recommendations. It is hoped that these results and future research will provide an enhanced understanding of dielectric properties of CCTO for capacitor and in energy storage applications.

- Implementing the current methods and repeating this study on the effect of microstructure and other testing atmosphere, such as dry air and pure dry O_2 would deepen the understanding of charge carrier transport mechanisms in CCTO. This way, more information will be obtained on the differences in two types of dielectric relaxations observed in the current CCTO samples despite the testing atmosphere, microstructure, sample thickness, temperature or alumina doping.

- In order to confirm the barrier layers at GBs and identify the important roles of GBs more experiments such as two probe impedance measurements using microelectrodes between grains are suggested.
- Further optimization of the sintering conditions to achieve higher density >95% are suggested to study and understand the important effect of measuring atmosphere for the pure and doped CCTO ceramics. Thus, it would be very interesting to prepare dense CCTO ceramics and study the dielectric properties in air as a function of temperature.
- Inspired by the reduction of the low tan δ and large Rgb by Al_2O_3 doping in CCTO, more doping experiments with various alumina content are suggested to be able to see the optimum doping levels for further enhancing dielectric properties.

REFERENCES

[1] R. Jia, X. Zhao, J. Li, and X. Tang, “Colossal breakdown electric field and dielectric response of Al-doped $CaCu_3Ti_4O_{12}$ ceramics,” Materials Science and Engineering: B, vol. 185, pp. 79-85, 2014.

[2] Y. Bai, Z.-Y. Cheng, V. Bharti, H. S. Xu, and Q. M. Zhang, “High-dielectric-constant ceramic-powder polymer composites,” Applied Physics Letters, vol. 76, no. 25, pp. 3804-3806, 2000.

[3] S. Krohns, P. Lunkenheimer, S. Meissner, A. Reller, B. Gleich, A. Rathgeber, T. Gaugler, H. U. Buhl, D. C. Sinclair, and A. Loidl, “The route to resource-efficient novel materials,” Nature Materials, vol. 10, pp. 899, 2011.

[4] R. K. Pandey, W. A. Stapleton, J. Tate, A. K. Bandyopadhyay, I. Sutanto, S. Sprissler, and S. Lin., “Applications of CCTO supercapacitor in energy storage and electronics,” AIP Advances, vol. 3, no. 6, pp. 062126, 2013.

[5] R. Schmidt, and D. C. Sinclair, "$CaCu_3Ti_4O_{12}$ (CCTO) ceramics for capacitor applications," Capacitors: theory of operation,behavior and safety regulations. , K. N. Muller, ed.: Nova Science Publishers Inc., 2013.

[6] C. C. Homes, T. Vogt, S. M. Shapiro, W. Si, S. Wakimoto, and M. A. Subramanian, “Charge transfer in the high dielectric constant materials $CaCu_3Ti_4O_{12}$ and CdCu3Ti4O12,” Physical Review B, vol. 67, pp. 092106, 2003.

[7] M. A. Subramanian, D. Li, N. Duan, B. A. Reisner, and A. W. Sleight, “High dielectric constant in $ACu_3Ti_4O_{12}$ and $ACu_3Ti_3FeO_{12}$ phases,” Journal of Solid-State Chemistry, vol. 151, no. 2, pp. 323-325, 2000.

[8] T. B. Adams, D. C. Sinclair, and A. R. West, “Giant barrier layer capacitance effects in $CaCu_3Ti_4O_{12}$ ceramics,” Advanced Materials, vol. 14, no. 18, pp. 1321-1323, 2002.

[9] D. C. Sinclair, T. B. Adams, F. D. Morrison, and A. R. West, “$CaCu_3Ti_4O_{12}$: One-step internal barrier layer capacitor,” Applied Physics Letters, vol. 80, no. 12, pp. 2153-2155, 2002.

[10] Y. Li, P. Liang, X. Chao, and Z. Yang, “Preparation of $CaCu_3Ti_4O_{12}$ ceramics with low dielectric loss and giant dielectric constant by the sol–gel technique,” Ceramics International, vol. 39, no. 7, pp. 7879-7889, 2013.

[11] L. Singh, U. S. Rai, K. D. Mandal, and N. B. Singh, “Progress in the growth of $CaCu_3Ti_4O_{12}$ and related functional dielectric perovskites,” Progress in Crystal Growth and Characterization of Materials, vol. 60, no. 2, pp. 15-62, 2014.

[12] T. Li, Z. Chen, F. Chang, J. Hao, and J. Zhang, “The effect of Eu_2O_3 doping on $CaCu_3Ti_4O_{12}$ varistor properties,” Journal of Alloys and Compounds, vol. 484, no. 1-2, pp. 718-722, 2009.

[13] B. Cheng, Y.-H. Lin, W. Deng, J. Cai, J. Lan, C.-W. Nan, X. Xiao, and J. He, “Dielectric and nonlinear electrical behaviors of Ce-doped $CaCu_3Ti_4O_{12}$ ceramics,” Journal of electro-ceramics, vol. 29, no. 4, pp. 250-253, 2012.

[14] R. Schmidt, M. C. Stennett, N. C. Hyatt, J. Pokorny, J. Prado-Gonjal, M. Li, and D. C. Sinclair, “Effects of sintering temperature on the internal barrier layer capacitor (IBLC) structure in $CaCu_3Ti_4O_{12}$ (CCTO) ceramics,” Journal of the European Ceramic Society, vol. 32, no. 12, pp. 3313-3323, 2012.

[15] A. A. Felix, M. O. Orlandi, and J. A. Varela, “Schottky-type grain boundaries in CCTO ceramics,” Solid State Communications, vol. 151, no. 19, pp. 1377-1381, 2011.

[16] J.-W. Lee, and J.-H. Koh, “Grain size effects on the dielectric properties of CaCu3Ti4O12 ceramics for supercapacitor applications,” Ceramics International, vol. 41, no. 9, Part A, pp. 10442-10447, 2015.

[17] T.-T. Fang, and C. P. Liu, “Evidence of the internal domains for inducing the anomalously high dielectric constant of $CaCu_3Ti_4O_{12}$,” Chemistry of Materials, vol. 17, no. 20, pp. 5167-5171, 2005.

[18] J. Li, M. A. Subramanian, H. D. Rosenfeld, C. Y. Jones, B. H. Toby, and A. W. Sleight, “Clues to the giant dielectric constant of $CaCu_3Ti_4O_{12}$ in the defect structure of SrCu3Ti4O12,” Chemistry of Materials, vol. 16, no. 25, pp. 5223-5225, 2004.

[19] P. Lunkenheimer, R. Fichtl, S. G. Ebbinghaus, and A. Loidl, “Non-intrinsic origin of the colossal dielectric constants in $CaCu_3Ti_4O_{12}$,” Physical Review B, vol. 70, no. 17, pp. 172102, 2004.

[20] C. C. Wang, and L. W. Zhang, “Surface-layer effect in $CaCu_3Ti_4O_{12}$,” Applied Physics Letters, vol. 88, no. 4, pp. 042906, 2006.

[21] S. Krohns, P. Lunkenheimer, S. G. Ebbinghaus, and A. Loidl, “Colossal dielectric constants in single-crystalline and ceramic $CaCu_3Ti_4O_{12}$ investigated by broadband dielectric spectroscopy,” Journal of Applied Physics, vol. 103, no. 8, pp. 084107, 2008.

[22] S. Krohns, P. Lunkenheimer, S. Ebbinghaus, and A. Loidl, “Broadband dielectric spectroscopy on single-crystalline and ceramic $CaCu_3Ti_4O_{12}$,” J Applied physics letters, vol. 91, no. 2, pp. 022910, 2007.

[23] M. Li, Z. Shen, M. Nygren, A. Feteira, D. C. Sinclair, and A. R. West, “Origin(s) of the apparent high permittivity in $CaCu_3Ti_4O_{12}$ ceramics: clarification on the contributions from internal barrier layer capacitor and sample-electrode contact effects,” Journal of Applied Physics vol. 106, no. 10, pp. 104106, 2009.

[24] T. B. Adams, D. C. Sinclair, and A. R. West, “Influence of processing conditions on the electrical properties of $CaCu_3Ti_4O_{12}$ ceramics,” Journal of American Ceramic Society, vol. 89, no. 10, pp. 3129-3135, 2006.

[25] Z. Guozhong, Z. Jialiang, Z. Peng, W. Jinfeng, and W. Chunlei, “Grain boundary effect on the dielectric properties of $CaCu_3Ti_4O_{12}$ ceramics,” Journal of Physics D: Applied Physics, vol. 38, no. 11, pp. 1824, 2005.

[26] H. Yu, H. Liu, H. Hao, L. Guo, C. Jin, Z. Yu, and M. Cao, “Grain size dependence of relaxor behavior in $CaCu_3Ti_4O_{12}$ ceramics,” Applied Physics Letters, vol. 91, no. 22, pp. 222911, 2007.

[27] Y.-H. Lin, J. Cai, M. Li, C.-W. Nan, and J. He, “Grain boundary behavior in varistor-capacitor TiO_2-rich $CaCu_3Ti_4O_{12}$ ceramics,” Journal of Applied Physics, vol. 103, no. 7, pp. 074111, 2008.

[28] T. B. Adams, B. Timothy, D. C. Sinclair, and A. R. West, “Characterization of grain boundary impedances in fine and coarse grained $CaCu_3Ti_4O_{12}$ ceramics,” Physical Review B, vol. 73, no. 9, pp. 094124, 2006.

[29] C. C. Homes, T. Vogt, S. M. Shapiro, S. Wakimoto, and A. P. Ramirez, “Optical response of high-dielectric-constant perovskite-related oxide,” Science, vol. 293, no. 5530, pp. 673, 2001.

[30] S. Kwon, and D. P. Cann, “Influence of the processing rates and sintering temperatures on the dielectric properties of $CaCu_3Ti_4O_{12}$ ceramics,” Journal of Electroceramics, vol. 24, no. 3, pp. 231-236, 2010.

[31] L. Ni, X. M. Chen, X. Q. Liu, and R. Z. Hou, “Microstructure dependent giant dielectric response in $CaCu_3Ti_4O_{12}$ ceramics,” Solid State Communications, vol. 139, no. 2, pp. 45-50, 2006.

[32] R. Yu, H. Xue, Z. Cao, L. Chen, and Z. Xiong, “Effect of oxygen sintering atmosphere on the electrical behavior of CCTO ceramics,” Journal of the European Ceramic Society, vol. 32, no. 6, pp. 1245-1249, 2012.

[33] S. Kwon, C.-C. Huang, M. A. Subramanian, and D. P. Cann, “Effects of cation stoichiometry on the dielectric properties of $CaCu_3Ti_4O_{12}$,” Journal of Alloys and Compounds, vol. 473, no. 1, pp. 433-436, 2009.

[34] S. Marković, M. Lukić, Č. Jovalekić, S. D. Škapin, D. Suvorov, and D. Uskoković, “Sintering Effects on Dielectric Properties of Zn-Doped $CaCu_3Ti_4O_{12}$ Ceramic Synthesized by Modified Sol-Gel Route.,” Electronic Materials Letters, vol. 9 no. 1, pp. 107-113, 2013.

[35] W.-X. Yuan, Z. Luo, and C. Wang, “Investigation on effects of CuO secondary phase on dielectric properties of $CaCu_3Ti_4O_{12}$ ceramics,” Journal of Alloys and Compounds, vol. 562, pp. 1-4, 2013.

[36] B. S. Prakash, and K. B. R. Varma, “The influence of the segregation of Cu-rich phase on the microstructural and impedance characteristics of $CaCu_3Ti_4O_{12}$ ceramics,” Journal of Materials Science, vol. 42, no. 17, pp. 7467-7477, 2007.

[37] F. Tsang-Tse, and M. Li-Then, “Evidence of Cu deficiency: A key point for the understanding of the mystery of the giant dielectric constant in $CaCu_3Ti_4O_{12}$,” Journal of the American Ceramic Society, vol. 90, no. 2, pp. 638-640, 2007.

[38] B. S. Prakash, and K. B. R. Varma, “Influence of sintering conditions and doping on the dielectric relaxation originating from the surface layer effects in $CaCu_3Ti_4O_{12}$ ceramics,” Journal of Physics and Chemistry of Solids, vol. 68, no. 4, pp. 490-502, 2007.

[39] F. Tsang-Tse, and S. Hsu-Kai, “Mechanism for developing the boundary barrier layers of $CaCu_3Ti_4O_{12}$,” Journal of the American Ceramic Society, vol. 87, no. 11, pp. 2072-2079, 2004.

[40] Y. He, H. Zhang, P. Liu, J. Zhou, and C. Mu, “Oxygen-defects-related dielectric response in $CaCu_3Ti_4O_{12}$ ceramics,” Physica B: Condensed Matter, vol. 404, no. 20, pp. 3722-3726, 2009.

[41] S.-W. Choi, S.-H. Hong, and Y.-M. Kim, “Effect of Al doping on the electric and dielectric properties of $CaCu_3Ti_4O_{12}$,” Journal of the American Ceramic Society, vol. 90, no. 12, pp. 4009-4011, 2007.

[42] S. Li, H. Wang, C. Lin, Y. Yang, and J. Li, “Dielectric properites of Al-doped $CaCu_3Ti_4O_{12}$ ceramics by coprecipitation method,” in Proceedings of 2011 International Symposium on Electrical Insulating Materials, 2011, pp. 23-26.

[43] C. Puchmark, and G. Rujijanagul, “Improvement in dielectric and mechanical performance of $CaCu_{(3.1)}Ti_4O_{(12.1)}$ by addition of Al_2O_3 nanoparticles,” Nanoscale Research Letters, vol. 7, no. 1, pp. 68-68, 2012.

[44] L. Liu, Y. Huang, Y. Li, D. Shi, S. Zheng, S. Wu, L. Fang, and C. Hu, “Dielectric and non-ohmic properties of $CaCu_3Ti_4O_{12}$ ceramics modified with NiO, SnO_2, SiO_2, and Al_2O_3 additives,” Journal of Materials Science, vol. 47, no. 5, pp. 2294-2299, 2012.

[45] A. Rajabtabar-Darvishi, R. Bayati, O. Sheikhnejad-Bishe, L. D. Wang, W. L. Li, J. Sheng, and W. D. Fei, “Giant dielectric response and low dielectric loss in Al_2O_3 grafted $CaCu_3Ti_4O_{12}$ ceramics,” Journal of Applied Physics, vol. 117, no. 9, pp. 094103, 2015.

[46] R. Jia, X. Tang, J. Li, and X. Zhao, “Large breakdown field and dielectric performance of $CaCu_3Ti_4O_{12}$ ceramics modified by Al_2O_3,” 2013 IEEE International Conference on Solid Dielectrics (ICSD), pp. 1087-1090, 2013.

[47] J. Li, L. Hou, R. Jia, L. Gao, K. Wu, and S. Li, “Influences of $CuAl_2O_4$ doping on the dielectric properties of $CaCu_3Ti_4O_{12}$ ceramics,” Journal of Materials Science: Materials in Electronics, vol. 26, no. 7, pp. 5085-5091, 2015.

[48] Z. Tang, K. Wu, Y. Huang, and J. Li, “High breakdown field $CaCu_3Ti_4O_{12}$ ceramics: Roles of the secondary phase and of Sr doping,” Energies, vol. 10, pp. 1031, 2017.

[49] S. Kwon, and D. P. Cann, “Influence of the processing rates and sintering temperatures on the dielectric properties of $CaCu_3Ti_4O_{12}$ ceramics,” J Journal of electroceramics, vol. 24, no. 3, pp. 231-236, 2010.

[50] J. Boonlakhorn, and P. Thongbai, “Effect of annealing in O_2 and mechanisms contributing to the overall loss tangent of $CaCu_3Ti_4O_{12}$ ceramics,” Journal of Electronic Materials, vol. 44, no. 10, pp. 3687-3695, 2015.

[51] T. Li, H. F. He, T. Zhang, B. Zhao, Z. Q. Chen, H. Y. Dai, R. Z. Xue, and Z. P. Chen, “Effect of synthesizing temperatures on the microstructure and electrical property of $CaCu_3Ti_4O_{12}$ ceramics prepared by sol-gel process,” Journal of Alloys and Compounds, vol. 684, pp. 315-321, 2016.

[52] B. Bender, and M.-J. Pan, “The effect of processing on the giant dielectric properties of $CaCu_3Ti_4O_{12}$,” J Materials Science Engineering: B, vol. 117, no. 3, pp. 339-347, 2005.

[53] P. Leret, M. A. de la Rubia, F. Rubio‐Marcos, J. J. Romero, and J. F. Fernández, “Effect of processing on the sintering of high dielectric constant $CaCu_3Ti_4O_{12}$ ceramics,” International Journal of Applied Ceramic Technology, vol. 8, no. 5, pp. 1201-1207, 2011.

[54] M. A. de la Rubia, P. Leret, J. de Frutos, and J. F. Fernández, “Effect of the Synthesis Route on the Microstructure and the Dielectric Behavior of $CaCu_3Ti_4O_{12}$ Ceramics,” Journal of the American Ceramic Society, vol. 95, no. 6, pp. 1866-1870, 2012.

[55] M. Li, X. Chen, D. Zhang, W. Wang, and W. Wang, “Humidity sensitive properties of pure and Mg-doped $CaCu_3Ti_4O_{12}$,” J Sensors Actuators B: Chemical, vol. 147, no. 2, pp. 447-452, 2010.

[56] M. Li, “Study of the humidity-sensing mechanism of $CaCu_3Ti_4O_{12}$,” J Sensors Actuators B: Chemical, vol. 228, pp. 443-447, 2016.

[57] M. Ahmadipour, M. F. Ain, and Z. A. Ahmad, “Effect of thickness on humidity sensing properties of RF magnetron sputtered $CaCu_3Ti_4O_{12}$ thin films on alumina substrate,” IEEE Sensors Journal, vol. 17, no. 11, pp. 3224-3230, 2017.

[58] M. Ahmadipour, M. F. Ain, and Z. A. Ahmad, “Fabrication of resistance type humidity sensor based on $CaCu_3Ti_4O_{12}$ thick film,” Measurement, vol. 94, pp. 902-908, 2016.

[59] D. Ming, J. M. Reau, J. Ravez, J. Gitae, and P. Hagenmuller, “Impedance spectroscopy analysis of a $LiTaO_3$ type single crystal,” Journal of Solid-State Chemistry, vol. 116, no. 1, pp. 185-192, 1995.

[60] K. C. Kao, Dielectric phenomena in solids: Elsevier, 2004.

[61] S. Kasap, Principles of Electronic Materials and Devices: McGraw-Hill, Inc., 2006.

[62] K. S. Cole, and R. H. Cole, “Dispersion and Absorption in Dielectrics I. Alternating Current Characteristics,” vol. 9, no. 4, pp. 341-351, 1941.

[63] G. G. Raju, Dielectrics in electric fields: Taylor & Francis, 2003.

[64] A. K. Jonscher, “Dielectric relaxation in solids,” Journal of Physics D: Applied Physics, vol. 32, no. 14, pp. R57, 1999.

[65] A. E. Smith, T. G. Calvarese, A. W. Sleight, and M. A. Subramanian, “An anion substitution route to low loss colossal dielectric $CaCu_3Ti_4O_{12}$,” Journal of Solid-State Chemistry, vol. 182, no. 2, pp. 409-411, 2009.

[66] L. He, J. B. Neaton, M. H. Cohen, D. Vanderbilt, and C. C. Homes, “First principles study of the structure and lattice dielectric response of $CaCu_3Ti_4O_{12}$,” Physical Review B, vol. 65, no. 21, pp. 214112, 2002.

[67] L. He, J. B. Neaton, D. Vanderbilt, and M. H. Cohen, “Lattice dielectric response of $CdCu_3Ti_4O_{12}$ and $CaCu_3Ti_4O_{12}$ from first principles,” Physical Review B vol. 67, pp. 012103, 2003.

[68] M. H. Whangbo, and M. A. Subramanian, “Structural model of planar defects in $CaCu_3Ti_4O_{12}$ exhibiting a giant dielectric constant,” Chemistry of Materials, vol. 18, no. 14, pp. 3257-3260, 2006.

[69] S. Krohns, P. Lunkenheimer, S. G. Ebbinghaus, and A. Loidl, “Broadband dielectric spectroscopy on single-crystalline and ceramic $CaCu_3Ti_4O_{12}$,” Applied Physics Letters, vol. 91, no. 2, pp. 022910, 2007.

[70] H. E. Kim, S.-D. Yang, J.-W. Lee, H. M. Park, and S.-I. Yoo, “Growth and characterization of $CaCu_3Ti_4O_{12}$ single crystals,” Journal of Crystal Growth, vol. 408, pp. 60-63, 2014.

[71] C. Wang, and L. Zhang, “Polaron relaxation related to localized charge carriers in $CaCu_3Ti_4O_{12}$,” Applied physics letters, vol. 90, no. 14, pp. 142905, 2007.

[72] N. Lei, and C. X. Ming, “Enhancement of giant dielectric response in $CaCu_3Ti_4O_{12}$ ceramics by Zn substitution,” Journal of the American Ceramic Society, vol. 93, no. 1, pp. 184-189, 2010.

[73] L. Ni, and X. M. Chen, “Dielectric relaxations and formation mechanism of giant dielectric constant step in $CaCu_3Ti_4O_{12}$ ceramics,” Applied Physics Letters, vol. 91, no. 12, pp. 122905, 2007.

[74] G. Deng, and P. Muralt, “Annealing effects on electrical properties and defects of $CaCu_3Ti_4O_{12}$ thin films deposited by pulsed laser deposition,” Physical Review B vol. 81, pp. 224111, 2010.

[75] X. Luo, Y. Liu, C. Yang, S. Chen, S. Tang, and K. Bärner, “Oxygen vacancy related defect dipoles in $CaCu_3Ti_4O_{12}$: Detected by electron paramagnetic resonance spectroscopy,” Journal of the European Ceramic Society, vol. 35, no. 7, pp. 2073-2081, 2015.

[76] R. Schmidt, S. Pandey, P. Fiorenza, and D. Sinclair, “Non-stoichiometry in $CaCu_3Ti_4O_{12}$ ceramics,” RSC Advances, vol. 3, pp. 14580, 2013.

[77] S.-Y. Chung, S.-I. Lee, J.-H. Choi, and S.-Y. Choi, “Initial cation stoichiometry and current-voltage behavior in Sc-doped calcium copper titanate,” Applied Physics Letters, vol. 89, pp. 191907-191907, 2006.

[78] T.-T. Fang, L.-T. Mei, and H.-F. Ho, “Effects of Cu stoichiometry on the microstructures, barrier-layer structures, electrical conduction, dielectric responses, and stability of $CaCu_3Ti_4O_{12}$,” Acta Materialia, vol. 54, no. 10, pp. 2867-2875, 2006.

[79] Y. Wenxiang, “Investigation on the decomposable process and the secondary liquid phase effect on the dielectric properties of $CaCu_3Ti_4O_{12}$ ceramics,” Journal of Physics D: Applied Physics, vol. 42, no. 17, pp. 175401, 2009.

[80] L. Zhang, and Z.-J. Tang, “Polaron relaxation and variable-range-hopping conductivity in the giant-dielectric-constant material $CaCu_3Ti_4O_{12}$,” Physical Review B, vol. 70, no. 17, pp. 174306, 2004.

[81] C. Wang, and L. Zhang, “Oxygen vacancy related dielectric anomaly in CaCu3Ti4O12: post sintering annealing studies,” Physical Review B, vol. 74, no. 2, pp. 024106, 2006.

[82] J. L. Zhang, P. Zheng, C. L. Wang, M. L. Zhao, J. C. Li, and J. F. Wang, “Dielectric Dispersion of $CaCu_3Ti_4O_{12}$ Ceramics at High Temperatures,” Applied Physics Letters, vol. 87, no. 14, pp. 142901, 2005.

[83] S. Vangchangyia, E. Swatsitang, P. Thongbai, S. Pinitsoontorn, T. Yamwong, S. Maensiri, V. Amornkitbamrung, and P. Chindaprasirt, “Very low loss tangent and high dielectric permittivity in pure- $CaCu_3Ti_4O_{12}$ ceramics prepared by a modified sol-gel process,” Journal of the American Ceramic Society, vol. 95, no. 5, pp. 1497-1500, 2012.

[84] J. Liu, R. W. Smith, and W.-N. Mei, “Synthesis of the giant dielectric constant material $CaCu_3Ti_4O_{12}$ by wet-chemistry methods,” Chemistry of Materials, vol. 19, no. 24, pp. 6020-6024, 2007.

[85] L. Singh, I. W. Kim, W. S. Woo, B. C. Sin, H.-i. Lee, and Y. Lee, “A novel low cost non-aqueous chemical route for giant dielectric constant $CaCu_3Ti_4O_{12}$ ceramic,” Solid State Sciences, vol. 43, pp. 35-45, 2015.

[86] J. Zhao, J. Liu, and G. Ma, “Preparation, characterization and dielectric properties of CaCu3Ti4O12 ceramics,” Ceramics International, vol. 38, no. 2, pp. 1221-1225, 2012.

[87] S. De Almeida-Didry, C. Autret, A. Lucas, C. Honstettre, F. Pacreau, and F. Gervais, “Leading role of grain boundaries in colossal permittivity of doped and undoped CCTO,” Journal of the European Ceramic Society, vol. 34, no. 15, pp. 3649-3654, 2014.

[88] L. Sun, Z. Wang, Y. Shi, E. Cao, Y. Zhang, H. Peng, and L. Ju, “Sol–gel synthesized pure $CaCu_3Ti_4O_{12}$ with very low dielectric loss and high dielectric constant,” Ceramics International, vol. 41, no. 10 Part A, pp. 13486-13492, 2015.

[89] P. Kumar Patel, and K. L. Yadav, “Dwell time effect on the barrier layer capacitor structure in $CaCu_3Ti_4O_{12}$ ceramic,” Ceramics International Part B, vol. 41, no. 9, pp. 12386-12392, 2015.

[90] R. Löhnert, H. Bartsch, R. Schmidt, B. Capraro, and J. Töpfer, “Microstructure and electric properties of $CaCu_3Ti_4O_{12}$ multilayer capacitors,” Journal of the American Ceramic Society, vol. 98, no. 1, pp. 141-147, 2015.

[91] A. Wen, D. Yuan, X. Zhu, J. Zhu, D. Xiao, and J. Zhu, “Electrical and dielectric properties of aluminum/niobium co-doped $CaCu_3Ti_4O_{12}$ ceramics,” Ferroelectrics, vol. 492, no. 1, pp. 1-9, 2016.

[92] M Sahu, R N P Choudhary, and B. K. Roul, “Dielectric and electrical characteristics of Sr modified $Ca_1Cu_3Ti_4O_{12}$,” AIP Conference Proceedings, vol. 1953, no. 1, pp. 050015, 2018.

[93] T.-T. Fang, and L.-T. Mei, “Evidence of Cu deficiency: A key point for the understanding of the mystery of the giant dielectric constant in CaCu3Ti4O12,” Journal of the American Ceramic Society, vol. 90, no. 2, pp. 638-640, 2007.

[94] J. Li, R. Jia, L. Hou, L. Gao, K. Wu, and S. Li, “The dimensional effect of dielectric performance in $CaCu_3Ti_4O_{12}$ ceramics: Role of grain boundary,” Journal of Alloys and Compounds, vol. 644, pp. 824-829, 2015.

[95] R. Aoyagi, M. Iwata, and M. Maeda, “Effect of sintering temperature on the dielectric properties of $CaCu_3Ti_4O_{12}$ ceramics,” Ferroelectrics, vol. 356, no. 1, pp. 90-94, 2007.

[96] J. J. Romero, P. Leret, F. Rubio-Marcos, A. Quesada, and J. F. Fernández, “Evolution of the intergranular phase during sintering of $CaCu_3Ti_4O_{12}$ ceramics,” Journal of the European Ceramic Society, vol. 30, no. 3, pp. 737-742, 2010.

[97] T. B. Adams, D. C. Sinclair, and A. R. West, “Influence of processing conditions on the electrical properties of $CaCu_3Ti_4O_{12}$ ceramics,” Journal of the American Ceramic Society, vol. 89, no. 10, pp. 3129-3135, 2006.

[98] A. R. West, T. B. Adams, F. D. Morrison, and D. C. Sinclair, “Novel high capacitance materials:- $BaTiO_3$:La and $CaCu_3Ti_4O_{12}$,” Journal of the European Ceramic Society, vol. 24, no. 6, pp. 1439-1448, 2004.

[99] S. D. Hutagalung, O. L. Ying, and Z. A. Ahmad, “Effect of sintering temperature on the properties of modified mechanical alloyed $CaCu_3Ti_4O_{12}$,” IEEE Transactions on Ultrasonics, Ferroelectrics, and Frequency Control, vol. 54, no. 12, pp. 2587-2591, 2007.

[100] Q. Zheng, H. Fan, and C. Long, “Microstructures and electrical responses of pand chromium-doped $CaCu_3Ti_4O_{12}$ ceramics,” Journal of Alloys and Compounds vol. 511, pp. 90–94, 2012.

[101] C. Mu, H. Zhang, Y. He, and P. Liu, “Influence of temperature on dielectric properties of Fe-doped $CaCu_3Ti_4O_{12}$ ceramics,” Physica B vol. 405, pp. 386-389, 2010.

[102] X. H. Zheng, C. Zhang, B. L. Liang, D. P. Tang, X. Huang, and X. L. Liu, “An effective way to tune the microstructure and dielectric properties of $CaCu_3Ti_4O_{12}$ ceramics,” Journal of Alloys and Compounds, vol. 505, no. 1, pp. L10-L14, 2010.

[103] A. Sen, U. Maiti, R. Thapa, and K. K. Chattopadhyay, “Effect of vanadium doping on the dielectric and nonlinear current–voltage characteristics of $CaCu_3Ti_4O_{12}$ ceramic,” Journal of Alloys and Compounds, vol. 506, pp. 853-857, 2010.

[104] M. A. de la Rubia, P. Leret, A. Del Campo, R. Alonso, A. R. López-Garcia, J. Fernández, and J. De Frutos, “Dielectric behaviour of Hf-doped $CaCu_3Ti_4O_{12}$ ceramics obtained by conventional synthesis and reactive sintering,” Journal of the European Ceramic Society vol. 32, pp. 1691–1699, 2012.

[105] J. Jumpatam, B. Putasaeng, T. Yamwong, P. Thongbai, and S. Maensiri, “Enhancement of giant dielectric response in Ga-doped $CaCu_3Ti_4O_{12}$ ceramics,” Ceramics International, vol. 39, pp. 1057–1064, 2013.

[106] S. Kwon, C.-C. Huang, E. A. Patterson, D. P. Cann, E. F. Alberta, S. Kwon, W. S. Hackenberger, and D. P. Cann, “The effect of Cr_2O_3, Nb_2O_5 and ZrO_2 doping on the dielectric properties of $CaCu_3Ti_4O_{12}$,” Materials Letters, vol. 62, no. 4, pp. 633-636, 2008.

[107] S. Jesurani, K. Samikannu, M. Hashim, I. Ismail, and I. R. Ibrahim, Microstructural and dielectric properties of Zr doped microwave sintered $CaCu_3Ti_4O_{12}$ synthesized by sol-gel route, 2014.

[108] K. Meeporn, T. Yamwong, S. Pinitsoontorn, V. Amornkitbamrung, and P. Thongbai, “Grain size independence of giant dielectric permittivity of $CaCu_3Ti_{4-x}Sc_xO_{12}$ ceramics,” Ceramics International, vol. 40, no. 10, Part A, pp. 15897-15906, 2014.

[109] L. Liu, H. Yanmin, Y. Li, D. Shi, S. Zheng, S. wu, L. Fang, and C. Hu, “Dielectric and non-Ohmic properties of $CaCu_3Ti_4O_{12}$ ceramics modified with NiO, SnO_2, SiO_2, and Al_2O_3 additives,” vol. 47, pp. 2294-2299, 2012.

[110] S. De Almeida-Didry, M. M. Nomel, C. Autret, C. Honstettre, A. Lucas, F. Pacreau, and F. Gervais, “Control of grain boundary in alumina doped CCTO showing colossal permittivity by core-shell approach,” Journal of the European Ceramic Society, vol. 38, no. 9, pp. 3182-3187, 2018.

[111] L. Shengtao, W. Hui, L. Chunjiang, Y. Yang, and L. Jianying, “Dielectric properites of Al-doped $CaCu_3Ti_4O_{12}$ ceramics by coprecipitation method,” Proceedings of 2011 International Symposium on Electrical Insulating Materials, pp. 23-26, 2011.

[112] L. Singh, U. S. Rai, A. K. Rai, and K. D. Mandal, “Sintering effects on dielectric properties of Zn-doped $CaCu_3Ti_4O_{12}$ ceramic synthesized by modified sol-gel route,” Electronic Materials Letters, vol. 9, no. 1, pp. 107-113, 2013.

[113] M. Li, G. Cai, D. F. Zhang, W. Y. Wang, W. J. Wang, and X. L. Chen, “Enhanced dielectric responses in Mg-doped $CaCu_3Ti_4O_{12}$,” vol. 104, no. 7, pp. 074107, 2008.

[114] J. Boonlakhorn, B. Putasaeng, and P. Thongbai, “Origin of significantly enhanced dielectric response and nonlinear electrical behavior in Ni^{2+}-doped $CaCu_3Ti_4O_{12}$: Influence of DC bias on electrical properties of grain boundary and associated giant dielectric properties,” Ceramics International, vol. 45, no. 6, pp. 6944-6949, 2019.

[115] P. Thongbai, B. Putasaeng, T. Yamwong, and S. Maensiri, “Modified giant dielectric properties of samarium doped CaCu3Ti4O12 ceramics,” Materials Research Bulletin, vol. 47, no. 9, pp. 2257-2263, 2012.

[116] S. Vangchangyia, T. Yamwong, E. Swatsitang, P. Thongbai, and S. Maensiri, “Selectivity of doping ions to effectively improve dielectric and non-ohmic properties of $CaCu_3Ti_4O_{12}$ ceramics,” Ceramics International, vol. 39, no. 7, pp. 8133-8139, 2013.

[117] J. Boonlakhorn, P. Thongbai, B. Putasaeng, T. Yamwong, and S. Maensiri, “Very high-performance dielectric properties of $Ca_{1-3x/2}Yb_xCu_3Ti_4O_{12}$ ceramics,” Journal of Alloys and Compounds, vol. 612, pp. 103-109, 2014.

[118] P. Thongbai, J. Boonlakhorn, B. Putasaeng, T. Yamwong, and S. Maensiri, “Extremely Enhanced Nonlinear Current–Voltage Properties of Tb-Doped $CaCu_3Ti_4O_{12}$ Ceramics,” vol. 96, no. 2, pp. 379-381, 2013.

[119] J. Jumpatam, B. Putasaeng, T. Yamwong, P. Thongbai, and S. Maensiri, “A Novel Route to Greatly Enhanced Dielectric Permittivity with Reduce Loss Tangent in $CaCu_{3-x}Zn_xTi_4O_{12}/CaTiO_3$ Composites,” vol. 97, no. 8, pp. 2368-2371, 2014.

[120] C.-M. Wang, S.-Y. Lin, K.-S. Kao, Y.-C. Chen, and S.-C. Weng, “Microstructural and electrical properties of $CaTiO_3$– $CaCu_3Ti_4O_{12}$ ceramics,” Journal of Alloys and Compounds, vol. 491, no. 1, pp. 423-430, 2010.

[121] W.-X. Yuan, and S. K. Hark, “Investigation on the origin of the giant dielectric constant in $CaCu_3Ti_4O_{12}$ ceramics through analyzing $CaCu_3Ti_4O_{12}$–HfO_2 composites,” Journal of the European Ceramic Society, vol. 32, no. 2, pp. 465-470, 2012.

[122] E. A. Patterson, S. Kwon, C.-C. Huang, and D. P. Cann, “Effects of ZrO2 additions on the dielectric properties of $CaCu_3Ti_4O_{12}$,” vol. 87, no. 18, pp. 182911, 2005.

[123] M. A. Ponce, M. A. Ramirez, F. Schipani, E. Joanni, J. P. Tomba, and M. S. Castro, “Electrical behavior analysis of n-type $CaCu_3Ti_4O_{12}$ thick films exposed to different atmospheres,” Journal of the European Ceramic Society, vol. 35, no. 1, pp. 153-161, 2015.

[124] J. Yang, M. Shen, and L. Fang, “The electrode/sample contact effects on the dielectric properties of the $CaCu_3Ti_4O_{12}$ ceramic,” Materials Letters, vol. 59, no. 29, pp. 3990-3993, 2005.

[125] Y. Shimizu, H. Arai, and T. Seiyama, “Theoretical studies on the impedance-humidity characteristics of ceramic humidity sensors,” Sensors and Actuators, vol. 7, no. 1, pp. 11-22, 1985.

[126] E. W. Thornton, and P. G. Harrison, “Tin Oxide Surfaces. Part 1.-Surface Hydroxyl Groups and the Chemisorption of Carbon Dioxide and Carbon Monoxide on Tin(IV) Oxide,” Journal of the Chemical Society, Faraday Transactions 1: Physical Chemistry in Condensed Phases, vol. 71, no. 0, pp. 461-472, 1975.

[127] M. Egashira, M. Nakashima, S. Kawasumi, and T. Selyama, “Temperature programmed desorption study of water adsorbed on metal oxides. 2. Tin oxide surfaces,” The Journal of Physical Chemistry, vol. 85, no. 26, pp. 4125-4130, 1981.

[128] J. Mollá, M. González, R. Vila, and A. Ibarra, “Effect of humidity on microwave dielectric losses of porous alumina,” Journal of Applied Physics, vol. 85, no. 3, pp. 1727-1730, 1999.

[129] C. Mrabet, N. Mahdhi, A. Boukhachem, M. Amlouk, and T. Manoubi, “Effects of surface oxygen vacancies content on wettability of zinc oxide nanorods doped with lanthanum,” Journal of Alloys and Compounds, vol. 688, pp. 122-132, 2016.

[130] W. Göpel, and K. D. Schierbaum, “SnO_2 sensors: Current status and future prospects,” Sensors and Actuators B: Chemical, vol. 26, no. 1, pp. 1-12, 1995.

[131] D. Ming, J. Reau, J. Ravez, J. Gitae, and P. Hagenmuller, “Impedance-spectroscopy analysis of a $LiTaO_3$-type single crystal,” J Journal of Solid-State Chemistry, vol. 116, no. 1, pp. 185-192, 1995.

[132] S. Manoharan, S. Birlasekaran, and C. Suryanarayana, “Computer program for nonlinear least square analysis of impedance and admittance data,” Bulletin of Electrochemistry, vol. 2, no. 5, pp. 509-513, 1986.

[133] J. Liu, C.-g. Duan, W. N. Mei, R. W. Smith, and J. R. Hardy, “Dielectric properties and Maxwell-Wagner relaxation of compounds $ACu_3Ti_4O_{12}$ (A=Ca,$Bi_{2/3}$,$Y_{2/3}$,$La_{2/3}$),” Journal of Applied Physics, vol. 98, no. 9, pp. 093703, 2005.

[134] N. Kolev, R. P. Bontchev, A. J. Jacobson, V. Popov, V. G. Hadjiev, A. Litvinchuk, and M. Iliev, “Raman spectroscopy of $CaCu_3Ti_4O_{12}$,” Physical Review B, vol. 66, pp. 132102, 2002.

[135] A. Felix, E. Longo, J. Varela, and M. Orlandi, “Gas sensing and conductivity relationship on nanoporous thin films: A $CaCu_3Ti_4O_{12}$ case study,” Thin Solid Films, vol. 604, pp. 69-73, 2016.

[136] A. Mohsen, A. Mohd Fadzil, and A. Zainal Arifin, “A short review on copper calcium titanate (CCTO) Electroceramic: synthesis, dielectric properties, film deposition, and sensing application,” Nano-Micro Letters, 2016.

[137] Y. C. Yeh, and T. Y. Tseng, “Humidity sensitive electrical properties of $Ba_{0.5}Sr_{0.5}TiO_3$ porous ceramics,” Journal of Materials Science Letters, vol. 7, no. 7, pp. 766-768, 1988.

[138] H. B. Xiao, C. P. Yang, C. Huang, L. F. Xu, D. W. Shi, V. V. Marchenkov, I. V. Medvedeva, and K. Bärner, “Influence of oxygen vacancy on the electronic structure of CaCu3Ti4O12 and its deep-level vacancy trap states by first-principle calculation,” vol. 111, no. 6, pp. 063713, 2012.

[139] K. Wu, Y. Huang, J. Li, and S. Li, “Space charge polarization modulated instability of low frequency permittivity in $CaCu_3Ti_4O_{12}$ ceramics,” vol. 111, no. 4, pp. 042902, 2017.

[140] W. Yuan, “Investigation on the decomposable process and the secondary liquid phase effect on the dielectric properties of $CaCu_3Ti_4O_{12}$ ceramics,” J Journal of Physics D: Applied Physics, vol. 42, no. 17, pp. 175401, 2009.

[141] T. Prasit, T. Suwat, Y. Teerapon, and M. Santi, “Dielectric relaxation and dielectric response mechanism in (Li, Ti)-doped NiO ceramics,” Journal of Physics: Condensed Matter, vol. 20, no. 39, pp. 395227, 2008.

[142] F. Kremer, and A. Schönhals, Broadband Dielectric Spectroscopy: Springer Berlin Heidelberg, 2012.

[143] W. Li, and R. W. Schwartz, “ac conductivity relaxation processes in $CaCu_3Ti_4O_{12}$ ceramics: Grain boundary and domain boundary effects,” Applied Physics Letters vol. 89, no. 24, pp. 242906, 2006.

[144] D. P. Samarakoon, N. Govindaraju, and R. N. Singh, "Calcium Copper Titanate Based High Dielectric Constant Materials for Energy Storage Applications.," Processing, Properties, and Design of Advanced Ceramics and Composites, Ceramic Transactions Series 259, G. Singh, A. Bhalla, M. M. Mahmoud, R. H. Castro, N. P. Bansal, D. Zhu, J. P. Singh and Y. Wu, eds., pp. 131-140, 2016.

[145] D. P. Samarakoon, N. Govindaraju, and R. N. Singh, "Influence of Processing and Microstructure on Dielectric Properties of Calcium Copper Titanate Ceramics," Processing, Properties, and Design of Advanced Ceramics and Composites II, Ceramic Transactions Series 261, N. P. Bansal, R. H. R. Castro, M. Jenkins, A. Bandyopadhyay, S. Bose, A. Bhalla, J. P. Singh, M. M. Mahmoud, G. Pickrell and S. Johnson, eds., pp. 237-243, 2018.

[146] L. He, J. Neaton, M. H. Cohen, D. Vanderbilt, and C. Homes, “First-principles study of the structure and lattice dielectric response of $CaCu_3Ti_4O_{12}$,” J Physical Review B, vol. 65, no. 21, pp. 214112, 2002.

[147] J. Li, A. W. Sleight, and M. A. Subramanian, “Evidence for internal resistive barriers in a crystal of the giant dielectric constant material: $CaCu_3Ti_4O_{12}$,” Solid State Communications, vol. 135, no. 4, pp. 260-262, 2005.

[148] D. P. Samarakoon, N. Govindaraju, and R. N. Singh, “Dielectric Properties of Calcium Copper Titanate Ceramics Exposed to Air and Dry Nitrogen Atmospheres,” Transactions of the Indian Institute of Metals, vol. 72, pp. 1-7, 2019.

[149] D. P. Samarakoon, N. Govindaraju, and R. N. Singh, “Influence of atmospheres on the dielectric properties of calcium copper titanate ceramics,” Journal of the American Ceramic Society, pp. 1-13, 2019.

[150] S. Ke, H. Huang, and H. Fan, “Relaxor behavior in $CaCu_3Ti_4O_{12}$ ceramics,” Applied Physics Letters, vol. 89, no. 18, pp. 182904, 2006.

[151] C.-C. Wang, M.-N. Zhang, K.-B. Xu, and G.-J. Wang, “Origin of high-temperature relaxor-like behavior in $CaCu_3Ti_4O_{12}$,” Journal of Applied Physics, vol. 112, no. 3, pp. 034109, 2012.

[152] T. Prasit, T. Suwat, Y. Teerapon, and M. Santi, “Dielectric relaxation and dielectric response mechanism in (Li,Ti)-doped NiO ceramics,” Journal of Physics: Condensed Matter, vol. 20, no. 39, pp. 395227, 2008.

[153] Y. W. Li, Y. D. Shen, Z. G. Hu, F. Y. Yue, and J. H. Chu, “Effect of thickness on the dielectric property and nonlinear current–voltage behavior of $CaCu_3Ti_4O_{12}$ thin films,” Physics Letters A, vol. 373, no. 27, pp. 2389-2392, 2009.

[154] V. Brizé, G. Gruener, J. Wolfman, K. Fatyeyeva, M. Tabellout, M. Gervais, and F. Gervais, “Grain size effects on the dielectric constant of $CaCu_3Ti_4O_{12}$ ceramics,” Materials Science and Engineering: B, vol. 129, no. 1, pp. 135-138, 2006.

[155] J. Jumpatam, N. Chanlek, and P. Thongbai, “Giant dielectric response, electrical properties and nonlinear current-voltage characteristic of Al2O3-CaCu3Ti4O12 nanocomposites,” Applied Surface Science, vol. 476, pp. 623-631, 2019.

[156] M. Li, “Study of the humidity-sensing mechanism of $CaCu_3Ti_4O_{12}$,” Sensors and Actuators B: Chemical, vol. 228, pp. 443-447, 2016.

[157] M. Li, X. L. Chen, D. F. Zhang, W. Y. Wang, and W. J. Wang, “Humidity sensitive properties of pure and Mg-doped $CaCu_3Ti_4O_{12}$,” Sensors and Actuators B: Chemical, vol. 147, no. 2, pp. 447-452, 2010.

[158] D. P. Samarakoon, and R. N. Singh, “Thickness dependent dielectric properties of calcium copper titanate ceramics measured in a controlled atmosphere,” Ceramics International, vol. 45, pp. 16554-16563, 2019.

[159] Y. Shimizu, M. Shimabukuro, H. Arai, and T. Seiyama, “Enhancement of humidity-sensitivity for perovskite-type oxides having semi conductivity,” Chemistry Letters, vol. 7, no. 7, pp. 917-920, 1985.

[160] J. Holc, J. Slunčko, and M. Hrovat, “Temperature characteristics of electrical properties of (Ba,Sr)TiO_3 thick film humidity sensors,” Sensors and Actuators B, vol. 26, no. 1-3, pp. 99-102, 1995.

[161] D. A. Chang, and T. Y. Tseng, “Humidity-sensitivity characteristics of $CaTiO_3$ porous ceramics,” Journal of Materials Science Letters, vol. 9, no. 8, pp. 943-944, 1990.

[162] C. Slouka, T. Kainz, E. Navickas, G. Walch, H. Hutter, K. Reichmann, and J. Fleig, “The effect of acceptor and donor doping on oxygen vacancy concentrations in lead zirconate titanate (PZT),” Materials, vol. 9, no. 11, pp. 945, 2016.

[163] T. Y. Li, R. J. Si, J. Sun, S. T. Wang, J. Wang, R. Ahmed, G. B. Zhu, and C. C. Wang, “Giant and controllable humidity sensitivity achieved in (Na+Nb) co-doped rutile TiO_2,” Sensors and Actuators B: Chemical, vol. 293, pp. 151-158, 2019.

VITA

Disna Priyadarshani Samarakoon

Candidate for the Degree of

Doctor of Philosophy

Dissertation: EFFECTS OF PROCESSING CONDITIONS AND TESTING ATMOSPHERE ON THE ELECTRICAL PROPERTIES OF CALCIUM COPPER TITANATE CERAMICS FOR ENERGY STORAGE APPLICATIONS.

Major Field: Materials Science and Engineering

Biographical:

Education:

Completed the requirements for the Doctor of Philosophy in Materials Science and Engineering at Oklahoma State University, Stillwater, Oklahoma in July, 2019.

Completed the requirements for the Master of Science in Mechanical Engineering at Kansas State University, Manhattan, Kansas in 2010.

Completed the requirements for the Bachelor of Science in Materials Science and Engineering at University of Moratuwa, Moratuwa, Sri Lanka in 2004.